UNCLASSIFIED

AD NUMBER

AD816546

NEW LIMITATION CHANGE

TO

Approved for public release, distribution unlimited

FROM

Distribution authorized to U.S. Gov't. agencies and their contractors; Critical Technology; JUN 1967. Other requests shall be referred to Air Force Rocket Propulsion Lab., Edwards AFB, CA.

AUTHORITY

AFRPL ltr, 27 Oct 1971

THIS PAGE IS UNCLASSIFIED

AD816546

DESIGNER'S GUIDE AND COMPUTER PROGRAM

FOR ABLATIVE MATERIALS IN LIQUID ROCKET

THRUST CHAMBERS

Final Report

H. S. Friedman
W. S. Hines
G. D. Cunial

Rocketdyne
A Division of North American Aviation, Inc.
Canoga Park, California

TECHNICAL REPORT AFRPL-TR-67-159

June 1967

NOTICES

When U. S. Government drawings, specifications, or
other data are used for any purpose other than a
definitely related Government procurement operation,
the Government thereby incurs no responsibility nor
any obligation whatsoever, and the fact that the
Government may have formulated, furnished, or in any
way supplied the said drawings, specifications, or
other data, is not to be regarded by implication or
otherwise, or in any manner licensing the holder or
any other person or corporation, or conveying any
rights or permission to manufacture, use, or sell
any patented invention that may in any way be related
thereto.

DESIGNER'S GUIDE AND COMPUTER PROGRAM

FOR ABLATIVE MATERIALS IN LIQUID ROCKET

THRUST CHAMBERS

Final Report

H. A. Friedman
W. S. Hines
G. D. Cunial

Rocketdyne
A Division of North American Aviation, Inc.
Canoga Park, California

June 1967

FOREWORD

This technical report was prepared for the Air
Force Rocket Propulsion Laboratory, Edwards Air
Force Base, California, by Rocketdyne, a Division
of North American Aviation, Inc. The report cov-
ers work done under contract AF04(611)-11415
during the period of 1 April 1966 through 30 April
1967. The Air Force Project Monitors during the
course of the program were Mr. J. Denker, Capt.
R. Bryson and Lt. J. Hintz. The Rocketdyne Program
Managers during the course of the program were
Dr. R. B. Lawhead and Mr. T. A. Coultas with Dr. E.
Talmor as responsible supervisor. The principal
investigators on the various tasks were as follows:

    Task 1 - Mr. H. A. Friedman
    Task 2 - Messrs. W. S. Hines and G. D. Cunial
    Task 3 - Mr. W. S. Hines

General assistance in all tasks was provided by
Mr. B. L. McFarland.

This report has been given the Rocketdyne identifi-
cation number R-7022. It contains no classified
information extracted from other classified documents.

A Computer Program Deck and a Computer Operator's
Manual have been submitted separately.

This technical report has been reviewed and is
approved.

<div align="right">

JAMES A. HINTZ,
1st Lt., USAF
AFRPL Project Engineer

</div>

ABSTRACT

The two-dimensional ablative heat transfer computer
program generated under contract AF04(611)-9714 was
refined and extended to handle anisotropic materials,
more than one charring material and reradiation at
the heated surface. Results of the two-dimensional
program were compared to experimental data to deter-
mine effective values of material properties used in
the analysis to simulate gas generation and cracking
reactions. The resulting effective properties for
two ablative materials were used in a parametric
study generating basic information for the design
of ablative systems in liquid rocket thrust chambers.
Graphs and charts showing the variation of thermal
penetration, char depth and surface erosion are
included.

CONTENTS

ILLUSTRATIONS

TABLE

INTRODUCTION

Effective design of rocket engine thrust chambers, which are passively
cooled by heat sink or ablative techniques, requires predictions of the
effect of high-temperature combustion products on candidate thrust chamber
wall materials. Under Contract AF04(611)-9714, Rocketdyne conducted a
12-month program entitled "Effect of Rocket Engine Combustion on Chamber
Materials," in which computer programs were developed for the numerical
solution of one- and two-dimensional models of transient ablation and heat
conduction. Detailed reports of this program can be found in Ref. 1 and
2 , including discussions of the physical and mathematical models employed,
the numerical procedures developed for the solution, and a comparison of
computed results to test data. Operating instructions for the computer
codes are given in Ref. 3 and 4.

In April 1966, a 12-month sequel program was initiated at Rocketdyne under
Contract AF04(611)-11415, entitled "Designer's Guide and Computer Program
for Ablative Materials in Liquid Rocket Thrust Chambers." The objectives
of the program were to extend the scope of the two-dimensional program
(2D-ABLATE) and conduct a comprehensive parametric study. The results of
this study were to be presented in a form convenient for design of ablative
rocket engine thrust chambers. The work was performed in four phases or
tasks:

1. The two-dimensional program was extended to handle anisotropic
    materials, multiple charring ablators, and the effects of
    reradiation at the heated surface.

2. Computed results were compared to existing experimental data to
    determine values of effective thermal material properties used
    in the 2D-ABLATE program to simulate the chemical reactions which
    occur in the interior of the charring materials.

3. A parametric study was performed to determine thermal and ablative
    effects as functions of parameters describing thrust chamber opera-
    ting conditions, geometry, and materials in liquid rocket engines.

1

4. Charts and curves were generated on the basis of the results of 3 above for use in the design of thrust chambers. In a separate report, an operators manual was written for the final version of the 2D-ABLATE program, including the capabilities added in 1 above.

In the subsequent sections of this report, a review of the original 2D-ABLATE program is first given. This is followed by separate presentations and discussions of the various phases of work accomplished.

REVIEW OF 2D-ABLATE PROGRAM

GENERAL

Although it is assumed that the reader is familiar with the material presented in Ref. 2, a brief review of the 2D-ABLATE computer program is given here for convenience.

The 2D-ABLATE program was developed to help fill the void caused by the scarcity of comprehensive computer codes for analyzing two-dimensional transient ablation and heat conduction problems in rocket engine thrust chamber walls. The analysis was performed using cylindrical coordinates, axial and radial, for the wall materials (as many as five) of an axisymmetric thrust chamber of general configuration (Fig. 1). Predicted by the program are temperature and pyrolysis gas mass flux distributions induced throughout the wall materials and recession rates at the surface exposed to the hot combustion gases. Following are some of the more important program features:

1. The thrust chamber geometry is simulated using as many as 40 quadratic segments. Thus, materials with arbitrarily curved boundaries can be handled.

2. Curvature-preserving techniques are used to obtain a second order accurate approximation of the normally directed heat fluxes encountered at the curved material boundaries.

3. In-depth charring within the wall materials and erosion of the exposed inside wall surface are treated in the program, and transpiration effects caused by gases generated within the wall materials and at the exposed surfaces are accounted for.

4. Physical and chemical properties may be specified as functions of temperature for each thrust chamber material.

5. The numerical procedures employed are stable* under most circumstances encountered in thrust chamber applications, thus

---

*Stable in the sense that errors introduced into the analysis do not grow during the course of the calculation

3
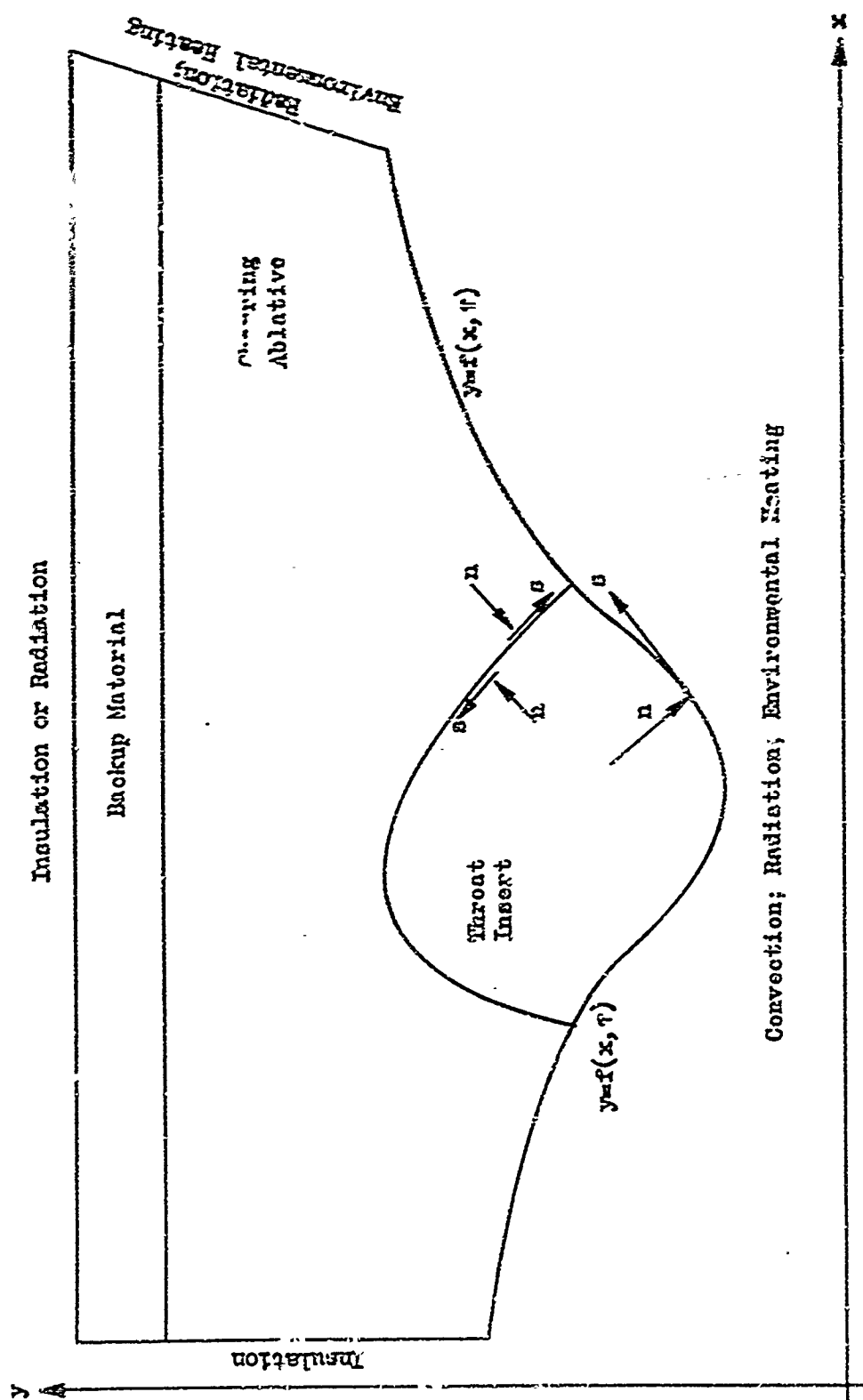
Figure 1. Typical Thrust Chamber Configuration and Boundary Conditions

permitting the use of relatively large time steps. In particular, a generalization of the unconditionally stable Peaceman-Rachford alternating direction method (Ref. 5) was employed to discretize the energy equation rather than the more frequently used, conditionally stable, explicit forward difference method which often requires the use of prohibitively small time increments to avoid error growth.

6. Complex duty cycles of intermittent engine firing can be simulated, including either steady bursts of firing followed by soakout or high-frequency pulsing.

MATHEMATICAL MODEL

In formulating the mathematical model and developing the numerical solution, the following assumptions were made concerning charring materials treated in the analysis:

1. In any thrust chamber configuration, there is no more than one charring material (this limitation was removed during the subsequent effort presently being reported). It is a continuous material with continuously changing material properties.

2. Chemical reactions in the charring region are treated in depth; i.e., they are permitted to take place throughout a continuous range of temperature rather than being confined to a single "interface" of constant temperature.(By specifying a very narrow temperature range for the reaction, an interface model can be simulated when required, e.g., in the case of vaporization of a metal filling a solid porous matrix.) These reactions, however, are simulated thermodynamically (rather than kinetically) in the energy and continuity equations. They include a maximum of three gas generation reactions (pyrolysis, a char-reinforcement reaction, and a further decomposition of the solid product of this reaction) plus cracking of the generated gases.

5

3. The porous char is cooled convectively by the gases generated in the charring material and the gas and char temperatures at any point are identical. Conduction of heat within the gas is assumed to be negligible in comparison with that in the char.

4. Gas density is assumed to be negligible in comparison to the char density.

5. The generated gas mass flux in the porous char region is assumed to be oriented in the direction of the temperature gradient vector.

In addition, the following ground rules were followed in analyzing the effects of surface erosion and recession:

1. Any of the thrust chamber wall materials exposed to the hot combustion gases are subject to surface erosion. For each exposed material, the surface removal modes include melting, vaporization, and as many as three independent chemical reactions with components of the combustion gas.

2. For vaporization and chemical reactions, the removal rate is computed based on mass diffusion in the boundary layer coupled with chemical kinetics at the wall surface.

The energy and continuity equations used in the model for the charring material have the following forms (see Ref. 2, Appendix A, for justification):

$$\left(\rho C - \sum_r Q_r \frac{\partial \rho}{\partial F_r} \frac{dF_r}{dT}\right)\frac{\partial T}{\partial \tau} = \frac{\partial}{\partial x}\left(K\frac{\partial T}{\partial x}\right) + \frac{1}{y}\frac{\partial}{\partial y}\left(yK\frac{\partial T}{\partial y}\right) - \frac{dH}{dT}\left(G_x\frac{\partial T}{\partial x} + G_y\frac{\partial T}{\partial y}\right) \quad (1)$$

$$-\frac{\partial \rho}{\partial \tau} = -\sum_r \frac{\partial \rho}{\partial F_r}\frac{\partial F_r}{\partial \tau} = \frac{\partial G_x}{\partial x} + \frac{1}{y}\frac{\partial}{\partial y}\left(yG_y\right) \quad (2)$$

where r ranges over the gas generation reactions occurring within the material. The orientation equation for the generated gas mass flux in the charring material takes the following form:

6

$$G_x/G_y = \frac{\partial T}{\partial x} \Big/ \frac{\partial T}{\partial y} = R_G(x,y,\tau) \tag{3}$$

Equation 3 is a formulation of assumption 5 above for charring materials, which in conjunction with assumption 4, permits the solution of Eq. 1 and 2 without the need for a separate momentum equation. The dependent variables of Eq. 1 through 3 are T, G_y, and G_x (or R_G). All physical and chemical properties appearing are assumed to be known functions of temperature. For the noncharring wall materials present in a thrust chamber configuration, Eq. 2 and 3 are not applicable, and Eq. 1 reduces to the pure conduction equation, as follows:

$$\rho C \frac{\partial T}{\partial \tau} = \frac{\partial}{\partial x}\left(K \frac{\partial T}{\partial x}\right) + \frac{1}{y}\frac{\partial}{\partial y}\left(y K \frac{\partial T}{\partial y}\right) \tag{4}$$

In the event of surface erosion caused by engine firing, an additional parameter must be predicted, $f(x,\tau)$, the changing radial position of the receding hot-gas boundary (Fig. 1). The following equation is used to relate the radial recession rate to the predicted normal recession rates:

$$\frac{\partial f}{\partial \tau} = \left(\sum_r v_r\right)\left[1 + \left(\frac{\partial f}{\partial x}\right)^2\right]^{1/2} , \tag{5}$$

where r ranges over those species generated at the surface and does not include those generated within the material. The v_r's are in turn defined by an appropriate rate equation (Ref. 2, Appendix C) for each surface removal mode r. In practice, the v_r's are calculated iteratively so as to satisfy both the rate equation and the energy balance at the exposed inside wall surface, which is taken in the form:

$$K \frac{\partial T}{\partial n} = h_{eff}(T_{aw} - T) - \rho \sum_r v_r (\Delta H)_r \tag{6}$$

7

More generally, Eq. 6 can be used as a convenient formulation of all the exterior boundary conditions which describe the heating and cooling mechanisms encountered (Fig. 1), where h_{eff} may include such effects as those of convection, radiation, and/or aerodynamic heating. Thus we write

$$h_{eff} = h_{conv} + h_{rad} + h_{env} \tag{7}$$

At an insulated boundary, both h_{eff} and the v_r are set to zero in Eq. 6. The v_r's, indeed, apply only at the exposed hot-gas boundary and are zero elsewhere. Similarly, T_{aw}, in Eq. 6, has physical significance only at an exposed boundary, but is used elsewhere as a convenient reference temperature in the definition of the effective quantity h_{eff}. In particular, when radiative and environmental heat flux terms are required, they are expressed as follows:

$$h_{rad} = - \frac{\sigma \epsilon \beta_f \left(T^4 - T_{env}^4 \right)}{T_{aw} - T}; \quad h_{env} = \frac{q_{env}}{T_{aw} - T} \tag{8}$$

Thus, the effect of T_{aw} is cancelled when h_{rad} and h_{env} are substituted in Eq. 6 (this form is employed as a linearization device in the finite difference solution procedure). The cancellation does not occur in the convection term at the exposed boundary, where h_{conv} includes modification of the basic convective heat transfer coefficient, $\bar{h}_{conv}$, by the blocking effect of the gases ejected at the surface:

$$h_{conv} = \bar{h}_{conv} + B \, C_{p_\infty} \sum_j \left(\frac{dH_j}{dT} / C_{p_\infty} \right)^{n_j} G_j \tag{9}$$

The summation of Eq. 9 is taken over all gaseous species ejected at the surface, where G_j is defined to be $-\rho v_j$ for the gases generated at the surface, and for the internally generated gases we use

$$G_j = - \left(G_x^2 + G_y^2 \right)^{1/2} \tag{10}$$

8

At an interface separating two adjacent material regions, say regions I and J, the continuity of temperature and outward normal heat flux are expressed as follows:

$$T_I = T_J; \quad K_I \left. \frac{\partial T}{\partial n} \right|_I = -K_J \left. \frac{\partial T}{\partial n} \right|_J, \tag{11}$$

Initially, the temperatures are assumed to be constant for all materials; e.g., ambient temperature.

NUMERICAL SOLUTION

A time step procedure was employed to uncouple and solve the continuous equations given above where finite difference techniques were used to discretize the continuous parameters. Predicted in each step are the two-dimensional (actually three, because of the assumption of axial symmetry) temperature distribution throughout the thrust chamber materials, the generated gas mass flux distribution in the charring material, and the new position of the inside surface exposed to the hot combustion gases (in the event of surface erosion and recession). No specific char front or depth is calculated because, as discussed in assumption 2 above, pyrolysis is permitted to occur over a temperature range rather than at a single value. The pyrolysis zone, however, can be identified at any time level by inspection of the predicted temperatures or, in the event of a stop-start engine firing cycle, by noting the maximum temperatures achieved.

Spatially, the discretization is achieved by imposing a mesh on the multi-material region of interest (Fig. 2). Mesh points are located at the intersections of the mesh lines with each other and with the boundaries and material interfaces and are classified as regular, irregular, boundary, and interface points (Fig. 2). The continuous temperature and generated gas mass flux distributions are approximated by discrete distributions defined only at mesh points and discrete time levels. These are obtained by solving the difference equations resulting from replacing the continuous derivatives in the equations above with their finite difference equivalents (Ref. 2).

9
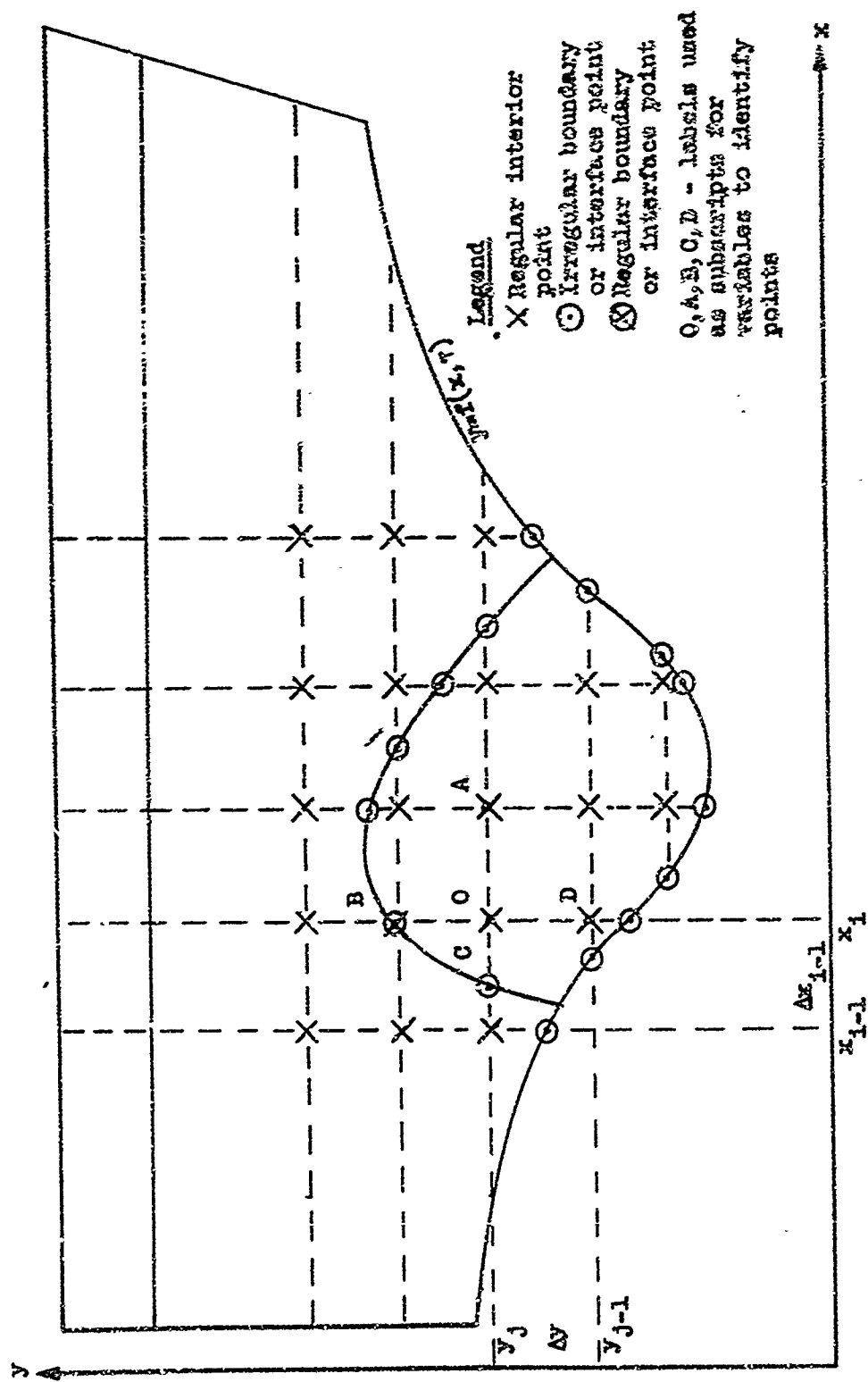
Figure 2. Typical Mesh Configuration and Categorization of Resulting Mesh Points

Of particular interest is an essentially second order accurate (in time as well as distance) generalization of the unconditionally stable, implicit alternating direction method of Peaceman and Rachford, employed in each time step to discretize and solve Eq. 1 (or Eq. 4) for temperature in conjunction with second order accurate, curvature-preserving techniques developed to express the normal gradient conditions at curved boundaries. A backward time difference was used to approximate the continuity equation (Eq. 2) in obtaining the internally generated gas mass flux distribution along with second order accurate central differences in the axial and radial directions. Although a forward time difference was used to discretize the recession equation (Eq. 5), the approximation nevertheless approaches a second-order central difference procedure because of the iteration, mentioned above, which is required to obtain values of the v_r. Details of the numerical procedures employed are given in Ref. 2.

Because of the use of essentially central (not exactly because the initially nonlinear difference equations are linearized in each time step by taking coefficients at the old time level) or backward time differences in discretizing the differential equations in the interior of the material regions, the resulting solution procedure approaches unconditional stability for sufficiently small, externally generated heat fluxes. However, when high values of heat flux are encountered at the hot-gas boundary during periods of steady firing, limitations may be required on the size of the time step, especially at the beginning of such a period. In general, such limitations are not nearly as severe as those required for explicit forward difference methods, and are not necessary at all during periods of sparse intermittent firing or during soakback. The favorable stability situation plus the generally second order spatial and temporal differencing permit the use of relatively large time and distance increments (compared to those frequently required for explicit forward difference procedures) and a substantial saving in computer time.

In simulating the normal temperature gradient conditions at curved surfaces as given by Eq. 6 and 11, the following exact relationships are utilized,

11

which relate the normal and tangential derivatives to those in the axial and radial directions:

$$\frac{\partial T}{\partial n} = \pm \left(\frac{\partial f}{\partial x} \frac{\partial T}{\partial x} - \frac{\partial T}{\partial y} \right) \Big/ \left[1 + \left(\frac{\partial f}{\partial x} \right)^2 \right]^{1/2} ;$$

$$\frac{\partial T}{\partial s} = \pm \left(\frac{\partial T}{\partial x} + \frac{\partial f}{\partial x} \frac{\partial T}{\partial y} \right) \Big/ \left[1 + \left(\frac{\partial f}{\partial x} \right)^2 \right]^{1/2} \tag{12}$$

In Eq 12, $y = f(x, \tau)$ is the equation of the boundary segment under consideration and the plus (minus) sign is used at a lower (upper) boundary; i.e., where the outward normal has a negative (positive) component in the y direction. The direction of n and s is indicated in Fig. 1 for a material at a boundary and an interface. The expressions for $\partial T/\partial n$ and $\partial T/\partial s$ can be combined (in keeping with the alternating direction method) so as to eliminate $\partial T/\partial y$ (or $\partial T/\partial x$) in an odd (even) time step. Finally, on purely physical grounds, we assume that $\partial T/\partial s$ is so dominated by $\partial T/\partial n$ that in the resulting expressions, we may neglect terms in $\partial T/\partial s$. Thus we obtain, for odd and even steps, respectively:

$$\frac{\partial T}{\partial x} = \pm \frac{\partial f}{\partial x} \frac{\partial T}{\partial n} \Big/ \left[1 + \left(\frac{\partial f}{\partial x} \right)^2 \right]^{1/2}$$

$$\frac{\partial T}{\partial y} = \pm \frac{\partial T}{\partial n} \Big/ \left[1 + \left(\frac{\partial f}{\partial x} \right)^2 \right]^{1/2} \tag{13}$$

Eq. 13 is used to replace $\partial T/\partial n$ in Eq. 6 and 11 and the resulting expressions are discretized with second order spatial accuracy.

All systems of difference equations generated in each time step are at worst tridiagonal* and are easily solved directly (rather than iteratively) by simple recursion formulas.

---

*A system of equations is tridiagonal if all the nonzero elements of its coefficient matrix lie on the main diagonal and its immediately adjacent diagonals.

RESULTS

Evaluation of the 2D-ABLATE program included comparisons of program results
with both theoretical and test data, including in-depth checkout of the
following cases:

1. Simulation of transient one-dimensional radial conduction in a
   hollow cylinder heated on the inside and insulated on the outside,
   with no charring or recession. The exact series solution for this
   problem is well-known and has been presented in the form of tem-
   perature response curves in Ref. 6.

2. Comparison to test data supplied by Edwards AFB from an engine
   firing with shutdown and soakback in a two-material thrust cham-
   ber, including a charring carbon-cloth/phenolic backed by a stainless-
   steel shell (Fig. 3). Here the full two-dimensional transient
   case was treated.

3. Comparison to measured temperatures obtained from a complicated
   mission duty cycle of engine firing (including pulsing) and aero-
   dynamic heating for a four-material charring, attitude control engine.
   Predicted computer results were in good agreement with measured
   backwall throat- and exit temperature histories. (This comparison
   was not reported in Ref. 2; details may be found in Ref. 7.)

Cases 1 and 2 above are fully reported in Ref. 2 and need not be repeated
here. Some of the results of Case 2, however, were used as controls for
checking out the 2D-ABLATE program extensions discussed later in this
report.

PROGRAM STRUCTURE

The 2D-ABLATE program was coded in Fortran IV for use on the IBM 7094.
Several links were employed to take advantage of the system overlay feature.
In addition to the main control link, Link 0, two other links were provided

13
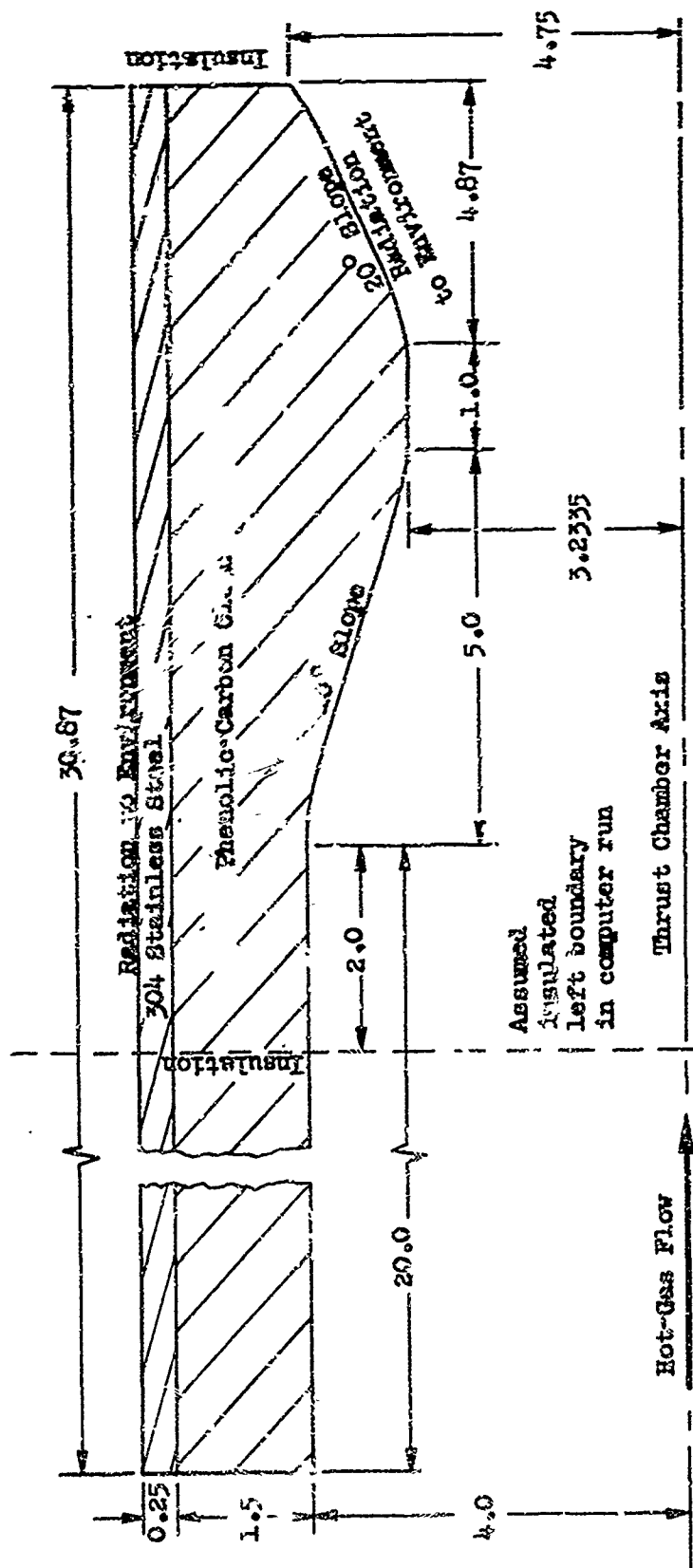
FIG. 3. THRUST CHAMBER WALL CONFIGURATION USED FOR EAFB FIRING

14

for:

1. Link 1, in which all set-up is performed for the time-step calculation (Ref. 2)

2. Link 2, the time-step calculation

Because the extensions to the 2D-ABLATE program (under the current contract) expanded Link 2 beyond the 7094 core storage capacity, Link 2 has been further sublinked, utilizing the overlay feature. This is described in more detail in another section of this report.

TASK 1, EXTENSION OF THE TWO-DIMENSIONAL ABLATION PROGRAM

In Task 1 of the present contract, the 2D-ABLATE computer program (as developed under Contract AF04(611)-9714) was extended by the addition of several mechanisms each of which, when applicable, can have a significant effect on the performance of ablative materials. Included were the following modifications:

A. The effect of radiative exchange across the thrust chamber between opposing surfaces exposed to the hot combustion gases. During firing, this effect can exert a strong influence on the surface temperature histories attained.

B. Analysis of materials with differing temperature-dependent conductivities in major and minor directions to provide adequate treatment for strongly anisotropic materials of current interest.

C. Provision to permit any of the wall materials to be charring ablators rather than being restricted to just one such material. Although most research engines are fabricated with only a single charring material, more than one is often required in the case of production engines. Frequently encountered classes of multiple-ablative construction include stacked materials (e.g., the Rocketdyne LEM engine with a phenolic-refrasil laminate backed by a low density phenolic-asbestos) and side by side (e.g., the Apollo attitude control engines with a 45-degree phenolic-refrasil laminate in the chamber and the same material in the nozzle extension at a 0-degree orientation).

In addition to the three Task 1 modifications (henceforth referred to as Tasks 1.A, 1.B, and 1.C), several other additions, modifications, and corrections were made to the 2D-ABLATE program as required during the performance of Tasks 1, 2, and 3 of the current study. Because these changes do not fall within the scope of Task 1, they are referred to collectively as "general modifications" and briefly described prior to the Task 1 discussion.

17

Checkout of most of these modifications was performed by comparison with results obtained previously with the "old version" of 2D-ABLATE. The test case used for the comparisons was Case 2 discussed in the Review section above and described in detail in Ref. 2. For Task 1, a preliminary checkout step involved demonstration of the ability of the extended program to suppress all the new mechanisms and perform as originally written.

GENERAL MODIFICATIONS

Program Structure

As indicated in the Review section above, coding of the old version of the 2D-ABLATE program was performed for IBM 7094 application. The "new version" (including the Task 1 extensions) was to be used on either the 7094 or the IBM 360. To accommodate the Task 1 program extensions, several methods were investigated of increasing available core storage in the new 7094 version. (In the new 360 version, no such problem existed. Indeed, it was possible to unlink the program completely without exceeding core storage limitations.) It was decided to further subdivide the time step link (Link 2 in the old version), yielding Link 2, the control link, Link 3, the recession calculation, and Link 4, the remainder of the calculation in each time step. Thus, Link 3 is bypassed in any time step for which the recession subroutines are not required (see Fig. 4 for a chart of the relinked program structure). The saving amounted to over 3500 locations in core during Link 4 (and even more during Link 3), which was more than enough for accommodation of the Task 1 extensions.

Added Capability

Because performance of the Task 2 and 3 efforts required extensive evaluation of calculated temperature histories, a great deal of time-consuming manual cross-plotting was avoided by extending the program to provide a

18
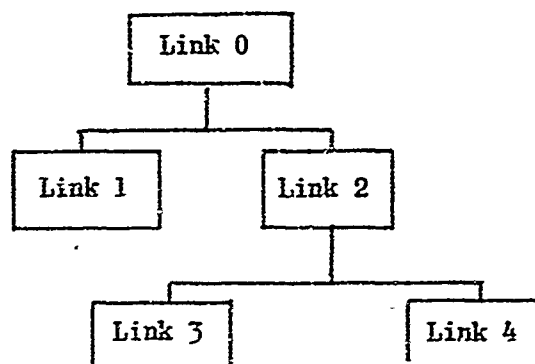
(a). Linkage of the new version
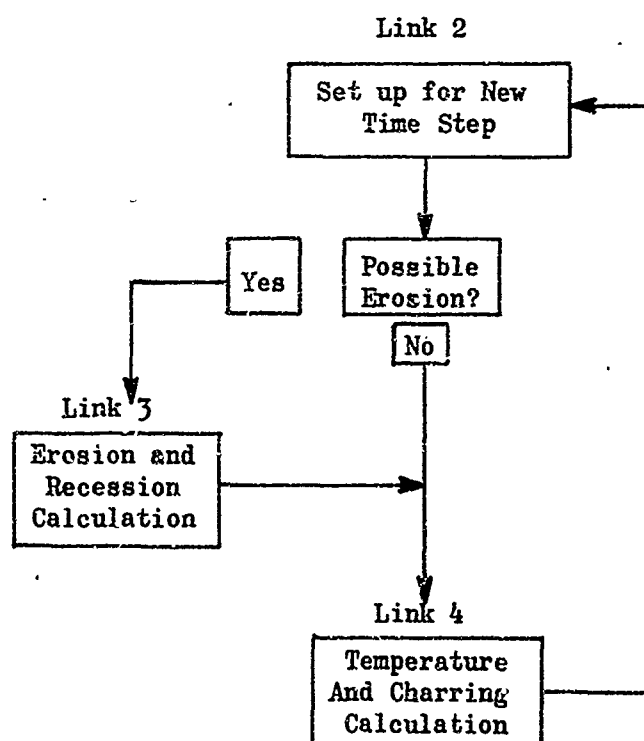
(b) Program flow in Link 2

Figure 4. Structure of the Relinked Program

19

visual display upon input signal of as many as 10 temperature-time graphs, each at a distinct specified regular interior point (see Fig. 2 for terminology) within the wall materials. This was accomplished by taking advantage of the available cathode ray tube equipment and the CRT library subroutines.

Improvement in Calculation of Gas Generation

Improvements were made in the portion of the program dealing with internal charring. First of all, the simulated boundary and initial conditions (pages 64 and 65, Ref. 2) for the solution of the continuity equation were altered to reduce initial lag in gas generation. In particular, the simulated boundary condition c, page 65, Ref. 2, should now read, in part, (see Fig. 5 for the point arrangement used to discretize the continuity equation) "If $T_{max,2}$ is less than T_{py} or if point 4 is a noncharring material, then G_2 is set equal to 0 " rather than "If either $T_{max,2}$ or $T_{max,4}$ is less than T_{py}....." Secondly, because the temperature may jump significantly into the pyrolysis range during a relatively large time step at mesh points close to an exposed surface, an upper limit for gas mass flux within a charring material can now be assigned as input to the program to prevent excessive initial interior gas generation and possible temperatu oscillation caused by overcooling.

These program changes were successfully checked out using the test case discussed above. As expected, the result was a graduated temperature reduction throughout the thrust chamber, the most significant reductions occurring at the heated inside surface.

Correction of Errors

In the cor se of performing the Task 2 and 3 efforts, a number of errors were uncovered. Most were of a strictly "programming" nature such as spelling and indexing of program variables. Correction of these errors did not alter results of previously run checkout cases because of the
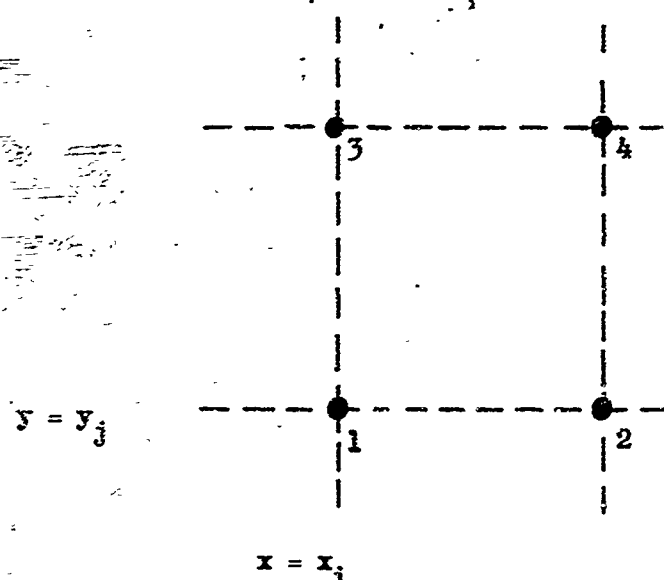
Figure 5. Point Arrangement for Discretizing the Continuity Equation

markedly different material and mesh line configurations. On the other hand, several other errors were discovered in the numerical interpretation of the model and were subsequently corrected. They were as follows.

Inspection of Eq. 9 above indicates that the values of G_j used in Eq. 9 were intended to be negative for all gaseous species ejected at the surface, as in Eq. 10. In the program, however, the plus sign in Eq. 9 was inadvertently written as a minus. Thus, the transpiration effect of the internally generated gases was reversed. For the checkout case discussed in the Review section, the effect of this error proved to be not overly significant.

Errors were found and corrected in the subroutines which predict erosion and recession at varying axial positions on the exposed inner surface and in the temperature calculation at these points after erosion. In the recession calculation, too few restrictions were placed on the number of loops of iteration permitted and on the number of circumstances under which the iterations would be permitted to continue, both in the calculation of Mach number and in the calculation of erosion rate. In the calculation of temperature after erosion has occurred, an error was found in the interpretation of the information supplied by the recession subroutines. In particular, an attempt had been made to bypass the direct simulation of Eq. 6 after erosion by employment of the value of $\partial T/\partial n$ as calculated iteratively in the recession subroutines. The nature of the iteration, however, is such that $\partial T/\partial n$ is evaluated at some intermediate time level between the old and new levels. The value required for the temperature calculation, on the other hand, must be obtained at the new level. Consequently, the short-cut procedure was abandoned and, Eq. 6 has been simulated directly in the program.

Alleviation of a Program Limitation

In several of the thrust chamber configurations treated during Task 3, the nozzle extension was taken to be a long narrow slanting strip of wall material. Because of the requirement of equal spacing of the horizontal (i.e., axially oriented) mesh lines, and the upper limit of 15 on the number of vertical mesh lines, it was necessary, in order to have a sufficient number of horizontal mesh lines for accuracy in the chamber and throat regions, to force too many into the narrow strip of extension material. The result was a violation, on several horizontal mesh lines in the strip, of a program limitation on the minimum number of points permitted per mesh line (four, as given in Rule 4 on page 79 of Ref. 2). As a consequence, a dummy subroutine was written which can be used when required to replace the restrictive subroutine (called HDAPT) and thus reduce the minimum from four to three (the latter being at present an irreducible minimum due to other program limitations as expressed by Rules 1 and 3 on pages 77 through 79, Ref. 2). The result of relaxing the four point limitation was, as expected, a worsening of the "condition" of the system of difference equations generated in the affected portions of the strip and, in particular, a certain amount of error in the calculated temperature in odd time steps at the intersections of the radiation-cooled outer boundary of the nozzle extension with some of the horizontal mesh lines. No transmitted ill effects, however, were observed (again, as expected) in the throat and chamber regions, which were of primary interest in the parametric study performed in Task 3.

TASK 1.A, RADIATIVE EXCHANGE AT THE EXPOSED INSIDE SURFACE

The effect of radiative exchange between axially varying portions of the inside wall surface was added as an optional (upon input signal) term of the effective heat transfer coefficient (see Eq. 7 and 8 above), as follows:

$$h_{rerad} = \frac{q_{rerad}}{T_{aw} - T} \qquad (14)$$

The approach taken in the program is to recalculate values of q_{rerad}, the reradiative heat flux, after each even time step at the boundary points P_i formed by the intersections of the radially oriented mesh lines, $x = x_i$, $i = 1, \ldots, n$, with the exposed inside surface, as follows:

$$q_{rerad,i} = \sum_{k=1}^{n} \sigma \epsilon F_{i,k} \left(T_k^4 - T_i^4 \right), \quad i = 1, \ldots, n \tag{15}$$

In Eq. 15, $F_{i,k}$ is the view factor* from an inside surface area represented by P_i to a similar area containing P_k. Included is the term with view factor $F_{i,i}$ because the inside surface area is in the shape of a ring and opposes itself as well as the remainder of the rings. The array obtained using Eq. 15 is then used for the succeeding two time steps in Eq. 14 to calculate the reradiative component of the effective heat transfer coefficient. In an odd step, values of q_{rerad} at boundary points lying at the ends of axially oriented mesh lines are obtained as needed by interpolation from the $q_{rerad,i}$ array.

Values of the two-dimensional array $F_{i,k}$ are obtained by interpolation at the points P_i from a similar input array $G_{j,\ell}$ defined at the input points Q_j at which the rest of the axially varying input data are specified, such as the adiabatic wall temperature and the convective heat transfer coefficient. This is performed in three stages in Link 1 of the program (the setup phase prior to the time step calculation), as follows:

1. Input and assignment of the two-dimensional array $G_{j,\ell}$, j, $\ell = 1$, ..., m, at the points Q_j and of a one-dimensional array B_j of associated disjoint surface subareas.

---

*The use of view factors in Eq. 15 instead of overall interchange factors (Ref. 8 and 9), which would include the effect of reflection, follows from the analysis in Tasks 2 and 3 of wall materials which emit nearly as black bodies. The net reflected heat fluxes are nearly zero and the interchange factors nearly equal to the view factors. Modification of the program to include reflection effects would be straightforward.

2. Direct calculation of a similar array A_i, $i = 1, \ldots, n$, of sub-areas associated with the P_i, each assumed conical, i.e.,

$$A_i = \pi \sqrt{1 + (f_i')^2} \; (x_{i+1/2} - x_{i-1/2}) \; [f_i' \; (x_{i+1/2} + x_{i-1/2}) +$$

$$2(f_i - x_i f_i')] \tag{16}$$

where $y = f(x)$ is the equation of the inside boundary curve and $f_i = f(x_i)$, and where $x_{i+1/2} = (x_i + x_{i+1})/2*$ defines the end points of the intervals over which the A_i are calculated. The generated array A_i is then normalized as follows:

$$\overline{A}_i = A_i \; \sum_{j=1}^{m} B_j / \sum_{k=1}^{n} A_k, \tag{17}$$

so as to satisfy the following normalization condition (where, for convenience of notation, we drop the bar on the A_i):

$$\sum_{i=1}^{n} A_i = \sum_{j=1}^{m} B_j. \tag{18}$$

Finally a two-sweep linear interpolation is performed to obtain the $F_{i,k}$ at the points P_i from the $G_{j,\ell}$ at the points Q_j in such a way as to satisfy the following two normalization conditions:

$$\sum_{k=1}^{n} H_{j,k} = \sum_{\ell=1}^{m} G_{j,\ell}, \quad j = 1, \ldots, m, \tag{19}$$

$$\sum_{i=1}^{n} A_i F_{i,k} = \sum_{j=1}^{m} B_j H_{j,k}, \quad k = 1, \ldots, n, \tag{20}$$

---

*This definition of $x_{i+1/2}$ is applicable only for $i = 1, 2, \ldots, n-1$. $x_{1/2}$ and $x_{n+1/2}$ are taken to be the leftmost and rightmost axial positions, respectively, of the exposed inside surface.

where $H_{j,k}$, $j=1, \ldots, m$, $k=1, \ldots, n$, is an interim two-dimensional array of view factors, from the points Q_j to the points P_i, obtained during the first sweep of interpolation.

To make use of the added Task 1.A program capability, it is necessary to obtain reasonable values for the input view factors $G_{j,\ell}$ and associated areas B_j for each contemplated thrust chamber configuration. For checkout purposes, an extension of the disk method developed by Dr. Simon deSoto of Rocketdyne (Ref. 10) was used to generate the $G_{j,\ell}$ and is described in some detail in Appendix A. The disk method is exact for the case of conical subareas, none of which are occulted or shaded from each other. Because the occultations in the checkout case were not severe (Fig. 3), the formulas were used as if no occultations existed. No rigorous method was found in the literature which would yield view factors from all portions of a converging-diverging thrust chamber to each other portion, including the effects of occultation and shading.*

The input subareas B_j employed in the test case used for checkout were obtained through application of Eq. 16 at points Q_j rather than P_i.**Values of the B_j and $G_{j,\ell}$ arrays used for the Task 1.A checkout are given in Table 1, and the arrangement of the subareas and their approximation by conical rings are depicted in Fig. 6. The other properties and heating conditions used for the checkout comparison can be found in Table 4 of Ref. 2. The checkout run made with reradiation was terminated after 12 seconds of steady firing. Comparisons of computed surface temperature histories with the previously obtained results are given in Fig. 7 and 8. As expected, temperatures computed with reradiation effects included were lower in the vicinity of the throat and higher in the chamber and exit sections.

---

*A rigorous procedure is presently being developed at Rocketdyne. When available, it would be desirable to program the method and incorporate it as a subroutine of Link 1 in 2D-ABLATE. This would eliminate a great deal of arduous computation, necessary, for example, for application of the disk method using a desk calculator.

**Selection of the end points $x_{j+1/2}$ (corresponding to the $x_{i+1/2}$ in Eq. 16) is not restricted to midpoints between the x_j. Instead, because judgement can be more readily exercised in a hand calculation, they can be taken at any p'nt between the x_j. Generally, they should be chosen on a geometrical basis so as to yield subsurfaces which are most nearly conical in shape.

TABLE 1

SUBAREAS B_j AND VIEW FACTORS $G_{i,j}$ USED AS INPUT FOR TASK 1.A CHECKOUT

B_j →	12.8805	25.7610	28.3371	58.1157	43.4815	20.3167	14.8312	49.1049	42.6188	19.2323
$G_{i,j}$										
j\i → / i↓	1	2	3	4	5	6	7	8	9	10
1	0.08103	0.10504	0.09764	0.14434	0.06005	0.01360	0.00760	0.00514	0.00327	0.00104
2	0.05252	0.13633	0.10835	0.17593	0.07489	0.01723	0.00959	0.00724	0.00442	0.00160
3	0.04438	0.09850	0.14694	0.22795	0.10094	0.02391	0.01331	0.01140	0.00665	0.00254
4	0.03199	0.07798	0.11115	0.26183	0.15089	0.03917	0.02104	0.02663	0.01298	0.00417
5	0.01779	0.04437	0.06578	0.20167	0.24612	0.08939	0.04835	0.07050	0.02884	0.00847
6	0.00862	0.02185	0.03335	0.11205	0.19131	0.14233	0.09084	0.13?8	0.05725	0.01990
7	0.00660	0.01666	0.02543	0.08245	0.14169	0.12444	0.10653	0.19440	0.07585	0.01792
8	0.00155	0.00380	0.00658	0.03154	0.06243	0.05767	0.05874	0.24652	0.12817	0.04044
9	0.00099	0.00267	0.00442	0.01770	0.02942	0.02729	0.02640	0.14768	0.17525	0.05553
10	0.00070	0.00214	0.00345	0.01260	0.01915	0.02102	0.01382	0.10325	0.12305	0.09045
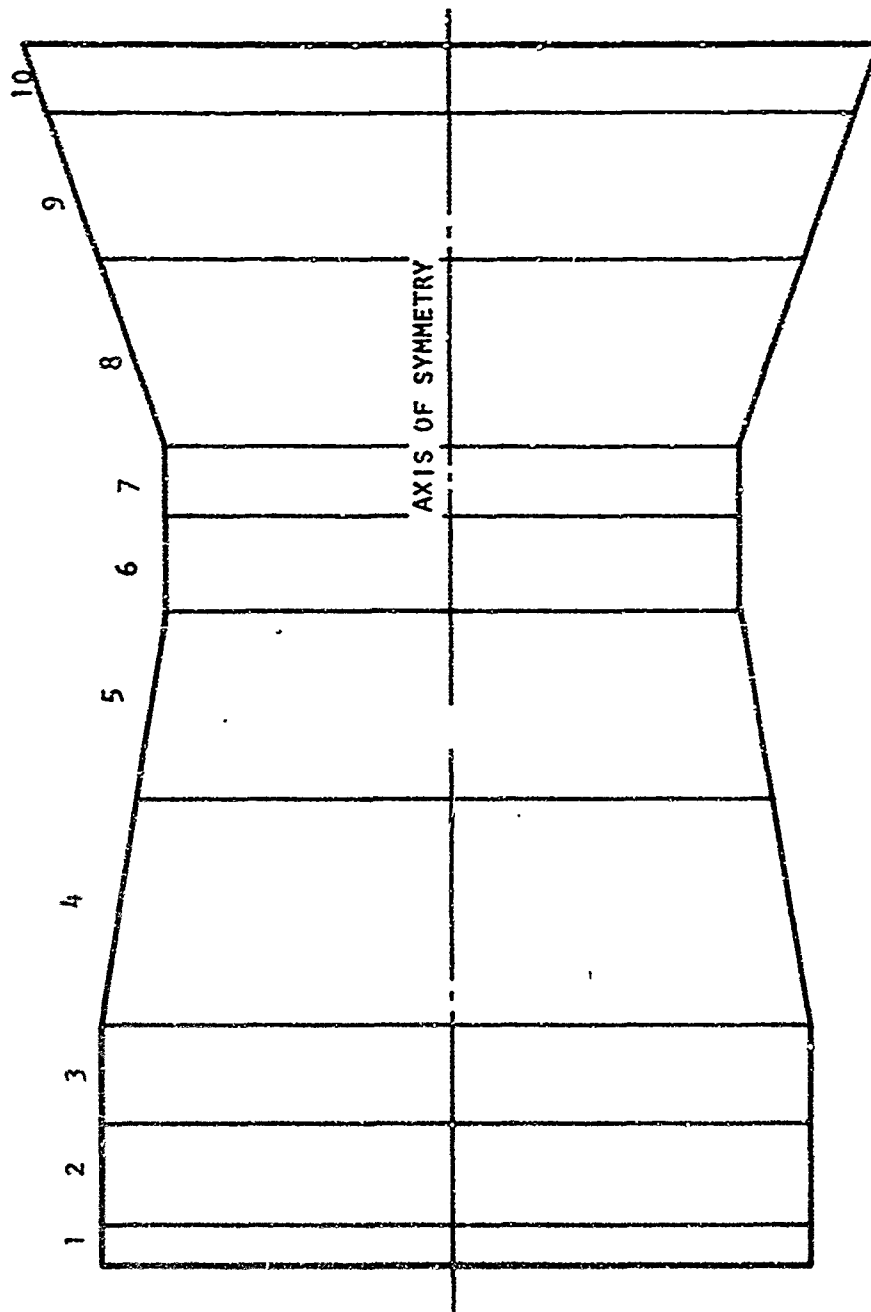
Figure 6. Subareas, B_j, $j=1,\ldots,10$, Used to Calculate Input View Factors $G_{j,\ell}$ for the Checkout of Task 1.A
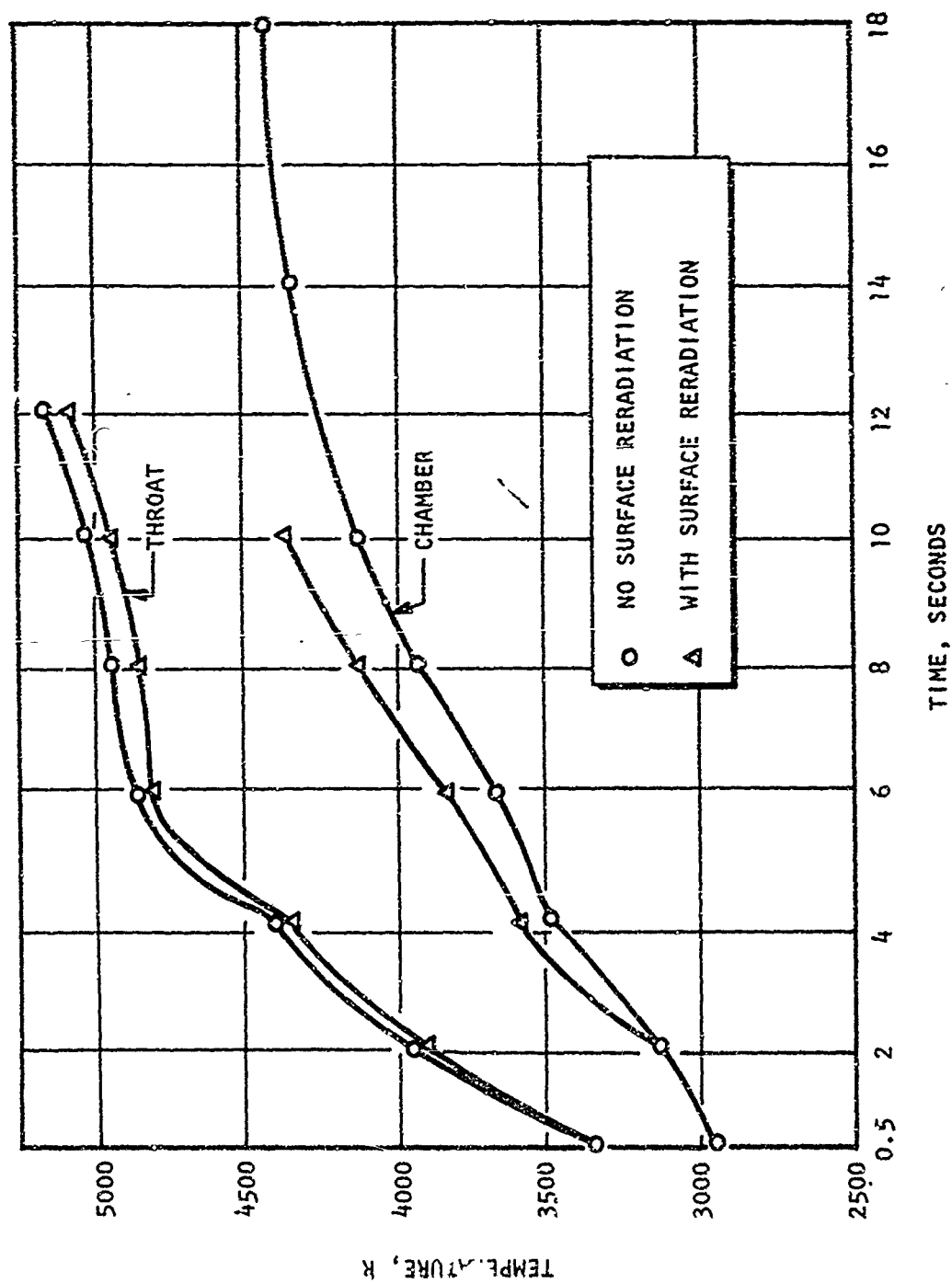
Figure 7 . Comparison of Surface Temperature Histories Computed in Checkout of Task 1.A for the Chamber Zone and Throat Region
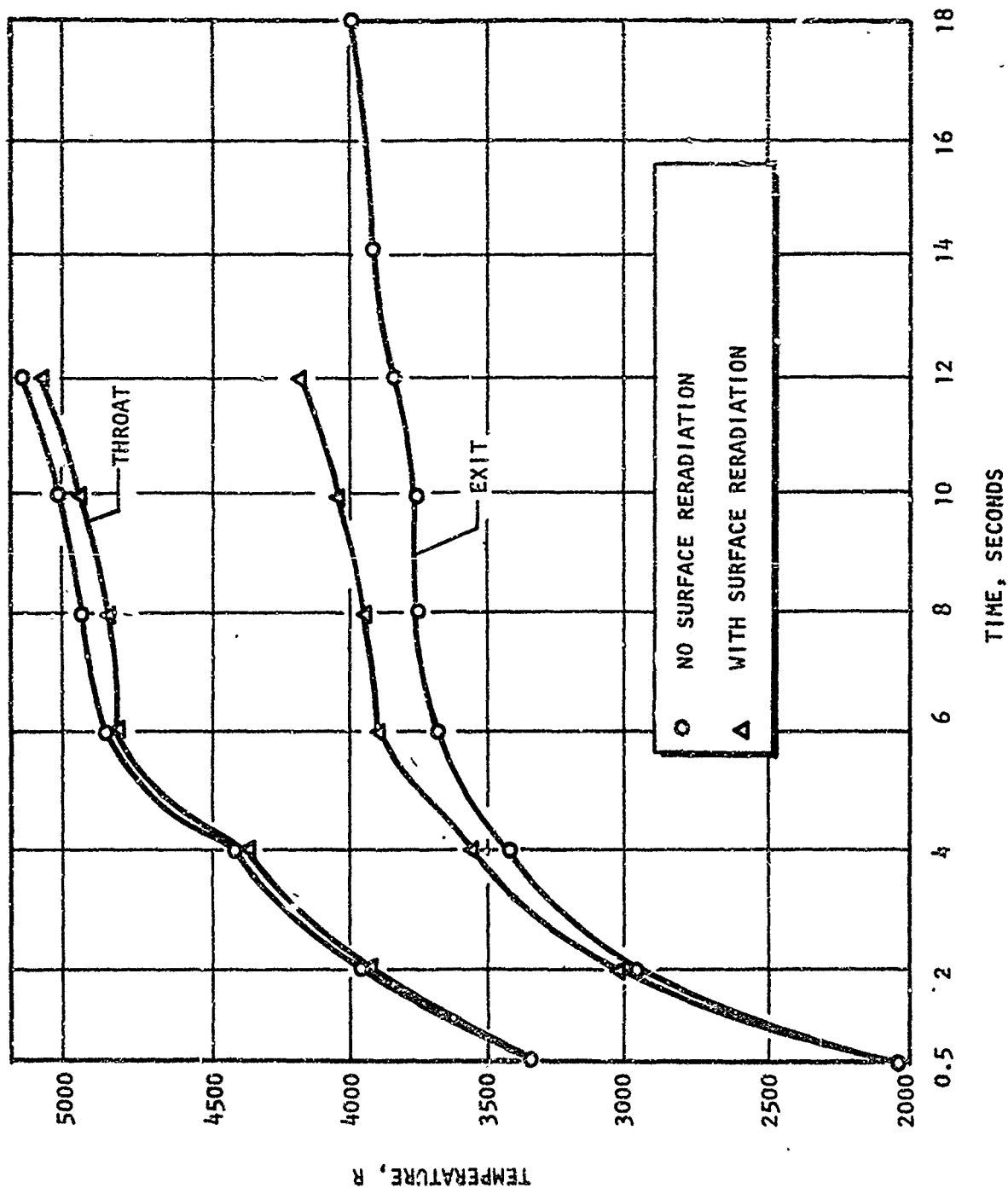
Figure 8 . Comparison of Surface Temperature Histories Computed in Checkout of Task 1.A for the Throat Region and Exit Nozzle

TASK 1.B, THERMAL ANALYSIS OF ANISOTROPIC MATERIALS

The 2D-ABLATE program was extended to permit (upon input signal) any of
the wall materials to be anisotropic; i.e., to possess two different con-
ductivities, each temperature dependent, one in the major direction (highest
conductivity) and the other in the minor direction (lowest conductivity) per-
pendicular to the major direction. Many wall materials of current interest
are strongly anisotropic such as phenolic-refrasil and phenolic-carbon
cloth laminates, which were analyzed in some detail in Task 2 and 3 of
the present program.

For treatment of anisotropic materials, modifications were necessary in
the formulation and discretization of the model as expressed by Eq. 1
through 11 given above. The overall solution procedures, however, were
substantially unchanged. A discussion follows of the changes made and
their effect on program results.

Model Changes

For an anisotropic wall material with conductivities $K_\eta(T)$ and $K_\xi(T)$ in
the major (η) and minor (ξ) directions and a counterclockwise displacement
θ^* of these directions from the radial (y) and axial (x), the following
version of the energy equation was derived (see Appendix B), in which,
for generality, both conduction and charring are accounted for:

$$(\rho C)_{eff} \frac{\partial T}{\partial \tau} = \frac{\partial}{\partial x}\left(K_x \frac{\partial T}{\partial x}\right) + \frac{1}{y}\frac{\partial}{\partial y}\left(yK_y \frac{\partial T}{\partial y}\right) - \frac{dH}{dT}\left(G_x \frac{\partial T}{\partial x} + G_y \frac{\partial T}{\partial y}\right) +$$

$$2K_{xy} \frac{\partial^2 T}{\partial x \partial y} + 2 \frac{dK_{xy}}{dT} \frac{\partial T}{\partial x} \frac{\partial T}{\partial y} \tag{21}$$

---

*It should be emphasized that θ is not what is commonly termed the orienta-
tion (or angle of wrap), the latter conventionally being taken as the clock-
wise rotation from the axial to the major direction.

where

$$K_x = K_\xi \cos^2\theta + K_\eta \sin^2\theta$$

$$K_y = K_\xi \sin^2\theta + K_\eta \cos^2\theta \qquad (22)$$

$$K_{xy} = (K_\xi - K_\eta) \sin\theta \cos\theta$$

and where $(\rho C)_{eff}$ is used to abbreviate the coefficient of $\partial T/\partial \tau$ on the left side of Eq. 1.

For use in the boundary and interface heat flux conditions, given by Eq. 6 and 11 above, the following expression was obtained (see Appendix B) for the conductivity in the normal direction n at the bounding surface:

$$K_n = \left[\left(\frac{\partial f}{\partial x}\right)^2 K_x - 2 \frac{\partial f}{\partial x} K_{xy} + K_y \right] / \left[1 + \left(\frac{\partial f}{\partial x}\right)^2 \right] \qquad (23)$$

where $\partial f/\partial x$ is the slope of the boundary curve, $y=f(x,\tau)$.

No direct changes were required for the anisotropic analysis in Eq. 2, the continuity equation for the mass flux of generated gases within a charring material. The direction of flow, however, in an anisotropic material, as characterized by the ratio of G_x to G_y, is now assumed to be oriented with the heat flux vector, as follows*:

$$G_x/G_y = K_x \frac{\partial T}{\partial x} / K_y \frac{\partial T}{\partial y} \qquad (24)$$

which is seen to be compatible with Eq. 3 above for an isotropic material; i.e., when $K_x = K_y$. It can be shown that Eq. 24 closely approximates the expression $G_\xi/G_\eta = (K_\xi \, \partial T/\partial \xi)/(K_\eta \partial T/\partial \eta)$.

---

*An alternative assumption, which was not employed, would have taken the direction of flow to be in the major direction η of conductivity; i.e., $G_x/G_y = -\tan\theta$. It was felt, however, that in general Eq. 24 would be more appropriate.

Discretization of $\partial^2 T/\partial x \partial y$

The numerical solution of the model equations for the case of an aniso-
tropic material was obtained with a time step procedure using finite dif-
ferences as in the isotropic case outlined above and detailed in Ref. 2.

Discretization of the anisotropic energy equation, however, required def-
inition of a finite difference analog of the mixed derivative $\partial^2 T/\partial x \partial y$.
For the remaining derivatives of Eq. 21, the centered first and second
spatial difference operators, δ_x, δ_x^2, δ_y, δ_y^2, and the first time dif-
ference were employed as defined by Eq. 19 through 23 of Ref. 2.

At an interior point 0 whose horizontally, vertically, and diagonally ad-
jacent points are all regular (see Fig. 2 for definition of regular point)
and where the points are equidistant (as in Fig. 9a for $\Delta x_A = \Delta x_C = \Delta x$
and $\Delta y_B = \Delta y_D = \Delta y$), the following standard mixed difference analog
could have been used with second order accuracy (See Appendix C for
derivation):

$$\delta_{xy}^2 \, T_0 = (T_E - T_F + T_G - T_H) \, / \, 4 \, \Delta x \, \Delta y \qquad (25)$$

In the case of nonequal spacing (as occurs in 2D-ABLATE in the x-direction),
the following similar analog could also have been applied:

$$\delta_{xy}^2 \, T_0 = (T_E - T_F + T_G - T_H) \, / \, (\Delta x_A + \Delta x_C)(\Delta y_B + \Delta y_D) \qquad (26)$$

but only with first order accuracy; i.e., with $0(\Delta x_A - \Delta x_C) + 0(\Delta y_B - \Delta y_D)$ accuracy (which improves to second order accuracy when the points are
equidistant as in Eq. 25 and thus might be termed accurate of order $3/2$
because it is effectively between first and second). This would have been
quite satisfactory in the approximation of the energy equation because of
the similar truncation error obtained in the discretization of the second
spatial derivatives. Neither Eq. 25 nor 26, however, are employed in 2D-
ABLATE because they too often are inapplicable; i.e., if, for a given
interior point 0, one or more of the points, E, F, G, and H do not lie in
the same material because of interposition of boundaries or interfaces
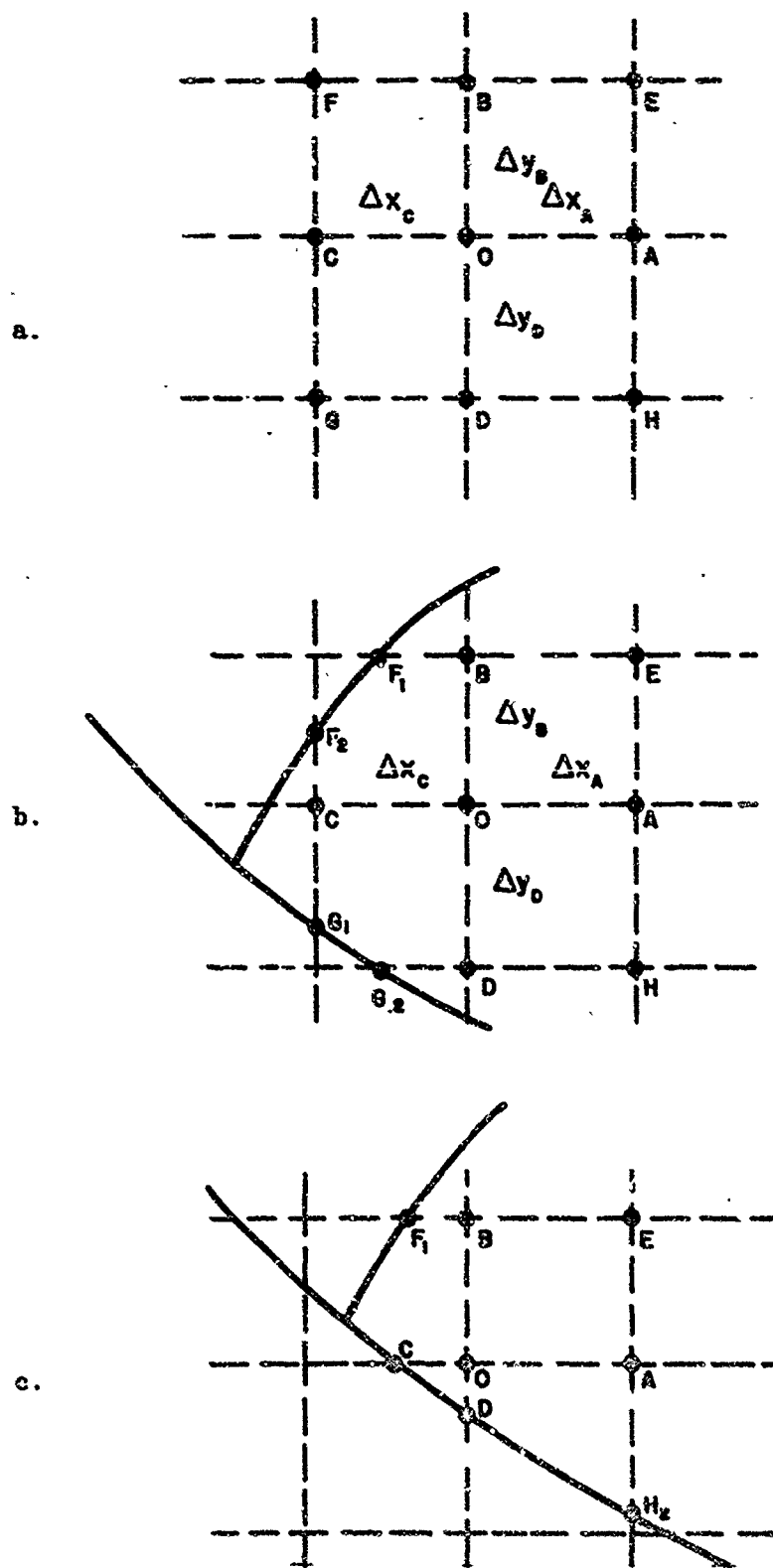
Figure 9.   Various Mesh-Boundary Configurations Affecting
Formulation of Difference Analog $\delta^2_{xy} T_o$

(as in Fig. 9b, for example). What is required instead in such a case
is a difference analog involving temperatures at the intercepted irregular
boundary or interface points (such as F_1, F_2, G_1, and G_2 in Fig. 9b). On
the other hand, to formulate a separate difference analog for each such
combination of irregular points (Fig. 9b depicting just one possible com-
bination) would be a difficult task. Instead, the following second order
accurate mixed difference analogs were derived (see Appendix C), one for
odd and one for even time steps, which treat all cases of the type shown
in Fig. 9b because of their formulation in terms of temperature gradients
at the horizontally and vertically adjacent points instead of temperatures
at the diagonal points.

Odd Step:

$$\delta^2_{xy} T_0 = \left[\Delta x_C^2 \, \delta_y T_A - (\Delta x_C^2 - \Delta x_A^2)\delta_y T_0 - \Delta x_A^2 \, \delta_y T_C \right] /$$

$$\left[\Delta x_A \, \Delta x_C \, (\Delta x_A + \Delta x_C) \right] \quad (27)$$

Even Step:

$$\delta^2_{xy} T_0 = \left[\Delta y_D^2 \, \delta_x T_B - (\Delta y_D^2 - \Delta y_B^2) \, \delta_x T_0 - \Delta y_B^2 \, \delta_x T_D \right] /$$

$$\left[\Delta y_B \, \Delta y_D \, (\Delta y_B + \Delta y_D) \right] (28)$$

Using the definitions given in Ref. 2 of the second order accurate differ-
ence operators, δ_x and δ_y, it can be seen that if, as in Fig. 9a, all of
the adjacent points A, B, C, D, E, F, G, and H are regular and in the
same material, then Eq. 27 and 28 are identical (but do not reduce to the
less accurate first order analog expressed by Eq. 26). If, further, the
spacing is equal, both reduce to Eq. 25.

Equations 27 and 28 are employed in the 2D-ABLATE program for the discre-
tization of the anisotropic energy equation at each interior point 0 whose
horizontally and vertically adjacent points A, B, C, and D are also interior

35

points. If, however, any of these points are boundary or interface points (as in Fig. 9c, for example), then either Eq 27 or 28 or both are not applicable directly. This is caused by the difficulty encountered in expressing the first differences $\delta_x T_B$, $\delta_x T_D$, $\delta_y T_A$, or $\delta_y T_C$ when the points B, D, A, or C are irregular. The same problem arose (described in Ref. 2, pages 47 through 53, and indicated in the Review section above) in obtaining a second order accurate difference analog to $\partial T/\partial n$ for use in boundary and interface conditions at irregular points. Here we do not employ the same device used for maintaining second order accuracy; i.e., permitting conversion from $\partial T/\partial x$ to $\partial T/\partial y$ at points B and D or from $\partial T/\partial y$ to $\partial T/\partial x$ at A and C by essentially letting $\partial T/\partial s$ vanish and using the equivalent condition, $\partial T/\partial x = -\partial f/\partial x\, \partial T/\partial y$, for the conversion. Instead we revert to first or even zero order accuracy, in the event of irregular points, by replacing Eq. 27 and 28, as follows:

Odd Time Step:

$$\delta^2_{xy} T_0 = \begin{cases} \dfrac{\delta_y T_A - \delta_y T_0}{\Delta x_A} & \text{if A is regular and C is irregular} \\[3ex] \dfrac{\delta_y T_0 - \delta_y T_C}{\Delta x_C} & \text{if C is regular and A is irregular} \\[3ex] 0 & \text{if A and C are irregular} \end{cases} \qquad (29)$$

Even Time Step:

$$\delta^2_{xy} T_0 = \begin{cases} \dfrac{\delta_x T_B - \delta_x T_0}{\Delta y_B} & \text{if B is regular and D is irregular} \\[3ex] \dfrac{\delta_x T_0 - \delta_x T_D}{\Delta y_D} & \text{if D is regular and B is irregular} \\[3ex] 0 & \text{if B and D are irregular} \end{cases} \qquad (30)$$

Discretization of the Energy Equation

The discretization of the anisotropic energy equation was performed as in the isotropic case in accordance with the linearization of the generalized Peaceman-Rachford alternating direction method as expressed by Eq. 30 through 32, Ref. 2. Tridiagonality of the systems of difference equations generated was maintained by evaluating the mixed difference analogs, as given by Eq. 27 through 30, at the old time level (i.e., at time τ_k in the time step, $\tau_k \to \tau_{k+1}$) rather than the new. Similarly, discretization of the term $2 K'_{xy}(T) \, \partial T/\partial x \, \partial T/\partial y$ was performed so as to maintain linearity and tridiagonality of the difference equations by taking $\delta_y T$ at the old time level and $\delta_x T$ at the new in an odd time step and reversing the assignment in an even step. Thus, in odd and even time steps, the anisotropic difference equations take the following form (where, following the notation of Ref. 2, Eq. 31 and 32, the spatial subscript 0 is omitted but is understood to apply to each parameter appearing):

Odd Step $\left(\tau_k \to \tau_{k+1} \right)$:

$$
(\rho c)_{\text{eff},k} \frac{T_{k+1} - T_k}{\Delta \tau} = K_{x,k} \, \delta_x^2 \, T_{k+1} + \left(K'_{x,k} \; \delta_x T_k - \frac{\delta_x H_k}{\delta_x T_k} \, G_{x,k} + \right.
$$

$$
\left. K'_{xy,k} \; \delta_y T_k \right) \delta_x T_{k+1} + K_{y,k} \, \delta_y^2 \, T_k + \left(\frac{K_{y,k}}{j \, \Delta y} + K'_{y,k} \; \delta_y T_k - \right.
$$

$$
\left. \frac{\delta_y H_k}{\delta_y T_k} \, G_{y,k} + K'_{xy,k} \; \delta_x T_k \right) \delta_y T_k + 2 K_{xy,k} \, \delta_{xy}^2 \, T_k \qquad (31)
$$

Even Step ($\tau_{k+1} \to \tau_{k+2}$):

$$(\rho c)_{eff,k+1} \frac{T_{k+2} - T_{k+1}}{\Delta \tau} = K_{x,k+1} \, \delta_x^2 T_{k+1} + \left(K'_{x,\,k+1} \, \delta_x T_{k+1} - \right.$$

$$\frac{\delta_x H_{k+1}}{\delta_x T_{k+1}} G_{x,k+1} + K'_{xy,\,k+1} \, \delta_y T_{k+1} \Big) \, \delta_x T_{k+1} + K_{y,k+1} \, \delta_y^2 T_{k+2} +$$

$$\left(\frac{K_{y,k+1}}{j \, \Delta y} + K'_{y,\,k+1} \, \delta_y T_{k+1} - \frac{\delta_y H_{k+1}}{\delta_y T_{k+1}} G_{y,k+1} + K'_{xy,\,k+1} \, \delta_x T_{k+1} \right) \delta_y T_{k+2} +$$

$$2 K_{xy,\,k+1} \, \delta_{xy}^2 T_{k+1} \qquad\qquad (32)$$

The notation used in subscripting and differencing the parameters, which
follows that of Ref. 2, Eq. 31 and 32, should be self-evident. In parti-
cular, $\delta_x H_k / \delta_x T_k$ and $\delta_y H_{k+1} / \delta_y T_{k+1}$ are used instead of the known values
$H'(T_k)$ and $H'(T_{k+1})$, as explained in Ref. 2, to ensure inclusion of all
heat absorption effects when the distance increments used are so large
that entire temperature intervals might be passed over in which $H'(T)$ is
relatively large. Also, $j \, \Delta y = y_j$, the height of the $j\underline{th}$ axial mesh line.

Revised Programming Procedures

The 2D-ABLATE program was modified for treatment of anisotropic materials
in the input and setup procedures of Link 1 and in the time step calculation
performed in Links 2, 3, and 4 (see the Review section).

Upon input signal, any of the five wall materials can be anisotropic. For
each anisotropic material, the input data include the major and minor con-
ductivities, $K_\eta(T)$ and $K_\xi(T)$, read in as piecewise quadratic functions of
temperature, and the counterclockwise angular displacement θ of the η
and ξ directions from y and x. The anisotropic input in Link 1 is then
transformed to equivalent conductivities in the axial, radial, and "mixed"
directions for later use in Links 2, 3, and 4. The transformation is
accomplished by use of Eq. 22.

The time step calculation is performed in Links 2, 3, and 4 as outlined in Ref. 2, with modifications in the solution procedure to account for the changes given above in Eq. 20 through 24 and 27 through 32.

In the solution of the energy equation, a separate function subprogram was used to calculate the difference analog of the mixed temperature derivative, thus providing the capability of testing and evaluating alternative formulations to that given by Eq. 27 through 30. The only alternative subprogram written thus far is one that simply sets the mixed difference identically to zero. This was used, as will be seen in the checkout section below, to help assess the significance of the mixed derivative term.

Checkout of the Anisotropic Capability

Checkout of the anisotropic program capability was performed by comparison to previously obtained results with carbon cloth-phenolic treated as isotropic (the same control case used to check out Task 1.A and discussed in the Review section, see Fig. 3). Assumed values were used for the anisotropic input data. Because checkout was not performed with respect to measured results but only by comparison to computed isotropic results, designation of checkout as successful or unsuccessful was a qualitative decision based on the predictability of the direction rather than the degree of deviation of the anisotropic results from the isotropic. Thus, the objective of the checkout was to see whether the anisotropic results deviated from the isotropic in a predictable manner, over a representative range of orientations, using assumed anisotropic conductivities as input which differed only slightly from the isotropic values.

Cases evaluated included orientations of 0, 45, 90, and 135 degrees, in which major and minor conductivities (both temperature dependent) differed from the isotropic conductivity by a constant (Fig.10). An orientation of 45 degrees only was employed for another case in which the difference

39
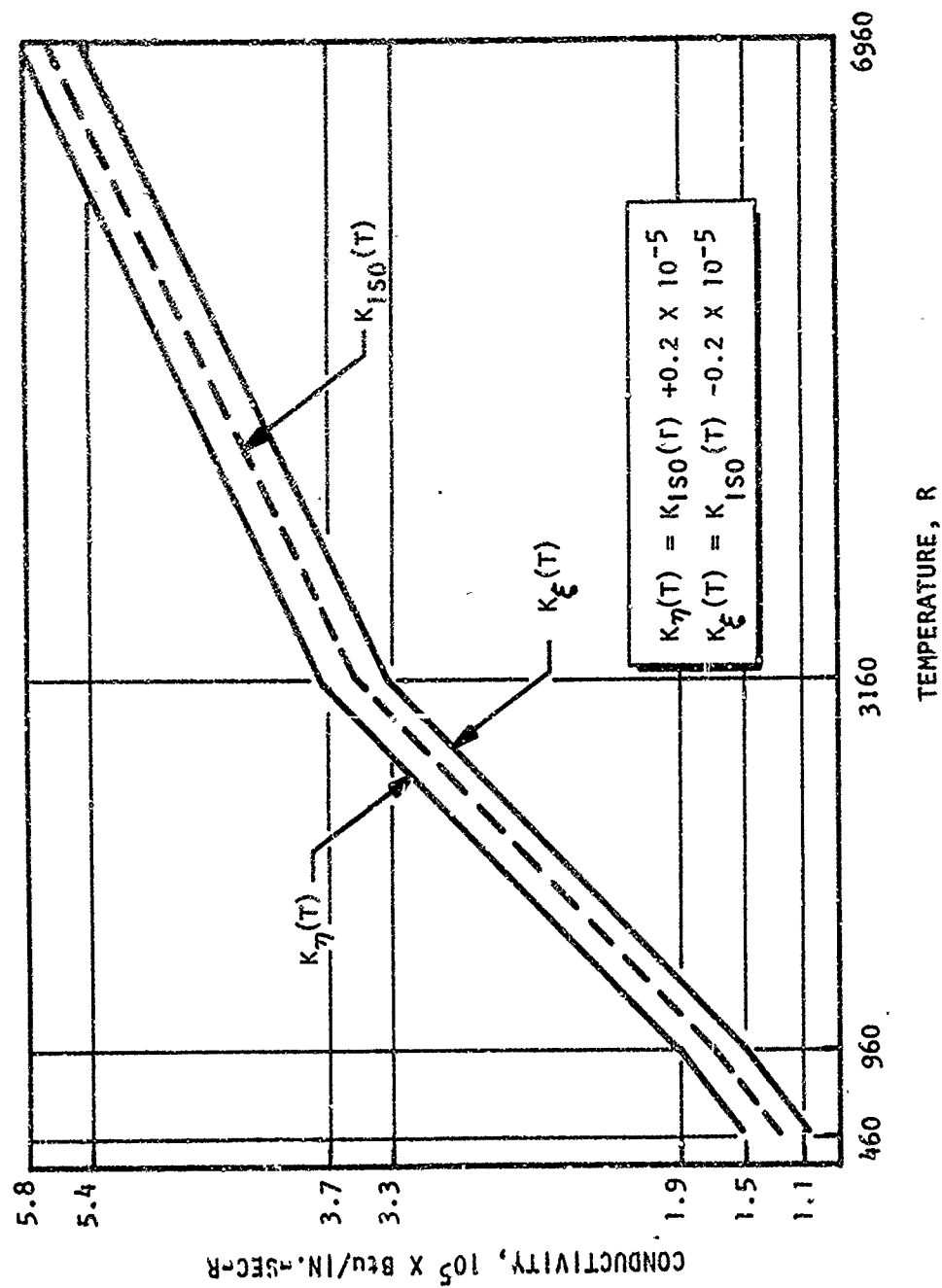
Figure 10 . Anisotropic Conductivity for Checkout

$$K_\eta(T) = K_{ISO}(T) + 0.2 \times 10^{-5}$$
$$K_\xi(T) = K_{ISO}(T) - 0.2 \times 10^{-5}$$

40

between conductivities varied with temperature by permitting the aniso-
tropic conductivities to vary linearly with the known isotropic conduc-
tivity, as follows:

$$K_\eta(T) = 1.1 \; K_{iso}(T), \; K_\xi(T) = 0.9 \; K_{iso}(T).$$

All cases were first run using the subprogram which provides a vanishing
mixed difference in the energy equation and then with the second order
analog expressed by Eq. 27 through 30. In this way, various anisotropic
effects could be isolated and evaluated separately.

The results of the checkout are given in Fig. 11 in the form of a comparison
of surface and interior temperatures obtained for the various orientations
(cases a through e) after 12 seconds of firing. The classification of
cases a through e (Fig. 11) will be maintained throughout the remainder
of the discussion. Temperatures given in parentheses (Fig. 11) are those
obtained with a vanishing mixed temperature difference in the energy equa-
tion. Cases a, c, and d are analyzed below in detail, and Case e in
somewhat less detail. Case b is not discussed because the reasoning employed
was similar to that of Case a.

Case a. 45-degree orientation ($\theta = 45$ degrees*), $K_x = K_y = K_{iso}(T)$,
$K_{xy} = -0.2 \; (10^{-5})$, $K'_{xy} = 0$. At the inside surface, the normal conductivity
is obtained from Eq. 23 as follows:

$$K_n = \left[\left(\frac{\partial f}{\partial x} \right)^2 K_x + K_y - 2 \frac{\partial f}{\partial x} K_{xy} \right] \bigg/ \left[1 + \left(\frac{\partial f}{\partial x} \right)^2 \right] = K_{iso} \div$$
$$0.2 \frac{\partial f}{\partial x} (10^{-5}) \bigg/ \left[1 + \left(\frac{\partial f}{\partial x} \right)^2 \right].$$

---

*In general, to calculate the equivalent value of θ for a given orientation
α, we can use $\theta = 90 - \alpha$ degrees for $0 \le \alpha \le 90$ degrees; $\theta = 270 - \alpha$ degrees
for $90 < \alpha < 180$ degrees

304 STAINLESS STEEL

PHENOLIC–CARBON CLOTH

20-Degree Slope

10-Degree Slope

T_{ISO} = 4232 R
a. 4216 (,4202°)
b. 4251° (,4255°)
c. 4212°
d. 4259°
e. 4199° (,4190°)

T_{ISO} = 1293 R
a. 1321° (,1289°)
b. 1273° (,1303°)
c. 1341°
d. 1252°
e. 1336° (,1310°)

T_{ISO} = 5175 R
a. 5169° (,5165°)
b. 5185° (,5185°)
c. 5161°
d. 5212°
e. 5164° (,5159°)

T_{ISO} = 1122 R
a. 1123° (,1120°)
b. 1121° (,1121°)
c. 1197°
d. 1046°
e. 1124° (,1122°)

T_{ISO} = 5053 R
a. 5063° (,5075°)
b. 5047° (,5036°)
c. 5024°
d. 5081°
e. 5069° (,5084°)

T_{ISO} = 1522 R
a. 1508° (,1529°)
b. 1537° (,1514°)
c. 1567°
d. 1474°
e. 1497° (,1517°)

Case Treated	Orientation		Conductivity
ISOTROPIC $K_{ISO}(T)$	Nose		$K_x = K_y = K_{ISO}$ $K_{xy} = 0$
ANISOTROPIC	a. 45°	$(\theta = 45°)$	$K_x = K_y = K_{ISO}$ $K_{xy} = -C$
$K_\eta(T) =$ $K_{ISO} + C,$	b. 135°	$(\theta = 135°)$	$K_x = K_y = K_{ISO}$ $K_{xy} = C$
$K_\xi(T) =$ $K_{ISO} - C,$	c. 90°	$(\theta = 0°)$	$K_x = K_\xi, K_y = K_\eta$ $K_{xy} = 0$
$C = 0.2 \times 10^{-5}$	d. 0°	$(\theta = 90°)$	$K_x = K_\eta, K_y = K_\xi$ $K_{xy} = 0$
$K_\eta(T) = 1.1 K_{ISO}$ $K_\xi(T) = 0.9 K_{ISO}$	e. 45°	$(\theta = 45°)$	$K_x = K_y = K_{ISO}$ $K_{xy} = -0.1 K_{ISO}$

Figure 11. Anisotropic Checkout Cases, Comparison of Temperatures After 12 Seconds of Firing

42

Therefore, to the left of the throat, we have $K_n < K_{iso}$ because $\partial f/\partial x < 0$, and thus we should have $T_{aniso} > T_{iso}$ at the surface. This inequality is satisfied in Fig. 11, the calculated values being $T_{aniso} = 5063$ R and $T_{iso} = 5053$ R. To the right of the throat, the reverse tendency is reflected (Fig. 11); T_{aniso} is 16 R less than T_{iso}.

It might be argued that a 10 or 16 degree difference is smaller than the expected error in the temperature and therefore should be disregarded as not being significant. This reasoning would be false because we are comparing two calculated temperatures, not a calculated temperature with a measured temperature. There are several sources of error in this sort of calculation. One error is caused by the assumption of a nonrealistic model and is a discrepancy between real temperatures and idealized temperatures. Another error is caused by the method of solution and is a measure of how closely the numerical solution of the finite difference equations approximates the exact solution of the continuous model ⊦ ɜ. Both of these errors can be quite large. However, neither applies to the present discussion because we are comparing two values which are calculated numerically from almost identical input data. Thus, as long as the numerical procedures are reasonably accurate and stable, the difference between the two calculated values need not be large to be significant. As will be shown, the consistency with which the expected trends are reflected in the calculated results indicates that these differences, though small, are indeed significant.

To evaluate the interior temperatures attained, two subcases must be analyzed. First, in the calculation made with a vanishing mixed temperature difference (i.e., with $\delta^2_{xy} T = 0$) we see that, because K'_{xy} is zero as well and $K_x = K_y = K_{iso}$, the anisotropic energy equation reduces identically to the isotropic case. Thus, any interior anisotropic effect felt

must be only a reflection of the surface effect.* This is borne out in the temperatures calculated, where $T_{aniso} = 1529° > 1522° = T_{iso}$ to the left of the throat and $T_{aniso} = 1289° < 1293° = T_{iso}$ to the right of the throat. In the second subcase, that calculated with $\frac{\partial^2}{\partial x \partial y} T$ as expressed by Eq. 27 through 30, we see that the only difference in the energy equation is caused by the presence of the mixed derivative. Thus, we can write

$$\rho C \left. \frac{\partial T}{\partial \tau} \right|_{aniso} \simeq \rho C \left. \frac{\partial T}{\partial \tau} \right|_{iso} -0.4 \; (10^{-5}) \; \frac{\partial^2 T}{\partial x \partial y} \; . \tag{33}$$

Here we have isolated the mixed derivative term of the energy equation so that the present subcase serves as a partial check of the significance of the second-order mixed difference analog by comparison of results with the subcase in which the vanishing mixed difference was employed.

Because of the gradients caused by surface heating, $\partial^2 T/\partial x \partial y$ will in general be positive to the left of the throat and negative to the right of the throat. This is caused by generally decreasingly negative $\partial T/\partial x$ and $\partial T/\partial y$ with increasing y and x, respectively, to the left of the throat and by increasingly positive $\partial T/\partial x$ and negative $\partial T/\partial y$ with increasing y and x, respectively, to the right of the throat. Therefore, we see from Eq. 33 that T_{aniso} should tend to increase with time more slowly than T_{iso} to the left of the throat and more rapidly to the right. Thus, except near the surface where the reverse effect dominates as discussed above, we should have $T_{aniso} < T_{iso}$ to the left of the throat and $T_{aniso} > T_{iso}$ to the right. Again, we see that these tendencies are reflected in the calculated interior temperatures ($T_{aniso} = 1508° < 1522° = T_{iso}$ to the left of the throat and $T_{aniso} = 1321° > 1293° = T_{iso}$ to the right). Thus, the interior anisotropic effect is the reverse of the surface effect and should be accounted for by use of a nonvanishing mixed

---

*This subcase illustrates the value of simulating the boundary curves $y = f(x,\tau)$ accurately in the analysis because the only anisotropic effect in the solution is felt in the value of K_n, which depends directly on the slope $\partial f/\partial x$. To achieve a similar effect with alternately horizontal and vertical segments using K_x and K_y respectively would require a significantly finer mesh and thus considerably more machine time for the solution. This subcase further serves as a partial checkout of the significance of the isolated surface anisotropic effect.

difference analog. We note in Fig. 11 that the anisotropic surface temperatures calculated with the vanishing mixed difference are not influenced by the reverse interior effect and are therefore higher to the left of the throat and lower to the right than those calculated with the second order difference analog.

Even at the throat plane, both on the surface and in the interior, the results obtained are in agreement with expected effects, i.e., the calculated values exhibit slight trends characteristic of the corresponding values obtained to the right of the throat because of the steeper surface slope to the right of the throat (20 degrees as compared to 10 degrees).

Case c. 90-degree orientation, $K_x = K_\xi = K_{iso} - 0.2 (10^{-5})$, $K_y = K_\eta = K_{iso} + 0.2 (10^{-5})$, $K_{xy} = K'_{xy} = 0$. At the surface, we get

$$K_n = K_{iso} + 0.2(10^{-5}) \left[1 - \left(\frac{\partial f}{\partial x}\right)^2\right] / \left[1 + \left(\frac{\partial f}{\partial x}\right)^2\right] \begin{cases} \geq K_{iso} & \text{if } \left|\frac{\partial f}{\partial x}\right| \leq 1 \\ < K_{iso} & \text{if } \left|\frac{\partial f}{\partial x}\right| > 1 \end{cases}$$

Therefore, we expect $T_{aniso} < T_{iso}$ at all points along the inside surface, including the throat, because $|\partial f/\partial x| < 1$ everywhere on the surface (the maximum inclination from the horizontal being 20 degrees). Indeed, calculated results agree with the expected direction of deviation (Fig. 11).

For the interior temperatures calculated, there is only one case to analyze because $K_{xy} \, \delta^2_{xy} T = 0$ no matter how $\delta^2_{xy} T$ is calculated. Actually two cases were run, one with vanishing $\delta^2_{xy} T$ and the other with the second order calculation given by Eq. 27 through 30, to check the programming of the latter. The results obtained were identical for the two cases, as expected.

45

With the normally directed heat flux at the inside surface applied considerably more in a radial than in an axial direction (the surface being inclined only 20 degrees at most from the horizontal), the radial temperature gradients should be much steeper in the interior than the axial and should also vary more abruptly. Thus, we can expect that

$$\frac{\partial^2 T}{\partial y^2} + \frac{1}{y} \frac{\partial T}{\partial y} > \frac{\partial^2 T}{\partial x^2}$$

Then, because $K_x = K_{iso} - 0.2(10^{-5})$, $K_y = K_{iso} + 0.2(10^{-5})$, $K'_x = K'_y = K'_{iso}$, and $K_{xy} = K'_{xy} = 0$, we would have

$$\rho C \left.\frac{\partial T}{\partial \tau}\right|_{aniso} \cong \rho C \left.\frac{\partial T}{\partial \tau}\right|_{iso} + 0.2(10^{-5}) \left(\frac{\partial^2 T}{\partial y^2} + \frac{1}{y} \frac{\partial T}{\partial y} - \frac{\partial^2 T}{\partial x^2} \right) > \rho C \left.\frac{\partial T}{\partial \tau}\right|_{iso}$$

and we would expect $T_{aniso} > T_{iso}$ at positions which are far enough into the interior to escape domination by the reverse anisotropic effect at the surface. This is reflected in the calculated results (Fig. 11).

Case d. 0-degree orientation, $K_x = K_\eta = K_{iso} + 0.2(10^{-5})$, $K_y = K_\xi = K_{iso} - 0.2(10^{-5})$, $K_{xy} = K'_{xy} = 0$. The reasoning here is just the reverse of that used for Case c. Thus, we get

$$K_n = K_{iso} - 0.2(10^{-5}) \left[1 - \left(\frac{\partial f}{\partial x}\right)^2 \right] / \left[1 + \left(\frac{\partial f}{\partial x}\right)^2 \right] \begin{cases} \leq K_{iso} & \text{if } \left|\frac{\partial f}{\partial x}\right| \leq 1 \\ > K_{iso} & \text{if } \left|\frac{\partial f}{\partial x}\right| > 1 \end{cases}$$

and, therefore we expect $T_{aniso} > T_{iso}$ at the surface, as shown in Fig. 11.

In the interior, we get

$$\rho C \left.\frac{\partial T}{\partial \tau}\right|_{aniso} \approx \rho C \left.\frac{\partial T}{\partial \tau}\right|_{iso} - 0.2(10^{-5}) \left(\frac{\partial^2 T}{\partial y^2} + \frac{1}{y} \frac{\partial T}{\partial y} - \frac{\partial^2 T}{\partial x^2} \right) < \rho C \left.\frac{\partial T}{\partial \tau}\right|_{iso}$$

and we expect $T_{aniso} < T_{iso}$ in the interior, except near the surface where the reverse effect dominates.

Case e. 45-degree orientation, $K_x = K_y = K_{iso}$, $K_{xy} = -0.1K_{iso}$, $K'_{xy} = -0.1K'_{iso}$. Similar reasoning applies at the surface as in Case a. In the interior, however, we must, for the first time, assess the effect of K'_{xy} as well. In particular, by analyzing the subcase for which $\delta^2_{xy} T$ is taken to be identically 0, we isolate the effect of the term $2K'_{xy} \, \partial T/\partial x \, \partial T/\partial y$ in the energy equation as follows:

$$\rho c \left. \frac{\partial T}{\partial \tau} \right|_{aniso} \simeq \rho c \left. \frac{\partial T}{\partial \tau} \right|_{iso} + 2K'_{xy} \frac{\partial T}{\partial x} \frac{\partial T}{\partial y} \, .$$

Therefore, because $\partial T/\partial x$, $\partial T/\partial y$, and K'_{xy} are all negative to the left of the throat $\left(K'_{xy} = -0.1K'_{iso} < 0 \text{ because } K'_{iso} > 0 \text{—see Fig. 10}\right)$, we have

$$\rho c \left. \frac{\partial T}{\partial \tau} \right|_{aniso} < \rho c \left. \frac{\partial T}{\partial \tau} \right|_{iso}$$

and thus $T_{aniso} < T_{iso}$ in the interior to the left of the throat. This is borne out by the calculated results $\left(T_{aniso} = 1517° < 1522° = T_{iso}\right)$. Thus, we see that the presence of the term $2K'_{xy} \, \partial T/\partial x \, \partial T/\partial y$ in the energy equation causes a reversal of the surface effect (in contrast to Case a) and thus constitutes a significant anisotropic effect. To the right of the throat we obtain the consistent result that in the interior T_{aniso} is higher than T_{iso}.

In the second subcase of Case e, in which the second order mixed difference is employed, the direction of deviation from the isotropic results in the interior is the same as in Case a but, as shown in Fig. 11, is more extreme because of reinforcement by the presence of the nonzero term $2K'_{xy} \, \partial T/\partial x \, \partial T/\partial y$ in the energy equation.

TASK 1.C, MORE THAN ONE CHARRING MATERIAL

The major effort required for extending the 2D-ABLATE program to treat
the case of multiple charring ablative thrust chambers was in programming
rather than in modification of the model equations or of the discretiza-
tion procedures. The latter was reflected only in the treatment of the
generated gas mass flux across a material interface; i.e., in the simula-
tion of interface conditions for solution of the continuity equation in
adjacent charring materials. The method adopted was to continue to dis-
cretize the continuity equation at the regular points only (as in the
"old' version of the program in which only one charring material could be
treated) as if no intervening interface existed. However, the thermochemical
properties and charring temperatures associated with each point must be
based on the properties assigned to the material in which the point lies.

The bulk of the programming required for the program extension was thus
of a logical or accounting nature. Additional input allocation and assign-
ment of additionally indexed arrays were required for the constants and
temperature-dependent functions used to describe the gas generation and
curing reactions taking place within several rather than a single charring
material. In Link 1, the selection of the bounding mesh lines for the
solution of the continuity equation was extended from a region lying within
a single material to a multimaterial range. In Links 3 and 4, accounting
changes are required to keep track of the regions and material properties
as the mesh lines cross the interfaces and to interrelate generated gas
mass fluxes from one region to another. Checkout of the added Task 1.C
program capability was performed by comparison with previously computed
results for a carbon cloth-phenolic thrust chamber backed by a stainless
steel shell (the same control case used to check out Tasks 1.A and 1.B).
Two cases were run. In both cases the carbon cloth material was axially
divided into three separate side-by-side charring materials (Fig. 12), each
requiring separate input of the same material properties. In the first case,
all materials were treated as isotropic so that essentially the control
case was rerun to verify that all the charring calculations were being

48
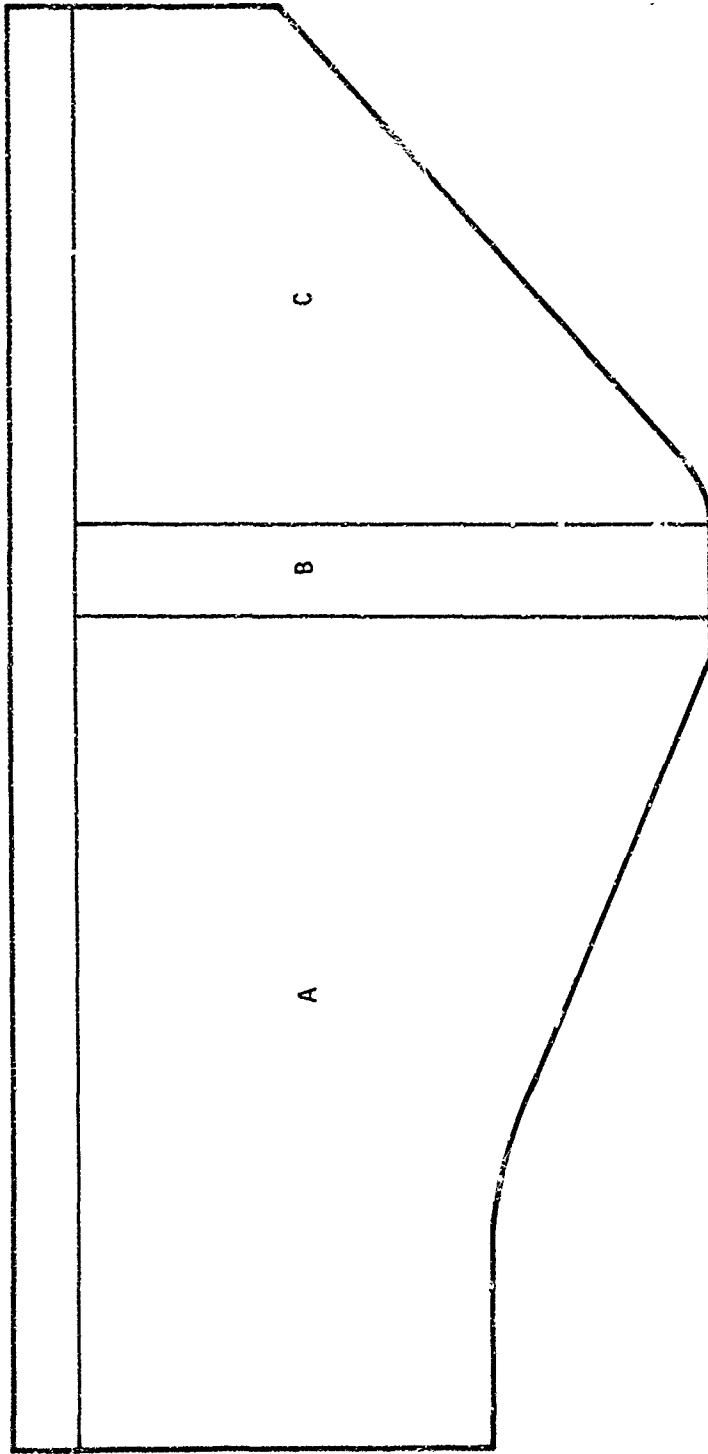
CASE 1: ALL MATERIALS ISOTROPIC

CASE 2:

MATERIAL	ORIENTATION
A	0 DEGREES ≡
B	90 DEGREES ‖‖
C	0 DEGREES ≡

Figure 12. Checkout Cases for Charring in More Than One Material

49

per{ med properl} in each region. The :'ierical results obtained were close but not the same as those obtained in the control case. The discrepancy was caused by truncation error incurred in discretization of the additional interface conditions required to express the continuity of heat flux from material to material: i.e., because of the highly nonlinear character of the variation of heat flux with axial distance occurring at times in the neighborhood of the interfaces. This was particularly true in the early stages of the run when, in the vicinity of an interface, the temperature had risen steeply on one side and not at all on the other side. Despite this difference in results, the checkout was considered to be successful because the charring mechanism worked as intended in the several regions.

In the second checkout case, the configuration and materials were the same as in the first case but all three charring materials were treated as anisotropic, the chamber and exit materials being given a 0-degree orientation ($\theta = 90$ degrees) and the throat material a 90-degree orientation ($\theta = 0$ degrees). As expected, the surface temperatures obtained in the 0 degree materials were higher and the interior temperatures were lower than the corresponding temperatures obtained in the first case, and the reverse was true in the throat material.

TASK 2. EFFECTIVE ABLATION PROPERTIES

INTRODUCTION

The primary objective of Task 2 was to define the effective thermophysical and thermochemical properties of reinforced phenolic resin systems needed for ablative design with the 2D-ABLATE program. The two systems of interest in the program were phenolic-refrasil and phenolic/carbon cloth. Properties for these systems were used for a portion of the 2-D computer runs of Task 3.

Task 2 also fulfilled the following secondary objectives: (1) operational checkout of the 2D-ABLATE computer program, (2) investigation of trial and error techniques for matching experimental data with computed results and (3) analysis of parametric effects in areas which overlapped with Task 3.

The physical properties required in the 2-D program either as functions of temperature (1, 2, 4, 5) or as constants (3, 6, 7) are as follows:

1. Density-specific heat product

2. Fraction of resin pyrolyzed

3. Heat of pyrolysis of the resin

4. Enthalpy of the pyrolysis gases

5. Thermal conductivity of the char and virgin material parallel and perpendicular to the reinforcement

6. Char-reinforcement reaction constants

7. Erosion constants

Insofar as was practical, these properties were obtained from the literature. The values for thermal conductivity and the enthalpy-temperature relationship for the pyrolysis gases were to be obtained by matching the calculated temperature and char profiles of 2D-ABLATE for assumed property values to the

51

experimental temperature profiles and char depths from ablative-walled rocket motor firings.

Appropriate data for the effective property determinations were very limited because of the three basic requirements such data had to meet: (1) relatively constant chamber pressure and mixture ratio, (2) a sufficient number of axial and radial temperature measurements to define the temperature profile as a function of time, and (3) injector performance which gave minimal and circumferentially-uniform surface erosion.

The test data ultimately selected for determination of the properties of phenolic/carbon cloth were generated by the Research Division of Rocketdyne under Contract NAS7-304. The results of four 300-second firings with the propellant combination OF_2/MMH at a nominal chamber pressure of 110 psia were employed. These tests provided data at three reinforcement orientations*, 0, 60, and 94 degrees, together with the thermal response of a nonablative ATJ graphite-walled chamber.

No entirely satisfactory rocket firing data were found to determine the properties of phenolic-refrasil ablatives. Under NASA Contract NAS9-150 (Ref. 7), effective properties of phenolic-refrasil had been estimated by means of the previous verison of 2D-ABLATE (2D-CHAR). However, these estimates were based upon: (1) the assumption of a single charring material and isotropic properties, and (2) upon back wall temperatures which showed highly damped response.

The previous estimates of phenolic-refrasil properties from Ref. 7 were rechecked by calculating the temperature history of the Apollo engine with 2D-ABLATE and comparing the results to the old calculations and to the original experimental data.

In the following sections, the recommended properties for phenolic/carbon cloth and phenolic-refrasil are presented graphically and in a numerical form directly applicable for input to the 2-D program. Applicable properties for the hard throat insert materials, ATJ graphite and silicon carbide,

---

*Orientation is used here and throughout the Task 2 and 3 discussions to mean the counterclockwise rotation θ as defined on p.31 for use in 2D-ABLATE rather than the usual clockwise orientation angle. See footnotes on pp.31 and 41 for the precise relationship between the two.

are also presented. Subsequently, the experimental data and matching procedures employed to define thermal conductivity for the two ablative systems are described.

The analysis of the experimental data used in the phenolic/carbon cloth property determinations is particularly interesting because it clearly shows the artifical nature of the usual boundary conditions assumed in regeneratively cooled rocket chamber heat transfer analyses. It also shows the significance of injector effects on heat transfer.

PROPERTIES

Product of Density and Specific Heat

The recommended values for the $\rho\, C_p$ product of phenolic-refrasil, phenolic/carbon cloth, ATJ graphite and silicon carbide are given in Fig. 13. The corresponding numerical input for 2D-ABLATE usage is presented in Table 2. The method of computation and source data for phenolic refrasil were obtained from Ref. 7. A similar procedure using manufacturer's listed values for virgin density and the same degree of resin pyrolysis was employed for phenolic/carbon cloth. The values for ATJ graphite and silicon carbide were obtained from Ref. 12 and 13.

Fraction Resin Pyrolyzed

The relationship between degree of resin pyrolysis and temperature is given in Fig. 14. It represents the recommended input values for the 2D-ABLATE program for both phenolic refrasil and phenolic/carbon cloth.

In terms of the program input variables

    Maximum fraction resins pyrolyzed = 0.45
    Maximum temperature of pyrolysis range = 1750 R
    Minimum temperature of the pyrolysis range = 750 R
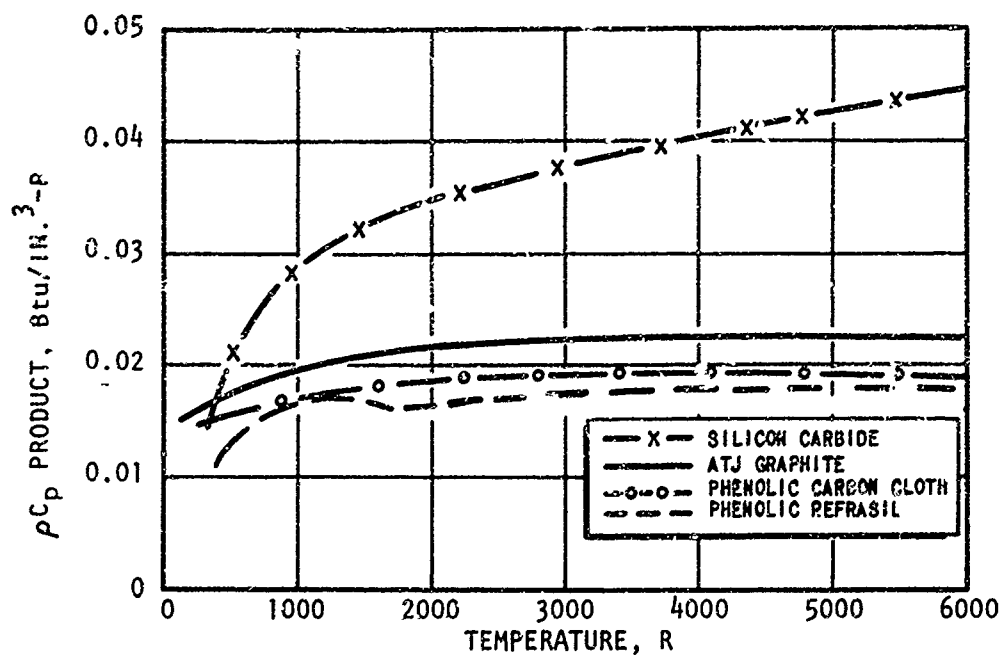
Figure 13. Density – Specific Heat Product For Ablative Chamber Materials
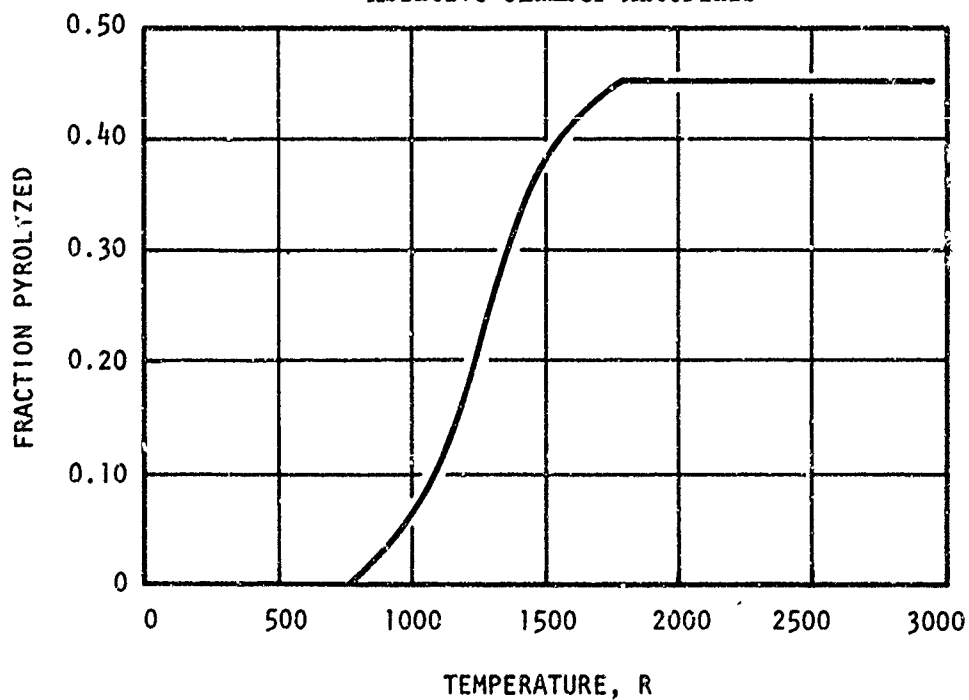
Figure 14. Fraction Resin Pyrolyzed

TABLE 2

RECOMMENDED DENSITY-SPECIFIC HEAT PRODUCT INPUT TO
2D-ABLATE PROGRAM FOR ABLATIVE WALL AND
HARD THROAT MATERIALS

Material	Temperature, R	ρc_p, Btu/in.^{3}-R
Phenolic/Carbon Cloth	350	0.015
	560	0.015
	1060	0.017
	1460	0.018
	2060	0.018
	3460	0.019
	7460	0.019
Phenolic Refrasil	360	0.0093
	660	0.015
	900	0.018
	1460	0.015
	1960	0.016
	3460	0.018
	5460	0.020
ATJ Graphite	370	0.015
	560	0.0175
	1460	0.0195
	2060	0.021
	3460	0.022
	7460	0.022
Silicon Carbide	300	0.012
	600	0.023
	1000	0.029
	3000	0.037
	6000	0.045

The curve of Fig. 14 is based upon the data of Ladacki (Ref. 14) for constant temperature or constant heating rate pyrolysis in a furnace. The data indicate that the fraction pyrolyzed at a given temperature is practically independent of heating rate over the range of heating rates tested.

In initial computer runs conducted with a TAP-IV, 1-dimensional computer program, an upper temperature limit for pyrolysis of 1600 F (2060 R) was assumed. The subsequent reduction to 1750 R appeared to improve the fit of experimental temperature histories to computer calculations.

Heat of Pyrolysis and Pyrolysis-Gas Enthalpy

The heat of pyrolysis for phenolic resins has been shown to vary with temperatures (Ref. 14). However, the 2D-ABLATE input format requires the assumption of a constant value. A standard value for heat of pyrolysis of 450 Btu/lb was employed in all computer runs of Tasks 2 and 3 in this program. Because the heat of pyrolysis represents only a small fraction of the total heat absorbed by the resin and subsequent pyrolysis gas reactions, the choice of the value employed for heat of pyrolysis produces negligible changes in calculated char rates over a range of several hundred Btu/lb.

The 2D-ABLATE program assumes that the degree of pyrolysis and the composition of the pyrolysis gases are thermodynamically rather than kinetically controlled and, that the pyrolysis gases are in local thermal equilibrium with the char. As a result, the enthalpy of the pyrolysis gas from phenolic resin is defined as a function of temperature only. During the Apollo RCS nozzle qualification program (Ref. 7), this functional dependence was deduced by two parallel efforts. Developmental test data for the Apollo RCS engine were matched to computer predictions of outer skin temperatures and char depth for assumed enthalpy-temperature relations. At the same time, Ladacki's experiments (Ref. 14) obtained data on the chemical composition of the pyrolysis vapors. An

enthalpy-temperature curve was obtained from the respective mole fractions, heats of formation, and sensible specific heats of the gaseous species observed in Ladacki's experiments (together with the assumed conversion of these species to carbon monoxide and hydrogen at higher temperature), which substantiated the curve obtained by matching the RCS engine firing data. The enthalpy-temperature curve obtained in the Apollo qualification studies is shown in Fig. 15. Recommended input data to the 2D-ABLATE program are listed in Table 3. The higher-temperature portion of the curve, which is based entirely upon the assumption that the pyrolysis gas is composed of carbon monoxide gas and hydrogen in this temperature range, is uncertain above approximately 3500 R.

TABLE 3

EFFECTIVE ENTHALPY OF PHENOLIC RESIN PYROLYSIS VAPORS

Temperature, R	Enthalpy, Btu/lb
0	0
700	0
1110	750
1560	1850
2060	3850
7460	9250

Thermal Conductivity

The values for thermal conductivity of phenolic-refrasil parallel-to and normal-to the silica reinforcement is shown in Fig. 16. The values shown were determined in the Apollo qualification program (Ref. 15) by a guarded hot-plate method using samples preconditioned at the test temperature. Experimental data were obtained at temperatures up to 1500 F, and the values defined for higher temperatures were estimated theoretically by assuming internal radiant transport contributions (Ref. 7). The thermal conductivity values obtained from the hot plate measurements were employed with a variable pyrolysis gas enthalpy to match the outer wall temperatures of the SE-8 engine during actual firings to the computed results of 2D-CHAR. Thus, the thermal conductivity values for phenolic-refrasil given in Fig. 16 and Table 4 are consistent with the enthalpy-temperature relations of
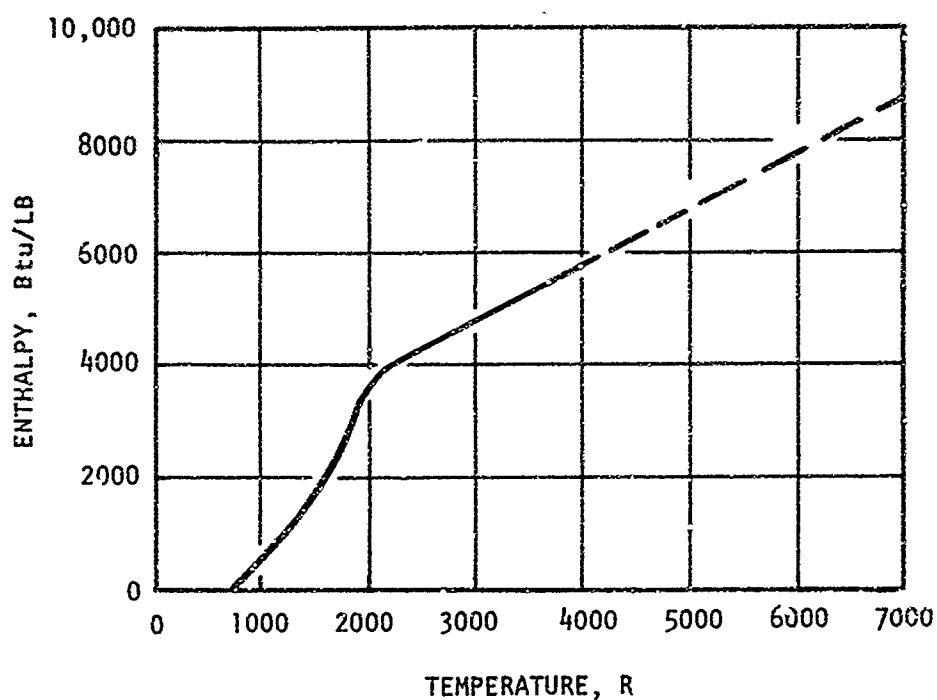
Figure 15. Variation of Pyrolysis-Gas
Enthalpy With Temperature
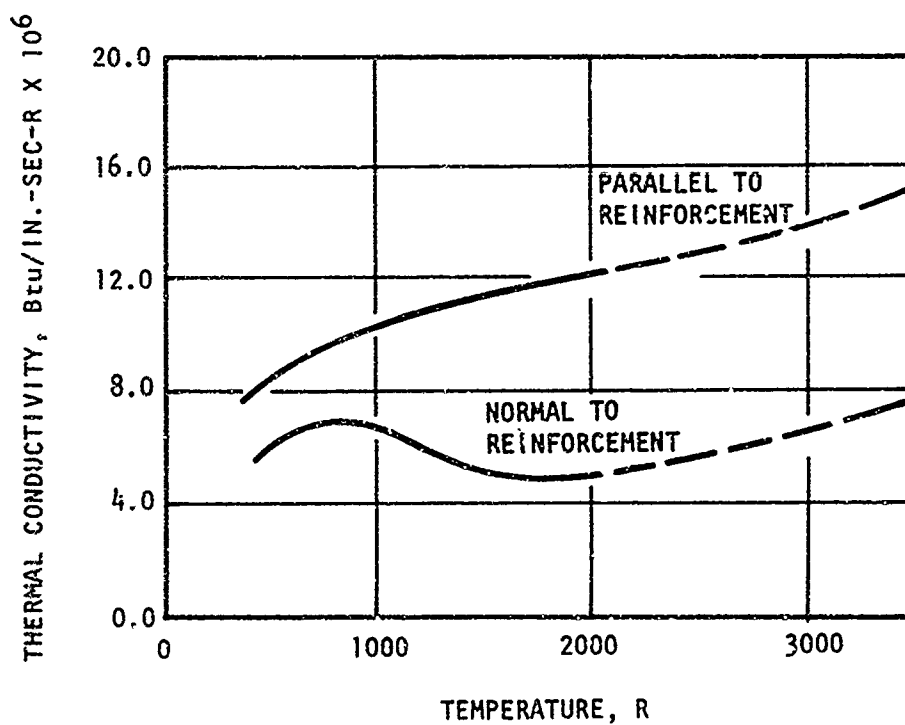
Figure 16. Thermal Conductivity of
Phenolic Refrasil

Fig. 15 and Table 3. The data matching done with 2D-CHAR was checked with 2D-ABLATE as described in a later section of this report.

For phenolic/carbon cloth, the results of the temperature-matching procedures between the OF_2/MMH model motor firing data and the calculations of 2D-ABLATE predict an essentially constant value for thermal conductivity of 8.0×10^{-5} Btu/in.-sec-R parallel to the carbon cloth reinforcement (major direction). A slightly better data fit was obtained by employing a moderate temperature dependency, with the thermal conductivity decreasing from 10×10^{-5} at ambient temperatures to 6×10^{-5} at 1000 F remaining constant for higher temperatures. Because of the relatively low adiabatic wall temperatures in the OF_2/MMH model motor (as discussed in a later section), the same char depth was obtained with either definition of thermal conductivity. However, the former value of thermal conductivity predicts a more conservative char depth for higher adiabatic wall temperatures and therefore is recommended until high adiabatic wall temperature data become available.

The recommended value for thermal conductivity of phenolic/carbon cloth normal to the reinforcement (minor direction) is 7.0×10^{-6} Btu/in.-sec-R between ambient temperatures and 2500 R increasing slowly to 1.5×10^{-5} Btu/in.-sec-R at 7000 R. Because of general similarity between the conductivities of both phenolic-refrasil and phenolic/carbon cloth normal to the reinforcement, a similar temperature dependence is predicted despite the lack of high-temperature experimental data for comparison. The postulated temperature dependence gives conservative predictions (greater char depths) and is therefore recommended. Recommended values for the thermal conductivity of phenolic/carbon cloth are given in Table 4.

Recommended thermal conductivity input data for ATJ graphite and silicon carbide obtained from Ref. 12 are also presented in Table 4.

Char Reinforcement Reaction

Provision is made in 2D-ABLATE for reactions between char and reinforcement. No such reactions need be considered for phenolic/carbon cloth

TABLE 4

RECOMMENDED THERMAL CONDUCTIVITY INPUT FOR 2D-ABLATE

Material	Temperature, R	k (Parallel to Reinforcement), Btu/in.-sec-R	k (Normal to Reinforcement), Btu/in.-sec-R	$\frac{dk}{dT}$ (Parallel to Reinforcement), Btu/in.-sec-R2	$\frac{dk}{dT}$ (Normal to Reinforcement), Btu/in.-sec-R2
Phenolic/Carbon Cloth	100	8.0×10^{-5}	7.0×10^{-6}	0	0
	2500	8.0×10^{-5}	7.0×10^{-6}	0	1.0×10^{-9}
	7000	8.0×10^{-5}	1.5×10^{-5}	---	---
Phenolic Refrasil	360	7.9×10^{-6}	5.9×10^{-6}	7.4×10^{-9}	4.2×10^{-9}
	660	1.01×10^{-5}	7.1×10^{-6}	7.4×10^{-9}	0
	960	1.18×10^{-5}	6.7×10^{-6}	3.9×10^{-8}	-1.1×10^{-9}
	1460	1.39×10^{-5}	5.3×10^{-6}	4.3×10^{-8}	-4.3×10^{-9}
	1960	1.49×10^{-5}	4.9×10^{-6}	2.0×10^{-11}	0
	3460	1.74×10^{-5}	7.7×10^{-6}	3.3×10^{-9}	3.1×10^{-9}
	5460	2.0×10^{-5}	1.4×10^{-5}	---	---
ATJ Graphite	500	1.75×10^{-3}	1.39×10^{-3}	-8.5×10^{-7}	-7.2×10^{-7}
	1000	1.32×10^{-3}	1.03×10^{-3}	-8.5×10^{-7}	-7.2×10^{-7}
	2000	7.8×10^{-4}	5.4×10^{-4}	-2.3×10^{-7}	-2.8×10^{-7}
	2800	6.6×10^{-4}	3.9×10^{-4}	-8.9×10^{-7}	-9.6×10^{-7}
	4000	5.5×10^{-4}	2.8×10^{-4}	-8.4×10^{-7}	-9.3×10^{-7}
	7000	4.8×10^{-4}	1.0×10^{-4}	---	---
Silicon Carbide	400	2.4×10^{-3}	2.4×10^{-3}	-8.5×10^{-7}	-8.5×10^{-7}
	1600	1.4×10^{-4}	1.4×10^{-3}	-9.7×10^{-7}	-9.7×10^{-7}
	3200	2.3×10^{-4}	2.3×10^{-4}	-1.0×10^{-7}	-1.0×10^{-7}
	6000	1.0×10^{-4}	1.0×10^{-4}	---	---

char systems. However, the highly endothermic conversion of silica and carbon to silicon carbide was considered for phenolic-refrasil ablators. In fact, chemical analysis of char specimens from the SE-8 motor walls (Ref. 7) indicated no formation of silicon carbide. Pending experimental verification of appreciable carbide formation, no char-reinforcement reaction inputs are recommended for phenolic-refrasil.

Erosion Rate Constants

The melting point of carbon is above 7000 F. Therefore, the logical modes for surface erosion of either ATJ graphite or carbon-cloth reinforced phenolic char are vaporization and chemical reaction with corrosive combustion gas species. Thermodynamic, chemical equilibrium calculations and experimental data (Ref. 16) indicate that carbon is compatible with HF and CO but is severely attacked by H_2O and CO_2 and, to a lesser extent, by H_2. The recommended erosion input data for either phenolic carbon cloth or ATJ graphite are listed in Table 5. They include vaporization constants from Ref. 17 and chemical reaction rate constants evaluated from data in Ref. 18, 19, and 20 for reactions with H_2O, CO_2, and H_2.

With phenolic-refrasil, melting of the silica reinforcement is the primary erosion mechanism; the secondary mechanism being the char vaporization. Recommended erosion input data for phenolic-refrasil are listed in Table 6.

For silicon carbide, throat erosion occurs primarily by means of decomposition at temperatures above 4500 F. This erosion is treated as a vaporization mechanism with a total vapor pressure equal to the sum of the partial pressures of the decomposition products. Recommended erosion parameters based upon vapor pressure data in Ref. 21 are listed in Table 7. The proposed constants have not been verified by comparison to rocket motor firing data.

TABLE 5

EROSION INPUT DATA FOR CARBON-CLOTH REINFORCED PHENOLIC ABLATORS AND ATJ GRAPHITE

Parameter	Value	Data Input Location
Vaporization Mechanism		
Diffusion Coefficient, $in.^2/sec$	0.04	$896 \div 8n*$
Vapor Molecular Weight	12	$897 \div 8n$
Vapor Pressure Constant, psia	5×10^8	$898 + 8n$
Molar Latent Heat, Btu/lb mole	514000	$899 \div 8n$
Mass Latent Heat, Btu/lb	26000	$900 \div 8n$
Density, $lb/in.^3$	0.081	$901 \div 8n$
Specific Heat of Vapor, $Btu/lb-F$	0.44	$902 \div 8n$
H_2O Reaction Constants		
Molecular Weight of H_2O	18	$936 \div 8n*$
Free Stream Mole Fraction of H_2O	From performance calculation	$937 \div 8n$
Rate Constant, $in./sec$	2.45	$938 + 8n$
Activation Energy, Btu/lb mole	4.21×10^4	$939 + 8n$
Heat of Reaction, Btu/lb	5000	$940 \div 8n$
Mass Diffusion Coefficient, $in.^2/sec$	0.034	$941 + 8n$
Product Specific Heat, $Btu/lb-R$	0.47	$942 + 8n$
H_2 Reaction Constants		
Molecular Weight of H_2	2	$976 \div 8n*$
Free Stream Mole Fraction of H_2	From performance calculation	$977 + 8n$
Rate Constant, $in./sec$	0.095	$978 + 8n$
Activation Energy, Btu/lb mole	6.8×10^4	$979 + 8n$
Heat of Reaction, Btu/lb	4500	$980 + 8n$
Mass Diffusion Coefficient, $in.^2/sec$	0.095	$981 + 8n$
Product Specific Heat, $Btu/lb-R$	1.0	$982 + 8n$
CO_2 Reaction Constants		
Molecular Weight of CO_2	44	$1016 + 8n*$
Free Stream Mole Fraction of CO_2	From performance calculation	$1017 + 8n$
Rate Constant, $in./sec$	0.138	$1018 + 8n$
Activation Energy, Btu/lb mole	33000	$1019 \div 8n$
Heat of Reaction, Btu/lb	4500	$1020 + 8n$
Mass Diffusion Coefficient, $in.^2/sec$	0.0214	$1021 + 8n$
Product Specific Heat, $Btu/lb-R$	0.25	$1022 + 8n$

*Index n goes from 0 to one less than the number of regions

TABLE 6

EROSION INPUT DATA FOR PHENOLIC REFRASIL

ABLATIVE WALLS

Parameter	Value	Data Input Location
Melting Mechanism		
Melt Layer Thermal Conductivity, Btu/in.-sec-R	4.6×10^{-5}	856 + 8n*
Viscosity Constant, lb/in.-sec	2.07×10^{-8}	857 + 8n
Viscosity Activation Energy, Btu/lb mole	2.32×10^{5}	858 + 8n
Melt Specific Heat, Btu/lb-R	0.30	859 + 8n
Melt Density, lb/in.^{3}	0.08	860 + 8n
Heat of Fusion, Btu/lb	100	861 + 8n
Melting Temperature, R	3360	862 + 8n
Vaporization Mechanism		
Diffusion Coefficient, in.^{2}/sec	0.04	896 + 8n*
Vapor Molecular Weight	12	897 + 8n
Vapor Pressure Constant, psia	5×10^{8}	898 + 8n
Molar Latent Heat, Btu/lb mole	314000	899 + 8n
Mass Latent Heat, Btu/lb	26000	900 + 8n
Density, lb/in.^{3}	0.081	901 + 8n
Specific Heat of Vapor	0.44	902 + 8n

TABLE 7

EROSION INPUT DATA FOR SILICON CARBIDE

Parameter	Value	Data Input Location
Vaporization Mechanism		
Diffusion Coefficient, in.^{2}/sec	0.01	896 + 8n*
Vapor Molecular Weight	40	897 + 8n
Vapor Pressure Constant, psia	4.28×10^{9}	898 + 8n
Molar Latent Heat, Btu/lb mole	215,600	899 + 8n
Mass Latent Heat, Btu/lb	4900	900 + 8n
Density, lb/in.^{3}	0.01	901 + 8n
Specific Heat of Vapor	0.2	902 + 8n

*Index n goes from 0 to one less than the number of regions

ESTIMATION OF EFFECTIVE THERMAL CONDUCTIVITY

Phenolic/Carbon Cloth

The effective anisotropic thermal conductivity of carbon-cloth reinforced ablatives was determined by comparing experimental wall temperature profiles measured in model rocket motor firings to the profiles calculated by 2D-ABLATE with assumed values of thermal conductivity. The experimental data used for comparison were generated with the hardware shown in Fig. 17. It consisted of an ablative-walled combustion chamber and an ATJ hard throat section backed-up by porous graphite (Ref. 22).

The experimental conditions for the four tests employed in the data-matching procedure are listed in Table 8. The four tests covered reinforcement orientations of 0, 60, and 84*, together with a test in which the combustion chamber walls consisted of the nonablative ATJ graphite. Consideration of three reinforcement orientations permitted the definition of the directional thermal conductivity of the ablatives while the data from the passive ATJ graphite wall firing established the hot-gas boundary conditions.

TABLE 8

RUN CONDITIONS FOR OF_2/MMH FIRINGS (REF. 22) SELECTED FOR
EVALUATION OF EFFECTIVE PROPERTIES FOR PHENOLIC/CARBON CLOTH

	Test Number			
	1	2	3	4
Nominal Chamber Pressure, psia	110	110	110	110
Nominal Mixture Ratio, o/f	2.0	2.0	2.0	2.0
Mainstage Duration, seconds	300	300	300	300
Throat Insert Material	ATJ	ATJ	ATJ	ATJ
Chamber Insert Material	ATJ	Phenolic/ Carbon Cloth	Phenolic/ Carbon Cloth	Phenolic/ Carbon Cloth
Ablative Material Reinforcement Orientation (relative to radial coordinate), degrees	--	0	60	84

*The orientation is expressed as the angle between the reinforcement and the radial vector consistent with the 2-D ABLATE definitions.

64
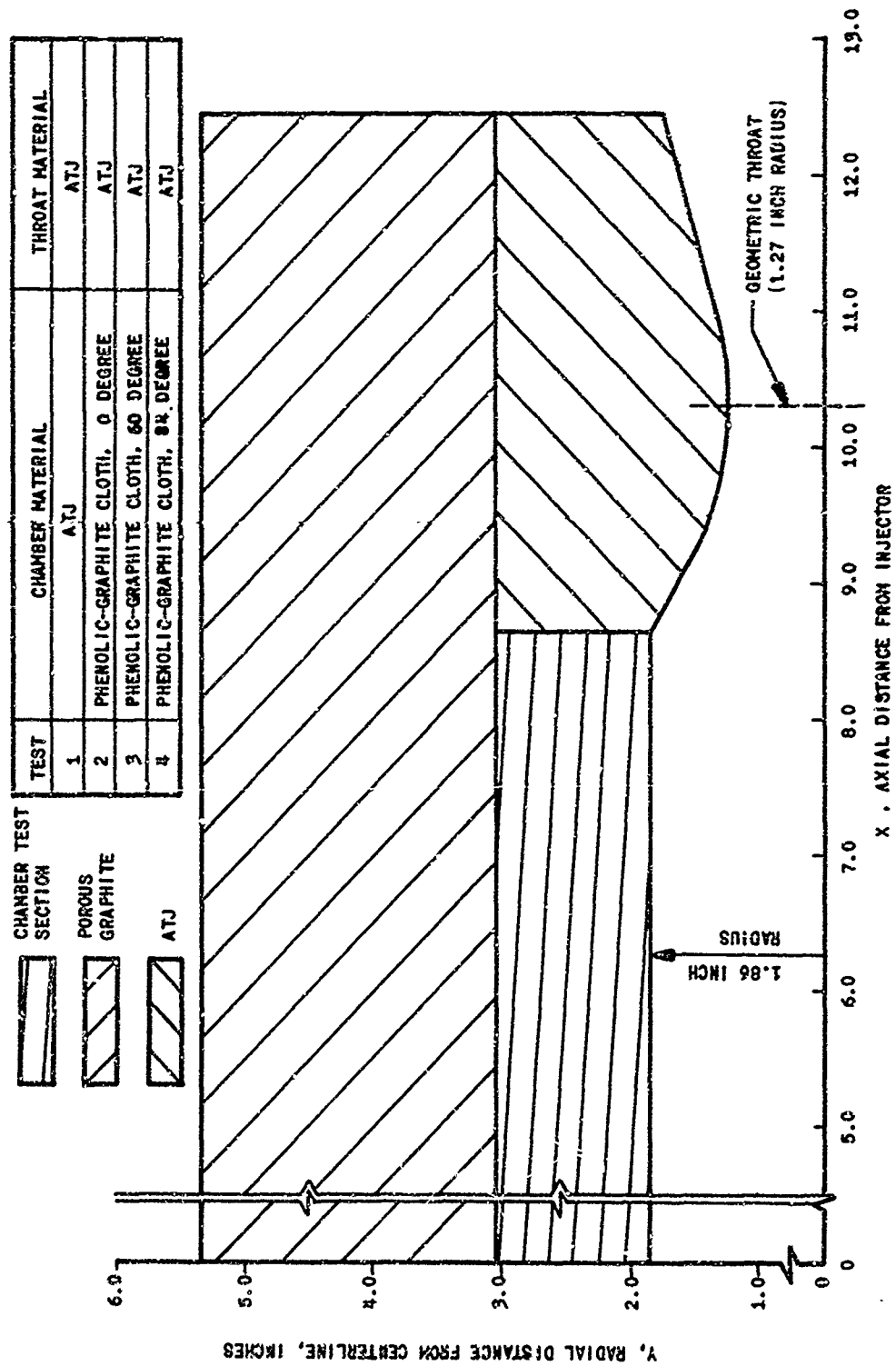
Figure 17. OF₂/Amine Test Motor (Typical), Model Used in 2D-ABLATE

Experimental wall temperature profiles in the combustion chamber walls were obtained from thermocouples embedded at the axial locations and depths (from the hot-gas surface) given in Table 9. The temperature histories recorded during the four motor firings are listed in Table 10.

The overall OF_2/MMH experimental program from which the data of tests 1 through 4 were obtained included a series of very short firings in copper-walled chambers under conditions of chamber pressure, mixture ratio, chamber geometry, and injector configuration very similar to those of tests 1 through 4. With proper instrumentation and reduction of circumferential and axial conduction, the transient wall temperature data from such firings permit a calorimetric measurement of the heat fluxes to the copper walls under conditions of high gas-to-wall temperature difference. From the transient heat flux data, the gas-side heat transfer coefficient is defined by

$$ h_g = \frac{q/A}{T_{aw} - T_W} \tag{2-1} $$

where T_{aw} is the adiabatic wall temperature determined from the thermodynamic gas stagnation temperature by propellant performance calculations at the bulk mixture ratio. The gas-side heat transfer coefficient profile defined by the copper-wall motor firings (Ref. 16) is shown in Fig. 18. The shape of the curve in Fig. 18 agrees with the prediction of the simplified Bartz equation (Ref. 23).

Based upon the data in Fig. 18, the first attempts to match experimental and calculated wall temperature profile employed a heat transfer coefficient calculated by means of the simplified Bartz equation and an adiabatic wall temperature based upon the thermodynamic gas stagnation temperature at a mixture ratio of 2.0. From the Rocketdyne N-element performance program (Ref. 24), T_{aw} was equal to 6200 F.

Initial trial and error calculations to determine effective thermal conductivities were conducted with TAP-4 computer program modified for ablative calculations. The formulation, method of calculation, and specification of physical properties in TAP-4 are essentially the same as those

66
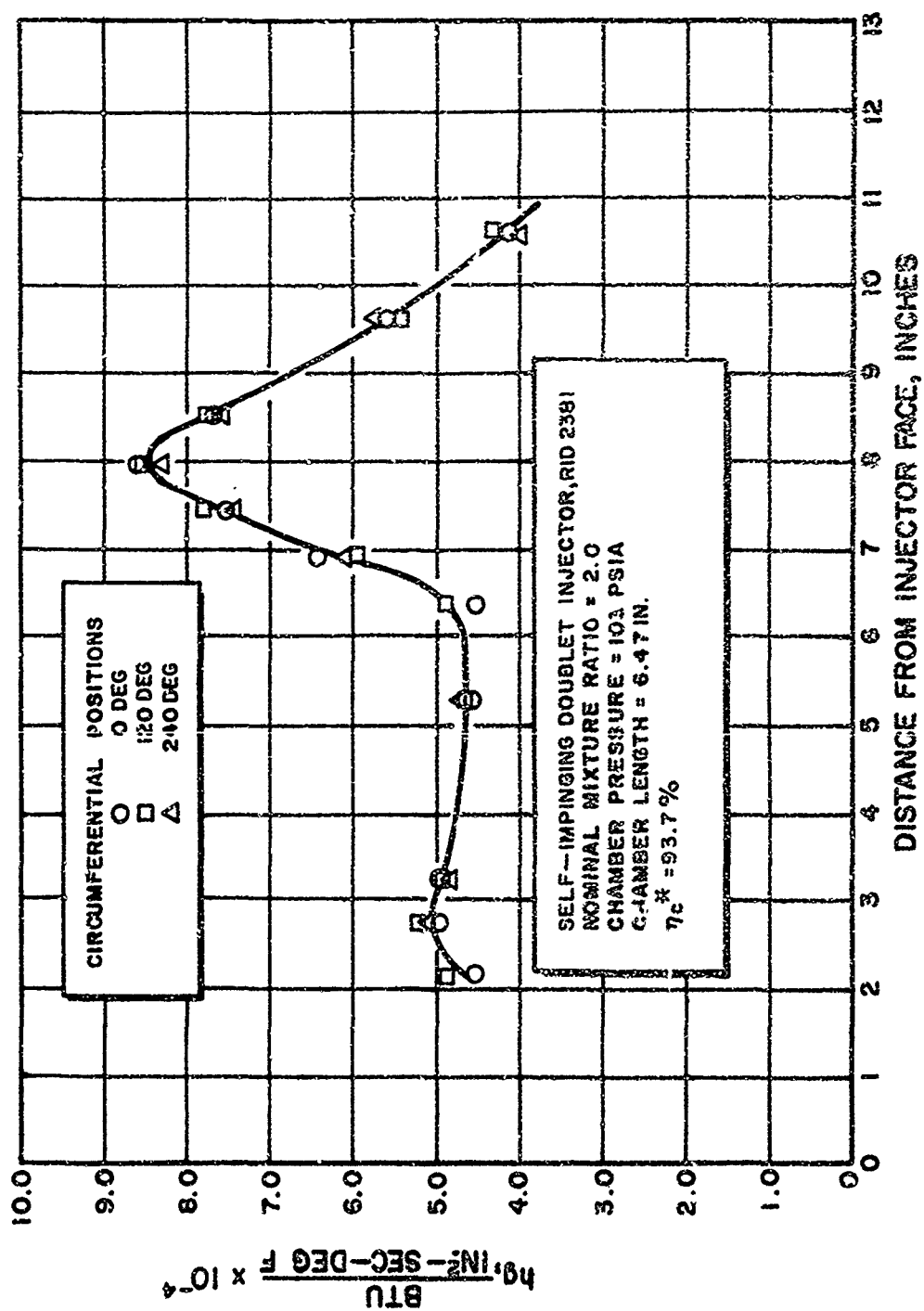
Figure 18. Typical Variation of the Heat Transfer Coefficient With Longitudinal and Circumferential Location for Self-Impinging Doublet Injector Employed in Ablative Motor Firings

67

TABLE 9

LOCATION OF THERMOCOUPLES USED TO MEASURE EXPERIMENTAL
TEMPERATURE HISTORIES USED FOR EVALUATION OF
EFFECTIVE PROPERTIES FOR PHENOLIC/CARBON CLOTH

(Thrust Chamber Locations, OF_2/Amine Tests 1 Through 4)

Thermocouple Number	Test Number							
	1		2		3		4	
	Axial and Radial Coordinates, inches							
	X	Y	X	Y	X	Y	X	Y
1	5.23	2.11	2.87	2.61	2.87	2.61	2.87	2.61
2	5.48	2.94	2.87	2.16	2.87	2.16	2.87	2.15
3	7.73	2.11	2.87	2.93	2.87	2.93	2.87	2.93
4	7.98	2.94	2.87	2.36	2.87	2.36	2.87	2.36
5	5.23	2.11	5.74	2.61	5.74	2.61	5.74	2.61
6	5.48	2.94	5.74	2.16	5.74	2.16	5.74	2.16
7	7.73	2.11	5.74	2.93	5.74	2.93	5.74	2.93
8	7.98	2.94	5.74	2.36	5.74	2.36	5.74	2.36
9	10.32	2.94	9.48	2.46	–	–	8.97	1.90
10	11.32	2.94	9.48	1.71	–	–	8.97	2.93
11	–	–	9.48	2.93	–	–	9.48	2.32
12	–	–	10.32	2.32	–	–	9.48	1.72
13	–	–	10.32	1.57	–	–	9.48	2.93
14	–	–	10.32	2.93	–	–	10.32	2.32
15	–	–	11.38	2.36	–	–	10.32	1.57
16	–	–	11.38	1.76	–	–	10.32	2.93
17	–	–	11.38	2.93	–	–	–	–

TABLE 10

THERMOCOUPLE DATA, OF$_2$/AMDE

I. Test 1

Time, seconds	Thermocouple Number — Temperature, F									
	1	2	3	4	5	6	7	8	9	10
4.0	81	82	87	87	83	85	83	87	92	92
10.0	680	265	710	360	605	265	670	240	?70	175
20.0	1110	620	1175	680	1055	605	1110	590	425	400
30.0	1395	890	1540	990	1375	870	1490	860	625	585
40.0	1610	1135	1825	1250	1620	1090	1770	1040	790	730
50.0	1800	1330	2060	1440	1815	1260	2050	1185	930	870
60.0	1935	1470	2230	1585	1970	1410	2210	1310	1060	1010
70.0	2040	1580	2355	1695	2085	1535	2355	1430	1170	1110
80.0	2110	1640	2450	1805	2170	1640	2440	1535	1270	1205
90.0	2160	1690	2515	1900	2235	1730	2515	1635	1360	1285
100.0	2195	1735	2570	1990	2285	1805	2575	1730	1430	1360
120.0	2250	1830	2635	2040	2375	1930	2650	1890	1545	1475
140.0	2300	1920	2670	2250	2450	2030	2715	2015	1620	1580
150.0	2340	1985	2710	2335	2500	2105	2565	2120	1680	1670
180.0	2370	2040	2745	2400	2540	2170	2800	2210	1750	1750
200.0	2395	2090	2780	2460	2580	2220	2835	2280	1810	1820
220.0	2410	2120	2805	2505	2605	2260	2860	2340	1870	1890
240.0	2425	2155	2835	2550	2620	2295	2880	2390	1925	1945
260.0	2440	2175	2860	2585	2635	2325	2900	2435	1980	1995
280.0	2445	2200	2660	2620	2640	2350	2920	2480	2030	2045
293.5	2445	2220	2650	2650	2645	2370	2925	2500	2070	2075

II. Test 2

Time, seconds	1	2	3	4
7.5	85	75	90	80
10.0	85	75	90	80
20.0	80	100	90	80
30.0	80	140	90	90
40.0	80	215	90	100
50.0	85	295	95	125
60.0	95	405	95	155
70.0	110	505	100	195
80.0	130	595	115	240
90.0	155	665	135	290
100.0	195	720	160	340
120.0	290	845	210	435
140.0	360	930	350	565
160.0	410	1025	420	660
180.0	455	1120	445	740
200.0	490	1260	440	820
220.0	530	1400	500	890
240.0	575	1480	540	960
260.0	615	1525	580	1040
280.0	650	1580	625	1145
300.0	685	1625	680	1270

III. Test 3

Time, seconds	Thermocouple Number — Temperature, F									
	1	2	3	4	5	6	7	8	9	10
40.0	95	155	95	110	90	220	90	110		
50.0	100	215	105	150	95	330	95	1 3		
60.0	115	280	115	180	100	425	100	180		
70.0	130	345	130	235	110	510	100	230		
80.0	155	410	155	285	130	610	105	285		
90.0	180	470	175	330	145	780	115	350		
100.0	215	535	200	380	170	915	120	415		
120.0	300	665	275	475	225	1155	140	460		
140.0	375	790	345	570	290	1350	175	710		
160.0	440	920	395	705	355	1495	210	875		
180.0	500	1030	435	810	410	1620	255	1040		
200.0	560	1120	465	900	480	1715	290	1185		
220.0	615	1205	490	980	560	1785	335	1315		
240.0	665	1280	510	1050	640	1840	390	1420		
260.0	720	1345	525	1120	730	1875	455	1500		
280.0	765	1405	540	1190	820	1905	550	1575		
293.0	800	1435	550	1230	885	1920	585	1615		

IV. Test 4

Time seconds	1	2	3	4
40.0		25		
50.0		40	20	
60.0		65	25	20
70.0	10	95	30	25
80.0	15	135	35	50
90.0	20	185	40	70
100.0	30	235	45	85
120.0	45	320	45	115
140.0	70	340	55	170
160.0	100	365	65	210
180.0	125	445	85	250
200.0	150	585	100	285
220.0	175	705	115	320
240.0	195	815	130	380
260.0	215	905	145	460
280.0	230	975	160	550
295.0				

TABLE 10

COUPLE DATA, O$_2$/AMINE TESTS

Test 2

	Thermocouple Number																
1	2	3	4	5	6	7	8	9	10	11	12	13	14	15	16	17
								Temperature, F								
85	75	90	80	85	80	90	80	260	620	145	225	525	105	200	395	95
85	75	90	80	85	80	90	80	390	795	200	310	615	135	280	490	100
80	100	90	80	80	85	90	80	715	1175	450	590	945	305	510	755	145
80	140	90	90	80	105	90	95	875	1435	790	820	1160	490	720	915	215
80	215	90	100	80	160	90	125	1170	1685	880	980	1340	650	870	1070	310
85	295	95	125	85	215	90	165	1335	1835	1010	1150	1490	770	1005	1200	405
95	405	95	155	95	295	95	225	1470	1960	1110	1275	1625	880	1120	1315	490
110	505	100	195	105	410	100	290	1595	2080	1165	1395	1755	950	1225	1425	585
130	595	115	240	115	520	100	360	1700	2180	1205	1495	1860	1000	1315	1525	670
155	665	135	290	130	615	110	435	1295	2275	1250	1595	1955	1050	1405	1610	750
195	720	160	340	150	710	130	500	1880	2360	1310	1680	2045	1110	1490	1700	830
290	845	210	455	190	865	160	620	2045	2485	1415	1835	2210	1240	1640	1855	985
360	930	350	565	250	1015	205	735	2180	2575	1520	1980	2340	1365	1775	1985	1110
410	1025	420	660	310	1180	255	840	2300	2640	1620	2110	2460	1475	1895	2090	1225
455	1120	445	740	390	1365	310	965	2410	2690	1700	2215	2555	1575	2005	2160	1330
490	1260	440	820	465	1410	380	1105	2495	2735	1780	2310	2635	1660	2090	2230	1425
530	1400	500	890	555	1460	450	1260	2570	2780	1855	2390	2690	1755	2175	2280	1510
575	1480	540	960	635	1510	540	1420	2640	2815	1920	2460	2705	1855	2250	2325	1590
615	1525	580	1040	690	1555	610	1560	2695	2855	1995	2525	2695	1910	2320	2360	1690
650	1580	625	1145	740	1600	675	1640	2750	2890	2055	2590	2745	1975	2575	2395	1750
685	1625	680	1270	785	1725	755	1665	2800	2920	2105	2650	2765	2040	2410	2410	1820

Test 4

	Thermocouple Number																
1	2	3	4	5	6	7	8	9	10	11	12	13	14	15	16	17
								Temperature, F								
	25				60			1410	865	1005	1450	865	870	1290	760	
	40	20			95		10	1605	1025	1200	1670	1050	1070	1505	940	
	65	25	20		130		15	1770	1155	1365	1850	1200	1230	1675	1095	
10	95	30	25		165		35	1910	1280	1505	1995	1330	1365	1825	1220	
15	135	35	50	10	210		55	2020	1385	1630	2125	1445	1490	1950	1340	
20	185	40	70	15	270		75	2125	1485	1740	2235	1550	1595	2065	1440	
30	235	45	85	20	350		95	2215	1580	1850	2330	1645	1695	2165	1530	
45	320	45	115	25	460	20	135	2365	1740	2010	2505	1810	1875	2345	1690	
70	340	55	170	60	580	35	175	2495	1865	2160	2645	1960	2030	2490	1835	
100	365	65	210	85	750	55	220	2610	1995	2290	2750	2090	2165	2595	1965	
125	445	85	250	110	960	75	275	2710	2100	2420	2845	2195	2290	2695	2050	
150	585	100	285	125	1110	95	335	2790	2200	2520	2905	2285	2390	2785	2180	
175	705	115	320	155	1250	120	405	2855	2285	2600	2970	2365	2485	2860	2270	
195	815	130	380	175	1320	125	490	2910	2355	2665	3020	2440	2555	2935	2350	
215	905	145	450	215	1360	130	590	2960	2420	2725	3070	2500	2625	3015	2425	
230	975	160	550	230	1370	135	710	2995	2480	2775	3115	2560	2700	3090	2490	
								3025	2525	2805	3145	2610	2745	3145	2540	

employed in 2D-ABLATE, except that it is one-dimensional and thus isotropic in all parameters. The thermocouple data obtained in the combustion chamber were expected to be amenable to one-dimensional analysis because the axial variation in temperature is dominated by radial temperature gradients in this region.

Successive computer runs over a wide range of radial thermal conductivities did not produce a match with the experimental temperature profiles for any reinforcement orientation. Moreover, when the assumed radial thermal conductivities at any two reinforcement orientations which would produce a match between computer-calculated and experimental char depths at these orientations were combined to calculate the major and minor axis thermal conductivities according to

$$k_y = k_\eta \cos^2 \theta + k_\xi \sin^2 \theta \tag{2-2}$$

the resultant definition of radial conductivity for the third orientation did not produce a match between computer calculation and experiment.

Several computer runs were conducted with 2D-ABLATE to match the temperatures in Test 1 with the ATJ graphite chamber (Tables 8 and 10) The calculated surface temperatures in the throat region were close to the adiabatic wall temperature (6200 F) rather than the values of 3000 to 3500 F measured with the optical pyrometer.

Because of the discrepancies between calculated and measured temperatures, the gas-side boundary conditions were reviewed with particular attention given to possible injector effects on thrust chamber heat transfer. The injector employed in the test hardware was particularly designed for a low mixture ratio near the chamber walls so as to reduce the concentration of water vapor below the corrosive limit for carbon walls. Sampling of the injector spray pattern under cold flow conditions had demonstrated that the mixture ratio near the wall was reduced to less than 1.0 (Ref. 16). At this mixture ratio, the thermodynamic gas temperature is 5000 F. Unpublished gaseous mixing experiments at Rocketdyne have shown that parallel gas streams have not approached equilibrium after as much as 22 equivalent

70

stream diameters. Therefore, it is reasonable to expect that the combustion gas in rocket chambers has a local temperature defined by the mixture ratio distribution at the injector.

For the injector employed in the ablative motor firings, the adiabatic wall temperature was therefore hypothesized to be much less than the thermodynamic temperature for the bulk mixture ratio as assumed for regenerative cooling. The increase in measured wall temperatures from the injector to the throat for the data of Test 1 also indicated that the adiabatic wall temperature was a function of axial distance.

Realistic values for the adiabatic wall temperature and the gas-side heat transfer coefficient in the test hardware were derived by an iterative procedure. An adiabatic wall temperature distribution was first assumed. A distribution of heat transfer coefficients was calculated so as to result in the experimental heat flux profile to copper chamber walls at 200 F. These adiabatic wall temperature and film coefficient distributions were then employed with 2D-ABLATE to calculate the wall temperature profile of Test 1. If a match was not obtained with experimental values, a new set of values for adiabatic wall temperatures was postulated and a new iteration was conducted. The procedure was continued until calculated and experimental wall temperatures converged. The final distributions of adiabatic wall temperature and heat transfer coefficient are given in Fig. 19. The gas-side boundary conditions shown in Fig. 19 produced the wall temperature histories shown as dotted curves in Fig. 20. The corresponding experimental temperature histories are superimposed thereon as solid curves showing reasonably good agreement between computed values and experimental results.

On the basis of the revised gas-side boundary conditions, new sets of ablative wall temperature profiles were derived with the TAP-4 computer program for assumed values of thermal conductivity. Because of the relatively low adiabatic wall temperatures involved, the range of calculated wall temperatures was relatively narrow for carbon cloth ablatives. Therefore, it was considered impractical to define a temperature dependency for the thermal conductivities derived. Examples of the match between experimental and calculated temperature profiles are given in Fig. 21.
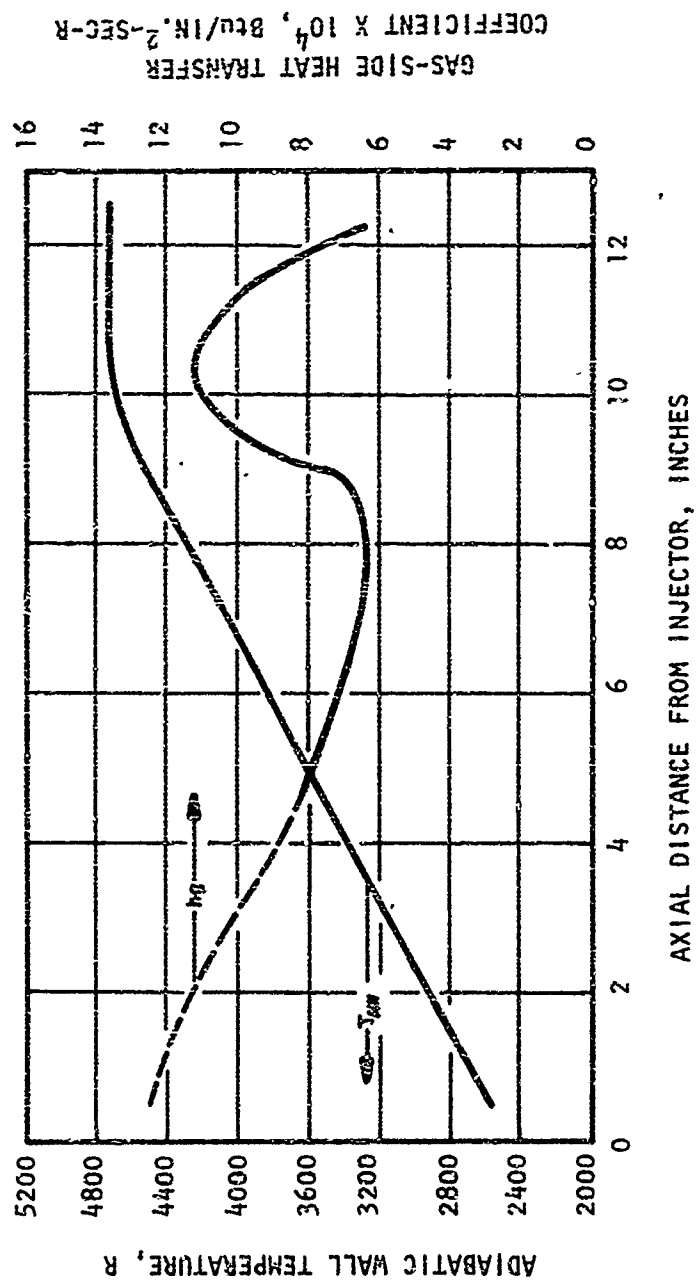
71

Figure 19. Axial Distribution of the Adiabatic Wall Temperature and the Gas-Side Heat Transfer Coefficient as Derived From an ATJ-Graphite Reference Test Case
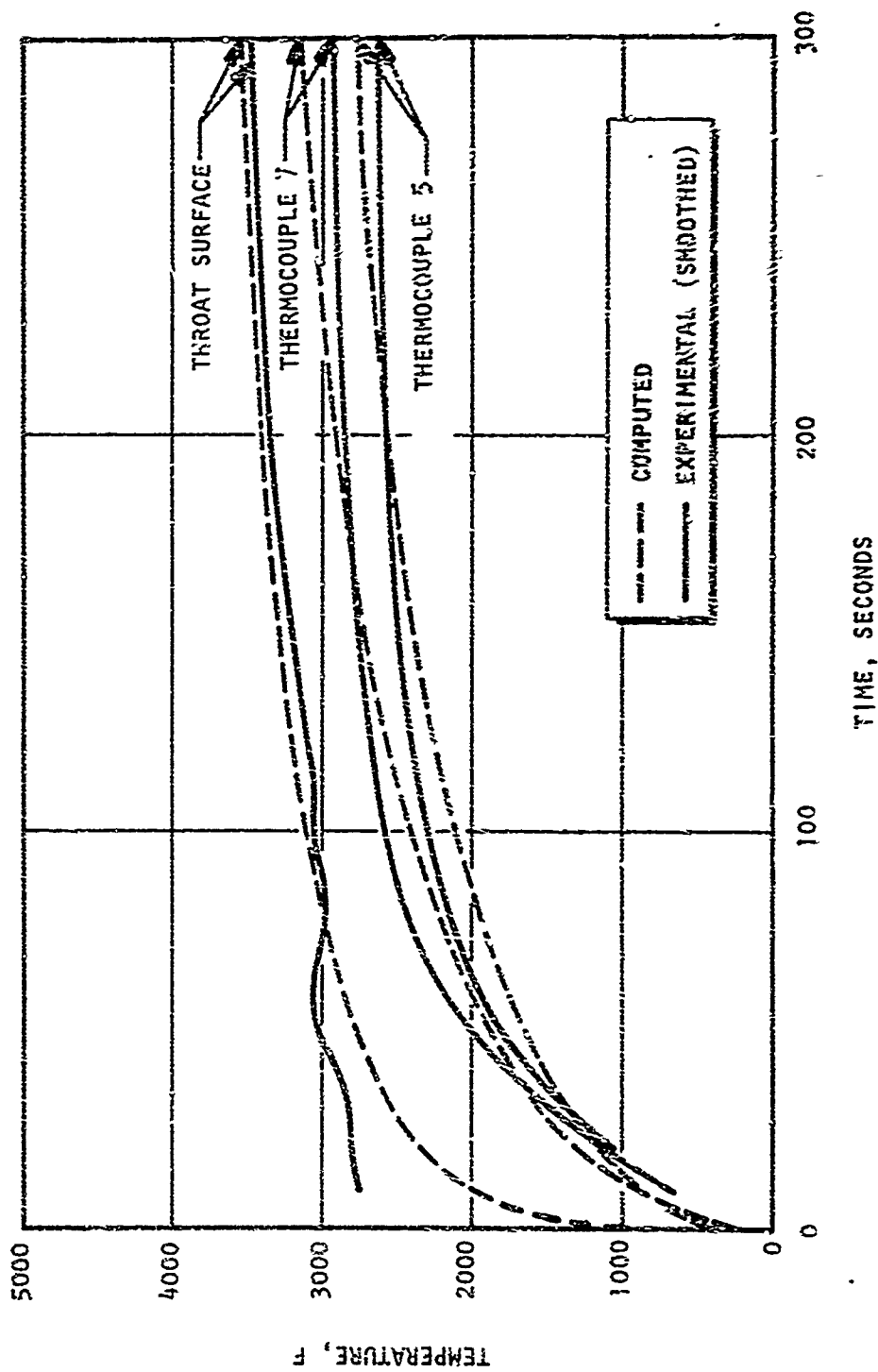
Figure 20. Computed and Experimental Temperature Histories For an ATJ-Graphite Case (Test 1)
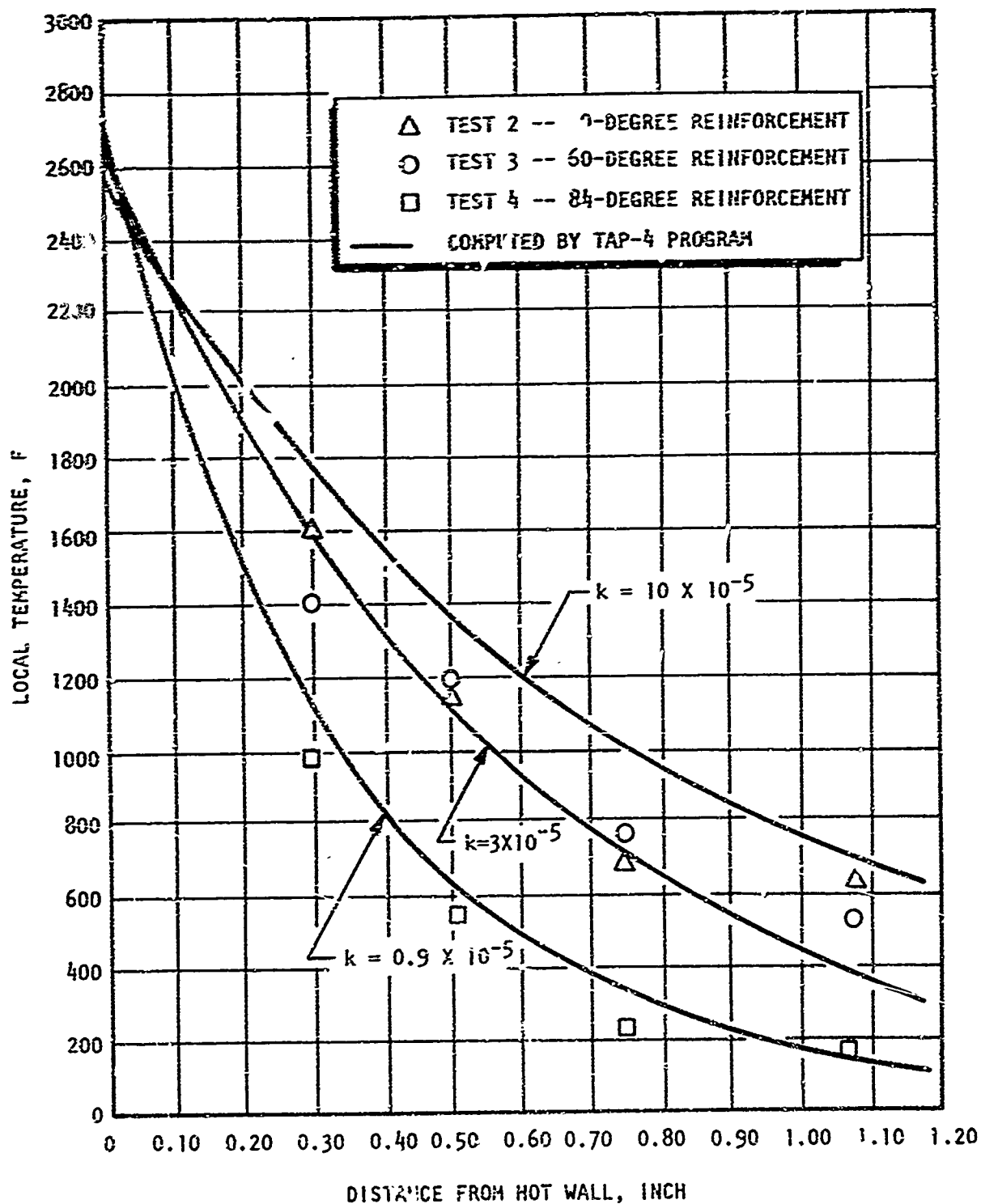
Figure 21. Temperature Profiles in Carbon Phenolic Ablators
at 280 Seconds for an Adiabatic Wall Temperature
of 2800 F and a Heat Transfer Coefficient of
0.0008 Btu/in²-sec-F

74

The curves represent computed results by the TAP-4 program for various
values of thermal conductivity. Further refinement of the computed results
was subsequently accomplished with the 2D-ABLATE program. It is because of
the relatively low wall temperatures (both calculated and experimental)
shown in Fig. 21, that no verification of the high temperature thermal con-
ductivity of the ablative walls could be made. Rocket motor firings giving
verified adiabatic wall temperatures of at least 5000 F under well-
instrumented conditions are required to obtain such high temperature
information.

The comparison between calculated and experimental profiles for the three
reinforcement orientations was combined with that between the experimental
and calculated char depths* and weighted with the requirement that the
radial thermal conductivities for these orientations be related by Eq. 2-2.
Based on all considerations, a constant value of 8.0×10^{-5} Btu/in-sec-F
is recommended for the major direction thermal conductivity together with
a minor direction thermal conductivity which ranges from 7.0×10^{-6} to
1.5×10^{-5} Btu/in.-sec-F as given in Table 4.

Phenolic Refrasil

The approach used to estimate the effective thermal conductivity of
phenolic-refrasil differed markedly from that employed for phenolic-
carbon cloth. Because the effective thermophysical and thermochemical
properties of this system had been estimated under another contract with
the 2D-CHAR (isotropic) computer program (Ref. 7), their validity had to
be checked with the (anisotropic) 2D-ABLATE computer program.

The experimental data used for comparison were those obtained on certain
qualification tests of the Apollo Command Module rocket engine and nozzle
extension. The computer model of this test configuration is shown in
Fig. 22. The specific data employed were the backwall temperature

---

*Experimental char depths were based upon photographs of sectioned chamber
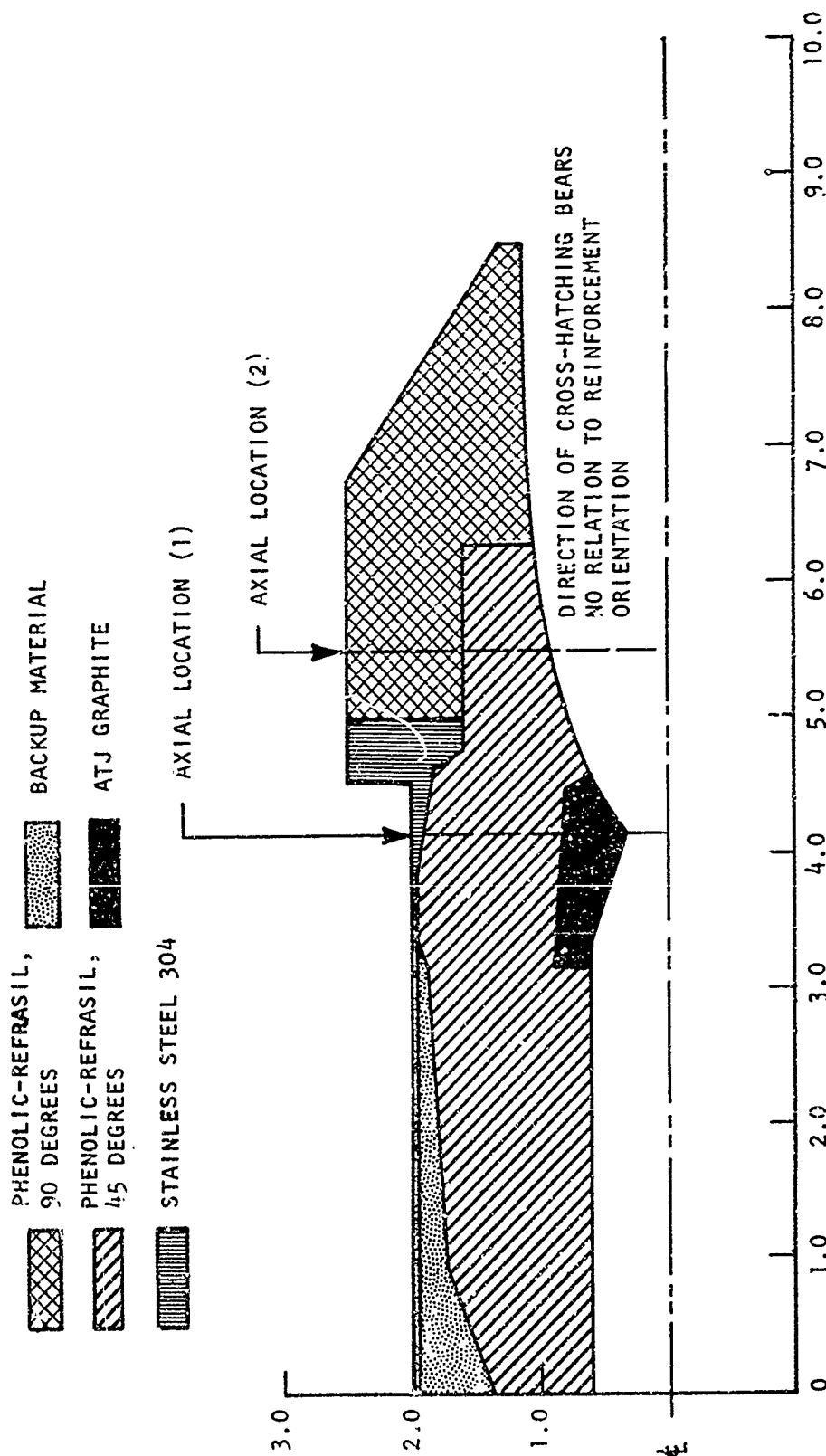 walls. Calculated char depths are based upon the 1000 F isotherm.

75

Figure 22. Apollo Qualification Test Model For 2D. ABLATE

histories during a given mission duty cycle at two external points. The axial locations (Fig. 22) correspond to (1) the nozzle throat, and (2) a point 1 inch downstream of the upstream face of the motor mounting flange.

Because of the limitations of 2D-CHAR (mentioned above), the original effective properties were estimated without consideration of anisotropicity. Additionally, the reinforcement orientation in the chamber/extension (45 degrees relative to the chamber centerline) differed from that in the nozzle (parallel to the nozzle centerline). Two separate calculations were made to produce a match between the experimental and predicted backwall temperature histories. The first, in which the reinforcement orientation in the entire motor was assumed to be 45 degrees and the second, in which it was assumed to be 0 degrees. With these assumed orientations, the effective thermophysical and thermochemical properties were estimated by separately matching the throat station and nozzle station data (Ref. 7). This approach with the 2D-CHAR was required because that program was limited to isotropic properties and could accommodate one charring material only. The property variation resulting from a different orientation of an anisotropic material is in effect a second charring material.

After resolving the anisotropic properties estimated with 2D-CHAR into the major and minor directions, the properties as previously estimated were submitted on 2D-ABLATE. The results are shown in Fig. 23 and 24. The experimental Apollo data as well as the backwall temperature history predicted by 2D-CHAR are superimposed. The differences are nominal; e.g., nowhere exceeding about 20 F at the throat station. The effective thermophysical and thermochemical properties thus estimated were presented in Table 4. Again it should be remembered that temperature measurements in the range shown in Fig. 24 and 25 are not a verification of ablative thermal conductivities at high (>2500 F) temperatures.
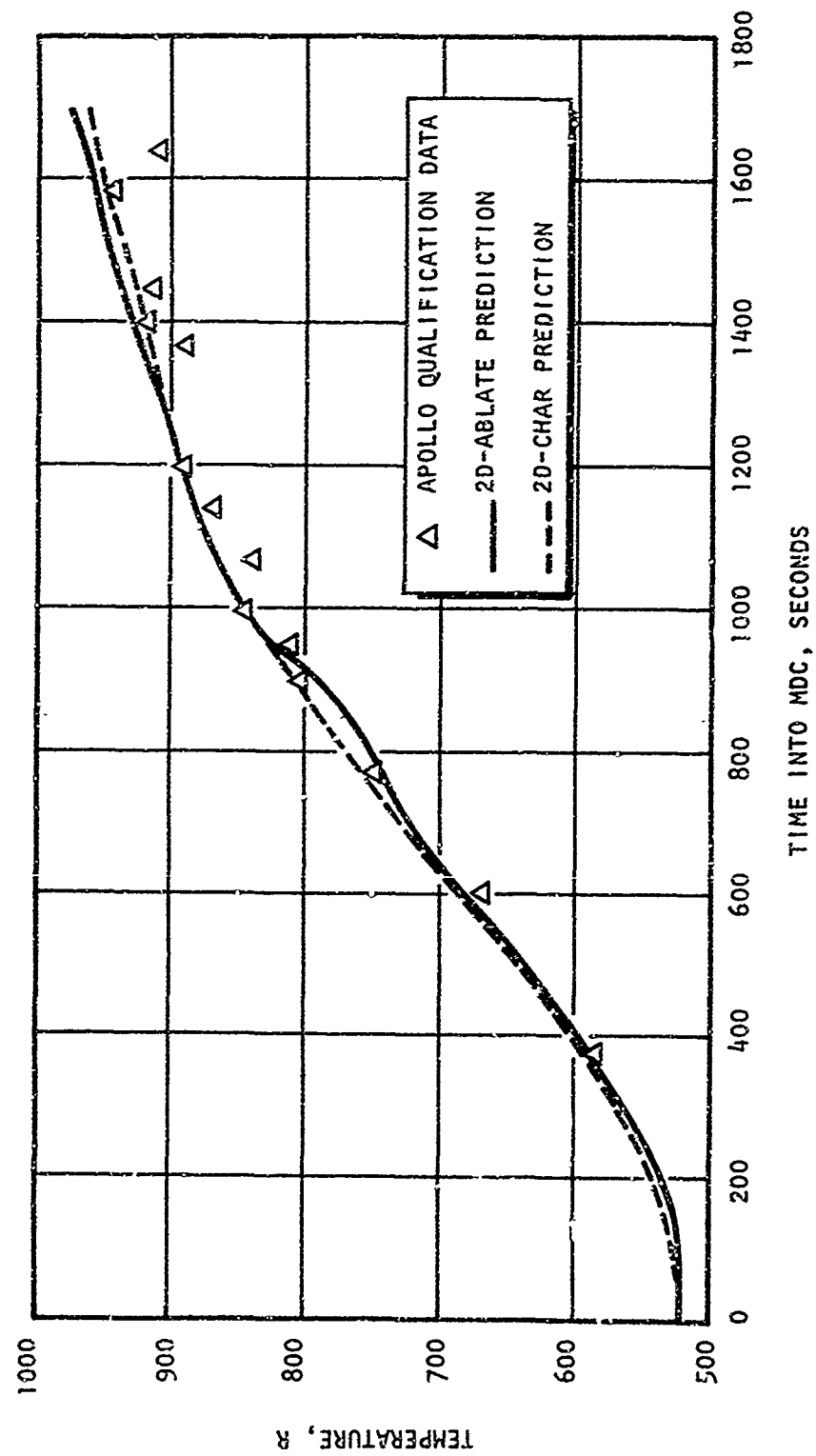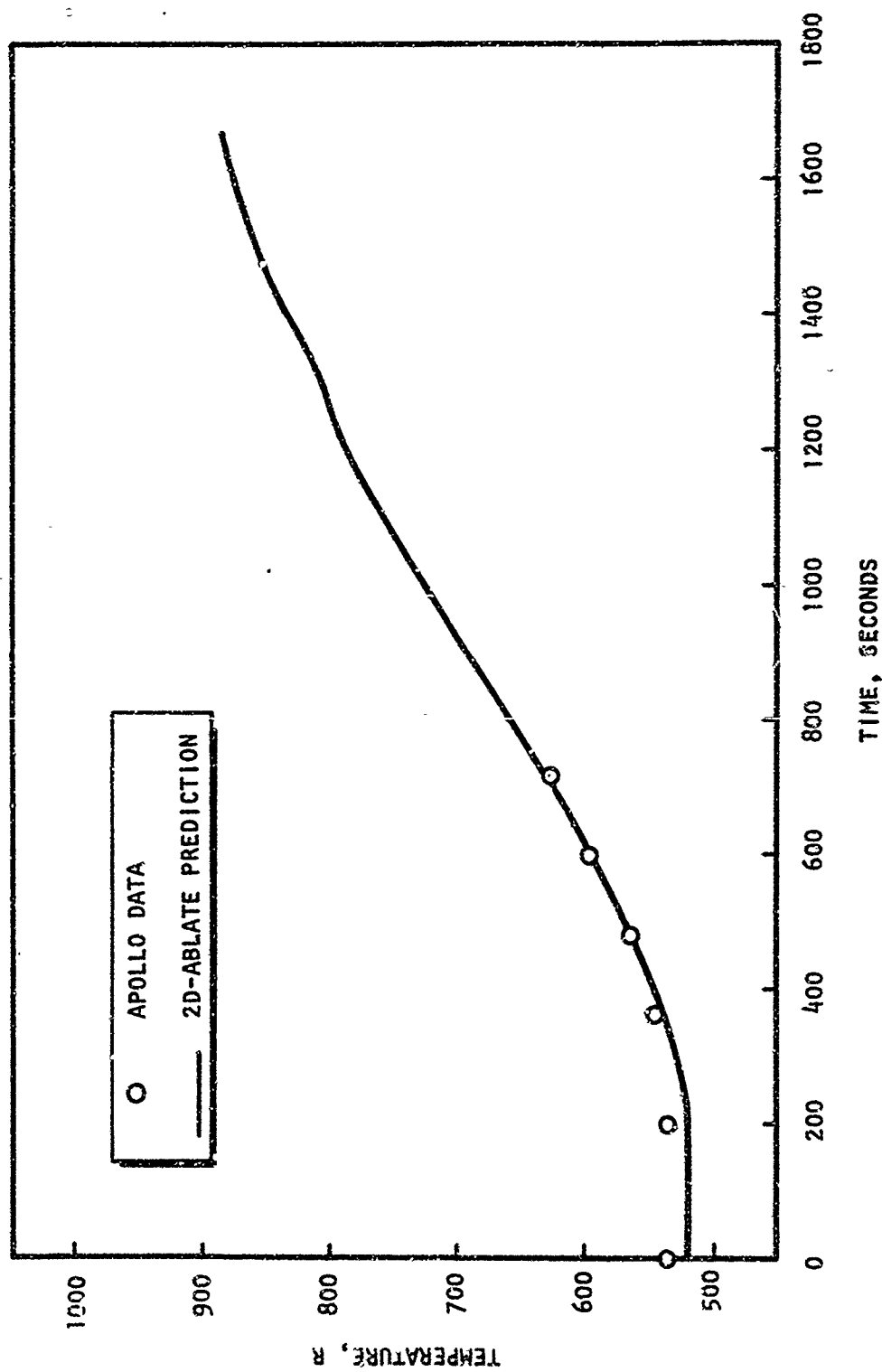
Figure 23 . Throat-Station Backwall Temperature

The figure shows a plot of Temperature, R (y-axis, ranging from 500 to 1000) versus Time into MDC, seconds (x-axis, ranging from 0 to 1800). The legend indicates:

△ APOLLO QUALIFICATION DATA
—— 2D-ABLATE PREDICTION
— — 2D-CHAR PREDICTION

78

Figure 24. Nozzle-Station Backwall Temperature

TASK 3, DESIGNER'S GUIDE

The two-dimensional computer program is ideally suited for the calculation of char rate, erosion, and temperature distribution within curved boundaries and multimaterial configurations typical of real thrust chamber walls if all the system parameters required for program input are known. However, the use of the computer program to optimize an ablative wall configuration within the constraints of an overall engine design requires an iterative procedure in which the parameters not completely fixed by mission requirements are systematically varied. Because of the large number of possible parameters to be considered, a systematic ablative design requires that the approximate effects of the most important parameters be known in advance; otherwise the number of iterations becomes excessive.

Subsequent sections of this report provide the designer with information relating the useful life of ablative chamber walls to the more important operating variables and material properties. Discussion is restricted to the following thermal responses: (1) char rate, (2) thermal penetration, and (3) surface erosion and surface temperature. Other factors in mechanical design which are related to thermal history such as material strength and thermal stress are not considered. Discussion is also restricted to the phenolic resin systems and to the common reinforcements, refrasil and carbon cloth.

SIGNIFICANT PARAMETERS

The variables known to be important to ablative chamber design can be divided into three categories:

1. Combustion gas properties and operating conditions

2. Chamber geometry

3. Wall material properties

81

The propellant combination and mixture ratio define the gas temperature and such properties as specific heat, molecular weight, and viscosity which in turn define the heat transfer coefficient and the concentration of corrosive gaseous species (H_2O, CO_2, and H_2). The adiabatic wall temperature and the effective gas properties are specified by the mixture ratio near the wall. The chamber operating conditions which affect ablative chamber design are duty cycle, chamber pressure, and thrust level. Duty cycle specifies not only the total firing duration but also the available cooldown periods between successive firings. To the extent that sensible heat stored in a char layer or refractory throat insert can be lost by radiation between firing periods, the length of the pulses and the interposed cooldown periods can reduce char depth and surface erosion.

Chamber pressure determines the heat transfer coefficient and the concentration of corrosive species in the combustion gases. With other conditions fixed, the magnitude of the heat transfer coefficient determines how closely the surface temperature approaches the adiabatic wall temperature. Over wide ranges of heat transfer coefficient, variations in ΔT between the surface and adiabatic wall temperatures produce relatively small percentage changes in the ΔT between surface and charring reaction zone and therefore relatively minor differences in char rate. However, because of the Arrhenius type of temperature dependence for surface reactions, the differences in surface temperature produced by changes in heat transfer coefficient can produce significant differences in surface erosion. Thrust level combined with chamber pressure and contraction ratio determines the throat and chamber dimensions and thereby the two-dimensional nature of the axisymmetric system.

The obvious variables of chamber geometry are the expansion and contraction ratios, the contraction and expansion 1/2-angles and the arrangement of hard or soft throat inserts with multilayer ablative walls of different reinforcements and reinforcement orientations. The effects of these variables are two-dimensional in nature and many of the boundary conditions are difficult to specify for a real system.

It is particularly difficult to specify the heat transfer coefficient for high contraction ratios and high contraction 1/2-angles, and the resultant erosion rates are correspondingly uncertain. The expansion ratio determines the radiative view factor between the throat region and free space and partially defines the maximum temperature of nonablative throat inserts.

The most important wall material parameters are thermal conductivity, resin content, chemical reactions between char, pyrolysis gases and reinforcement, and surface erosion resistance. The thermal conductivity of the char controls the diffusion of heat from the combustion gases to the charring reaction zone. High thermal conductivity produces a high charring rate but also produces a lower surface temperature and therefore a lower surface erosion. The thermal conductivity of the virgin ablative determines the thermal penetration through the virgin ablative. Resin content determines the rate of char front advance as do the energy absorbing processes occurring in the char layer between the char and the percolating pyrolysis gases. Although the reaction between refrasil (silica) reinforcement and char has been proposed as a high heat sink, Rocketdyne experience on the Apollo program indicates that this reaction does not occur.

The resistance to erosion of ablative or passive refractory materials is dependent upon a high melting point, low vapor pressure, and compatability with boundary layer gas species. The optimal combination of low erosion, low char rate, and low thermal penetration will usually require a multi-layer combination of ablative and passive materials.

Although the heat transfer in an ablative system is, in fact, two dimensional, the radial temperature gradients through most chamber walls are much larger than the axial gradients. For convenience in preliminary design, axial conduction can be ignored and a "first cut" design can be based on radial heat transfer only. Similarly, it is most convenient to evaluate the effects of the various physical, chemical, and transport properties of the wall material and combustion gas on a one-dimensional

95

basis. In the following section of this report, the thermal responses of ablative walls to a one-dimensional radial heat flux are presented graphically and analyzed for the following parameters:

Wall thermal conductivity

Adiabatic wall temperature

Resin fraction

Heat transfer coefficient

Chamber radius

ONE-DIMENSIONAL RELATIONSHIPS

Definitions

Experiments (Ref. 11) have shown that charring of phenolic resins occurs at a rapid but finite rate over the approximate temperature range 300 F to 1600 F. Therefore, a narrow zone of partially charred resin rather than a distinct char-virgin interface exists in ablative walls both during and after burn time. However, because of the thermodynamic description of the char reaction in the computer program it is convenient to define a char front for purposes of comparing various parametric effects. In the following sections of the report, char rate is defined as the rate of advance of the 1000 F isotherm. Similarly, char depth is the distance from the hot-gas surface to the 1000 F isotherm.

Transfer of heat from ablative walls to outer portions of the vehicle is directly related to the temperature profile in the virgin material. This can be loosely expressed as thermal penetration through the wall. In the following sections, thermal penetration is defined as the location of the 100 F isotherm with respect to the surface for a system initially at 70 F.

Surface erosion is the increase (assumed circumferentially uniform) in the diameter of the chamber at a given location.

Surface temperature is the temperature of the ablative wall exposed to the combustion gas. This response is directly related to surface erosion and in some cases is used in place of erosion for evaluating parametric effects.

Thermal Conductivity

The effect of ablative wall thermal conductivity on char depth is shown in Fig. 25 through 27 for adiabatic wall temperatures of 3500, 5000, and 7000 F respectively. All curves are based upon a chamber radius of 1.90 inch and a wall thickness of 1.20 inch. The 3500 F curves are based upon a heat transfer coefficient of 0.00065 Btu/in^2-sec-F and a resin content of 0.30; the 5000 and 7000 curves are based upon a heat transfer coefficient of 0.0005 Btu/in^2-sec-F and a resin content of 0.25; All three graphs show that char rate is a strong function of thermal conductivity. If a modified Biot modulus is defined as:

$$Bi = \frac{h_g \, \Delta y_c}{k_c} \tag{3-1}$$

where Δy_c is the char depth, a simple expression can be written for the effect of thermal conductivity on char rate which applies for Biot moduli greater than about 10. This simple expression which can be employed to interpolate between curves is

$$\frac{(\Delta y_c)_2}{(\Delta y_c)_1} = \sqrt{\frac{k_2}{k_1}} \tag{3-2}$$

The curves of Fig. 25 through 27 are for heat transfer coefficients in the range of 0.0005 to 0.00065 Btu/hr-ft^2-F typical for a combustion chamber at chamber pressures from 70 to 150 psia. The relationship between char depth and thermal conductivity for very high and very low values of heat transfer coefficient is given in Fig. 28. For high values of film coefficient, Eq. 3-1 and 3-2 still apply for interpolation. However, char depth is relatively independent of thermal conductivity at very low values of film coefficient (Fig. 28).
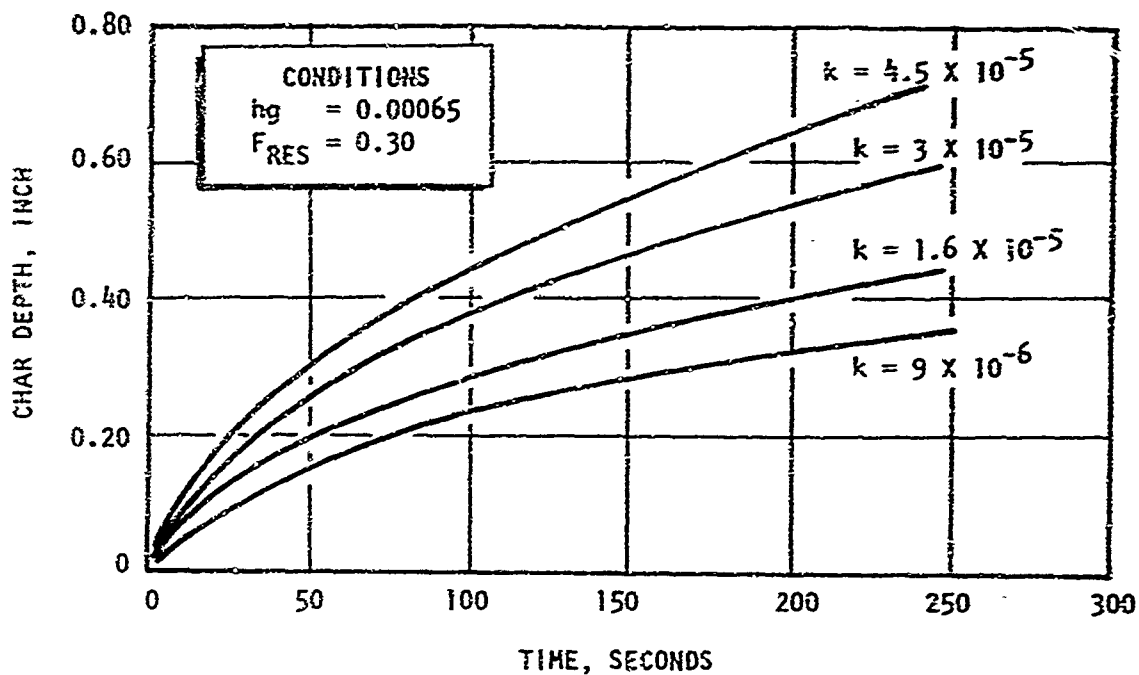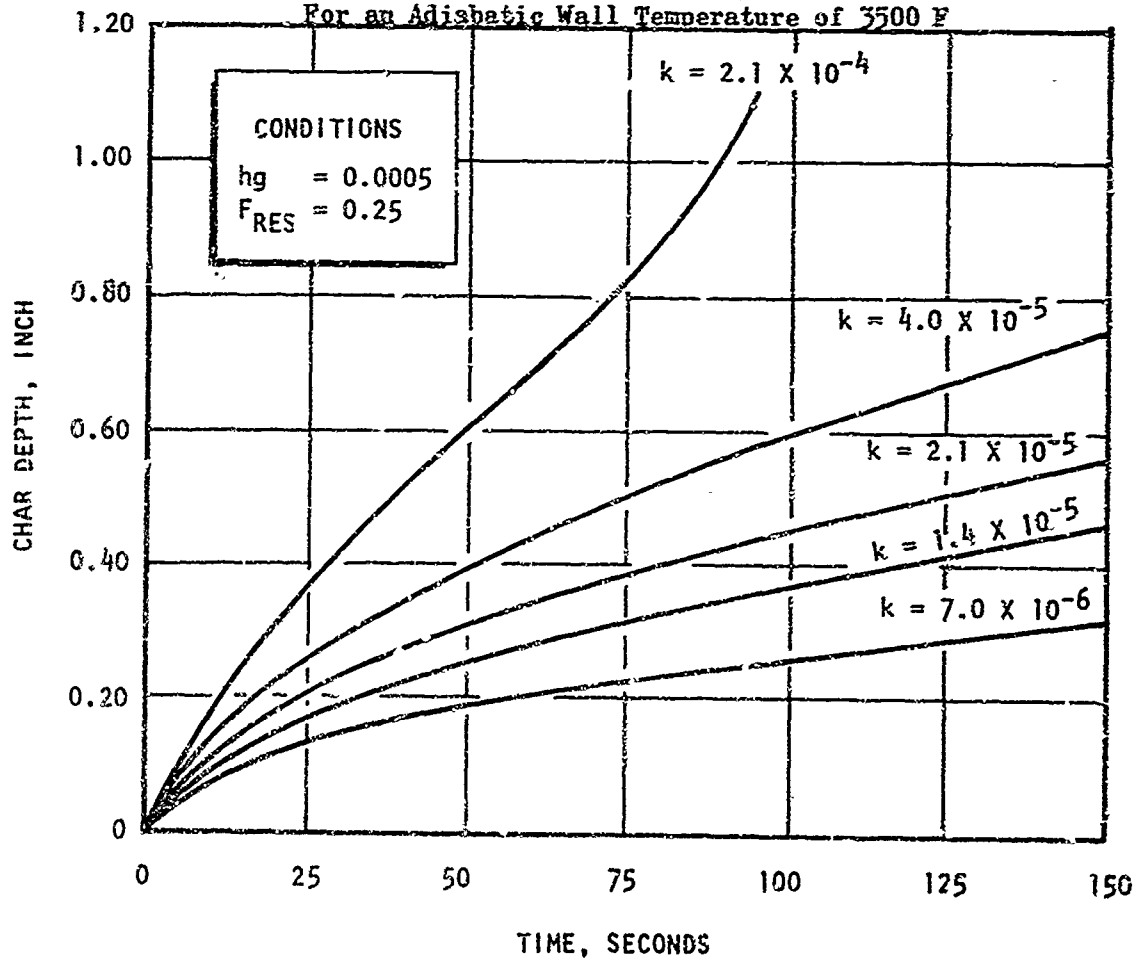
85

Figure 25. Effect of Thermal Conductivity on Char Front Advance For an Adiabatic Wall Temperature of 3500 F

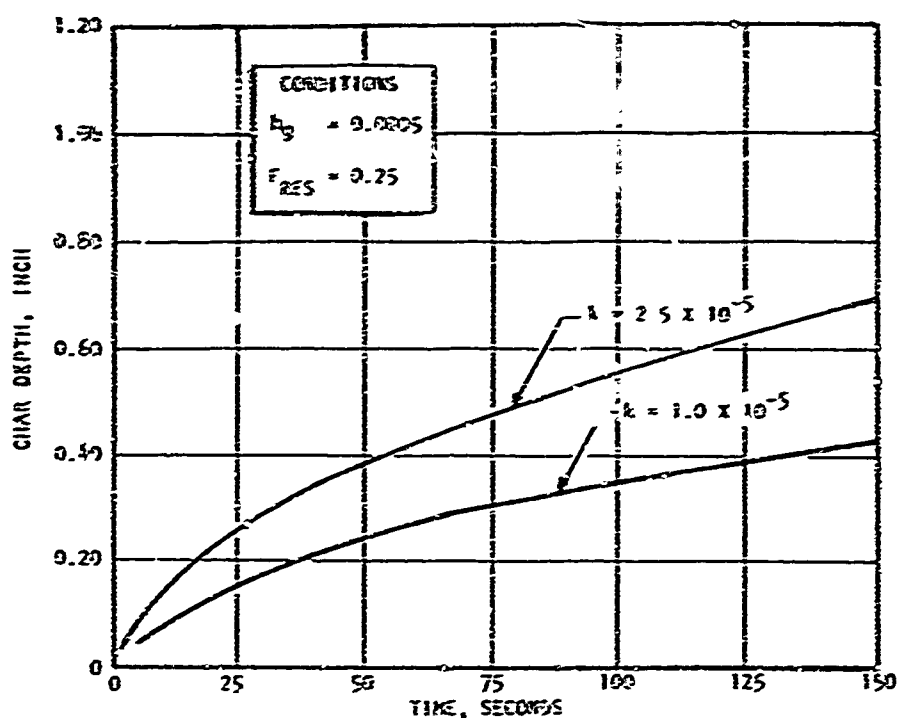Figure 26. Effect of Thermal Conductivity on Char Front Advance For an Adiabatic Wall Temperature of 5000 F

86

Figure 27. Effect of Thermal Conductivity on Char Front Advance for an Adiabatic Wall Temperature of 7000 F
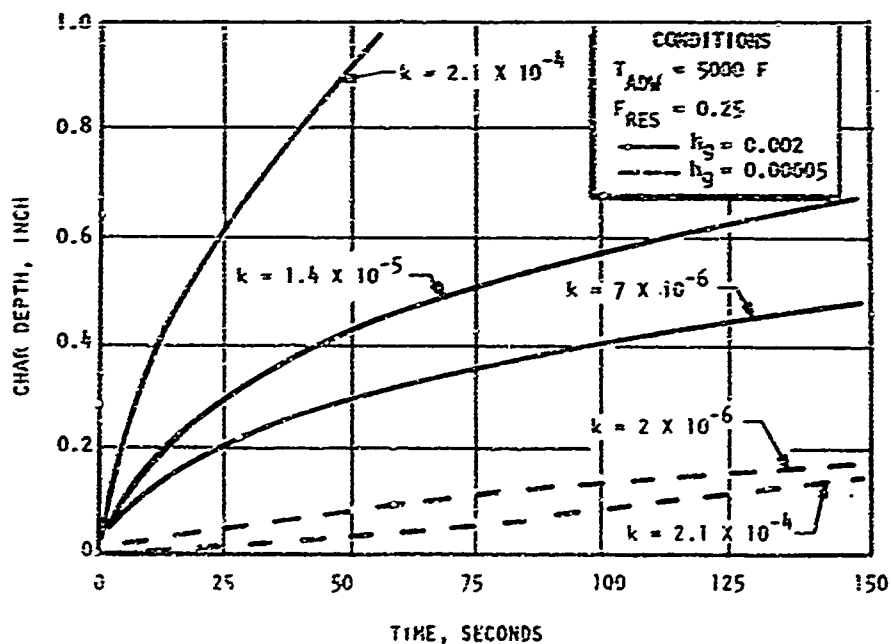

Figure 28. Effect of Thermal Conductivity at High and Very Low Values of Heat Transfer Coefficient

87

The effect of thermal conductivity on thermal penetration is shown in
Fig. 29. As would be expected, thermal penetration depends upon the
conductivity of both the char and the virgin materials. The results shown
in Fig. 29 can be extended to other adiabatic wall temperatures and other
char- and virgin-region thermal conductivities by means of the relation:

$$\frac{(\Delta y_p - \Delta y_c)_2}{(\Delta y_p - \Delta y_c)_1} = \sqrt{\frac{k_{v_2}}{k_{v_1}}} \qquad (3\text{-}3)$$

In Eq. 3-3, Δy_p is the thermal penetration depth (the 100 F isotherm)
while Δy_c is the char depth and k_v is the thermal conductivity of the
virgin material. The char depth can be obtained from Fig. 25 through 27
while a reference Δy_p is obtained from Fig. 29.

The effect of thermal conductivity upon the gas-side surface temperature
is shown in Fig. 30 for an adiabatic wall temperature of 5000 F and a
heat transfer coefficient of 0.0005 Btu/in^2-sec-F. The effect of increasing
thermal conductivity is to reduce the rate at which the surface temperature
approaches the adiabatic wall temperature or, in other words, to lower the
surface temperature at any time. Interpolation between the curves of
Fig. 30 and extrapolation to other adiabatic wall temperatures can be
made with fair accuracy by the relationship:

$$\frac{\left[(T_{aw} - T_s)/(T_{aw} - 1200)\right]_2}{\left[(T_{aw} - T_s)/(T_{aw} - 1200)\right]_1} = \sqrt{\frac{k_2}{k_1}} \qquad (3\text{-}4)$$

where the effective temperature of the heat sink is taken to be 1200 F.
Eq. 3-4 may be used when the modified Biot number defined by Eq. 3-1 is
greater than 10.

In general, all three responses, char rate, thermal penetration, and
surface temperature are related to the square root of the thermal conduc-
tivity. These thermal conductivity effects with ablation are therefore
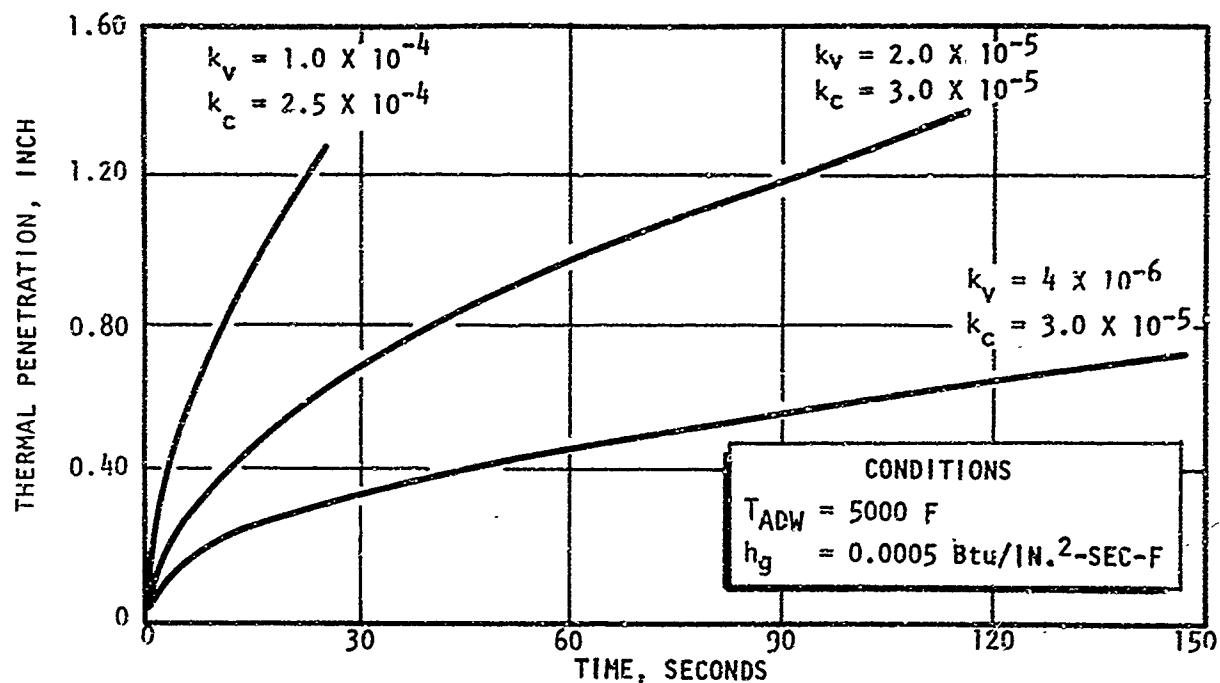very similar to the relationships for ordinary transient conduction. In

88

Figure 29. Effect of Thermal Conductivity on Thermal
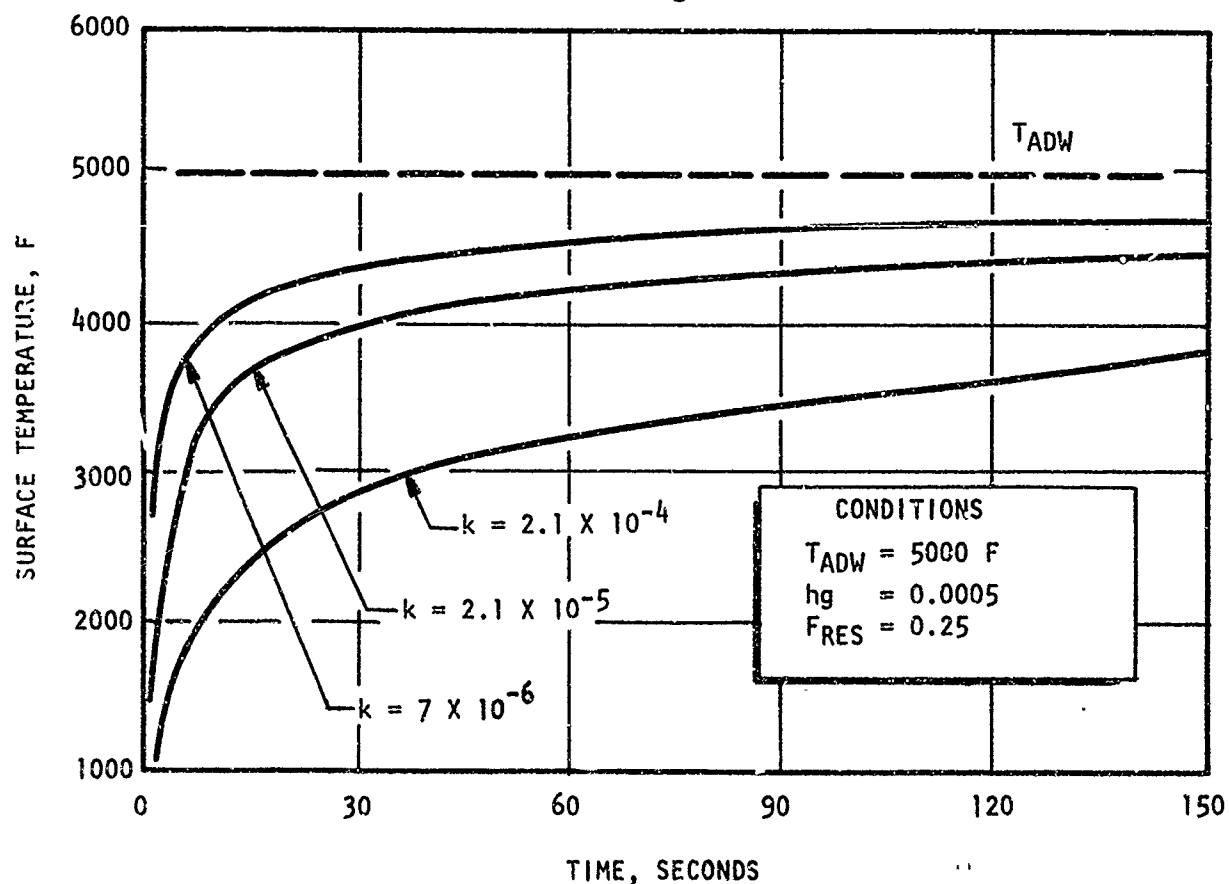Penetration Through Ablative Walls

Figure 30. Effect of Char Thermal Conductivity on the Gas-Side
Surface Temperature of Ablative Walls

using the curves of Fig. 25 through 30, a mean thermal conductivity for the char layer should be estimated.

For low thermal conductivity material, in which the char rate is relatively low and the radius vector does not change drastically with time, the char depth is known to increase approximately as the square root of time. This is true of the curves of Fig. 25 through 27 for burn times greater than approximately 100 seconds.

Adiabatic Wall Temperature

Rates of char front advance at T_{aw} of 3500, 5000, 6000, and 7000 F are compared in Fig. 31. The curves apply for a heat transfer coefficient of 0.0005 Btu/in^2-sec-F, a resin content of 0.25 and a thermal conductivity assumed to vary linearly from 2×10^{-5} to 3×10^{-5} Btu/in-sec-F between 2500 and 7000 F. As shown (Fig. 31), the char depth for a burn time of 150 seconds is almost 50 percent greater for an adiabatic wall temperature of 7000 F than for a temperature of 3500 F.

Even on a one-dimensional basis, the effect of adiabatic wall temperature on char rate is considerably more difficult to generalize than the effect of thermal conductivity. The view factor of the surface to low-temperature regions (free space) determines the degree by which radiation can reduce the heat flux into the wall and thereby reduce the char rate. Similarly, surface reactions can absorb significant amounts of heat to reduce char rate, but the resultant erosion will remove insulating char and thereby increase char rate. The curves of Fig. 31 are for negligible radiation and surface reactions.

An approximate method for calculating the effect of adiabatic wall temperature upon char depth is to apply the formula

$$\frac{(\Delta y_c)_2}{(\Delta y_c)_1} = \frac{\psi (T_{aw})_2}{\psi (T_{aw})_1} \tag{3-5}$$
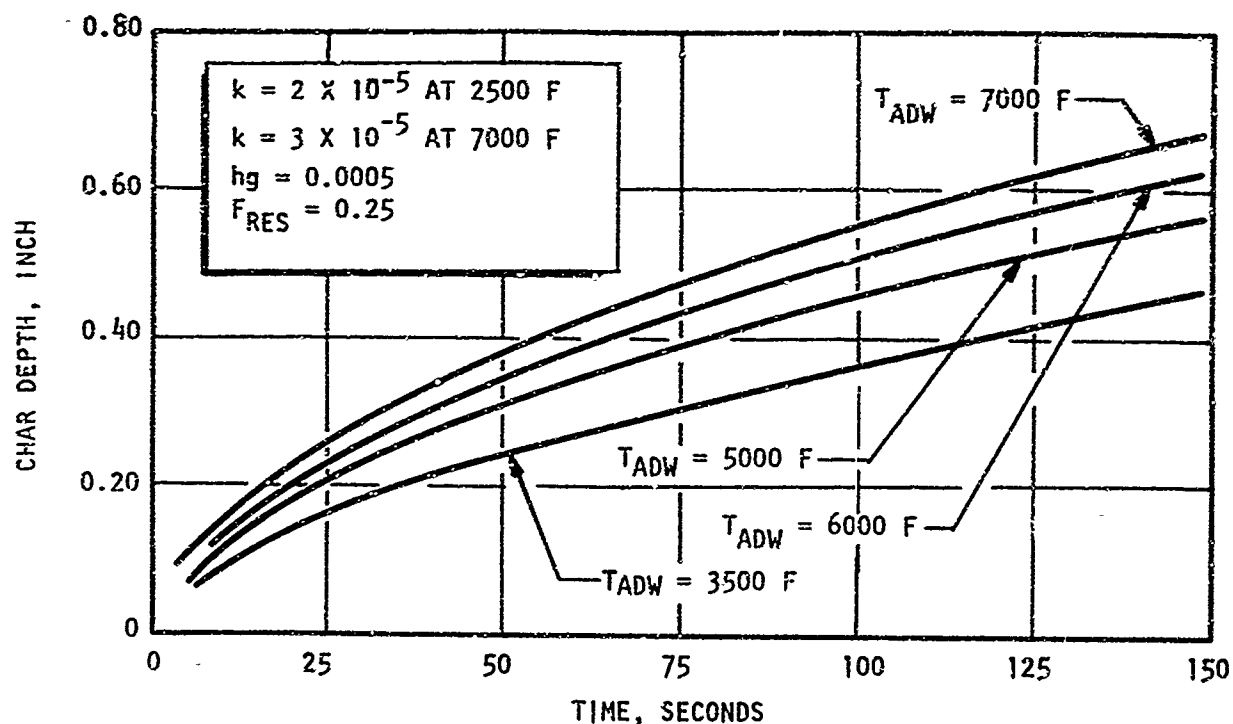
Figure 31. Effect of Adiabatic Wall Temperature
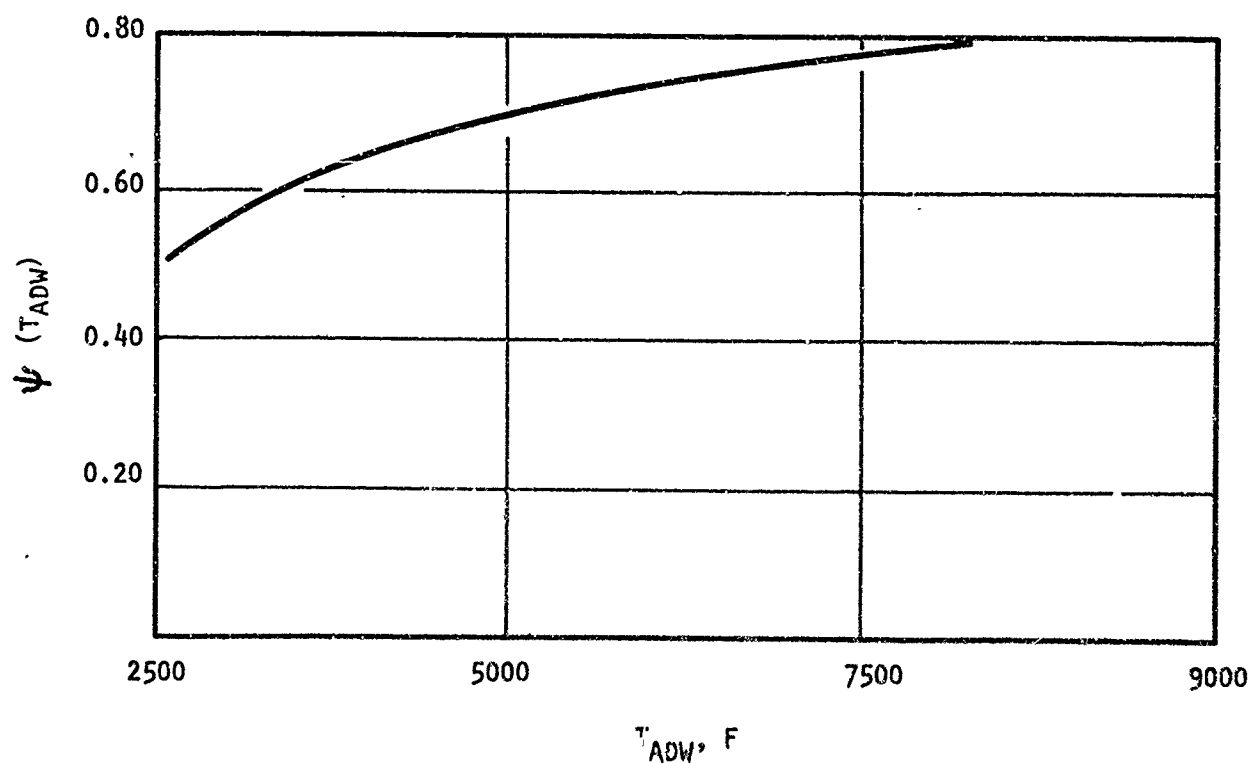on Char Front Advance

Figure 32. Enthalpy Parameter ψ as a Function of
Adiabatic Wall Temperature

91

where the enthalpy parameter ψ is obtained from Fig. 32. The enthalpy parameter is defined by

$$\psi = \sqrt{\frac{\sqrt{T_{aw} - 1200}}{\Delta H}} \qquad (3\text{-}6)$$

where ΔH is the total heat absorbed by resin pyrolysis, gas cracking, and sensible heat absorption by the pyrolysis gases. Equation 3-5 applies for modified Biot numbers greater than 10 and for negligible radiation and surface erosion.

The effect of adiabatic wall temperature upon thermal penetration is shown in Fig. 33. Comparison of Fig. 33 and 31 indicates that the effect of adiabatic wall temperature on thermal penetration can be equated to the differences produced in char rate. Under steady firing conditions, the difference between the thermal penetration front and the char front is effectively independent of adiabatic wall temperature and is a function only of virgin thermal conductivity and time.

The relation between surface temperature and adiabatic wall temperature is shown in Fig. 34. The surface temperature is shown to gradually approach the adiabatic wall temperature. The curves of Fig. 34 can be effectively normalized into a single curve by plotting the ratio

$$\frac{T_{aw} - T_s}{T_{aw} - 1200}$$

vs time as shown in Fig. 35. The results shown in Fig. 35 provide the justification for employing Eq. 3-4 to account for thermal conductivity and adiabatic wall temperature changes from values employed in Fig. 30.

Resin Fraction

The effect of variable phenolic resin content upon the char rate of ablative walls under conditions of high thermal conductivity and high heat
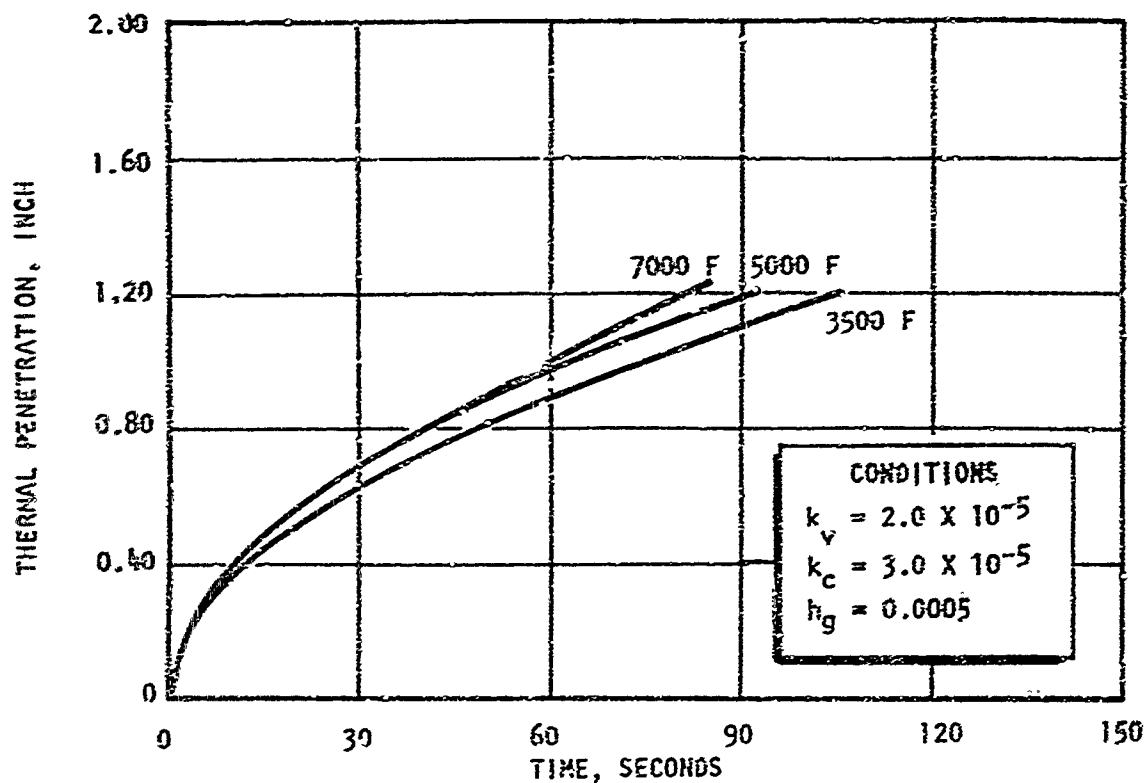
Figure 33. Effect of Adiabatic Wall Temperature on Thermal
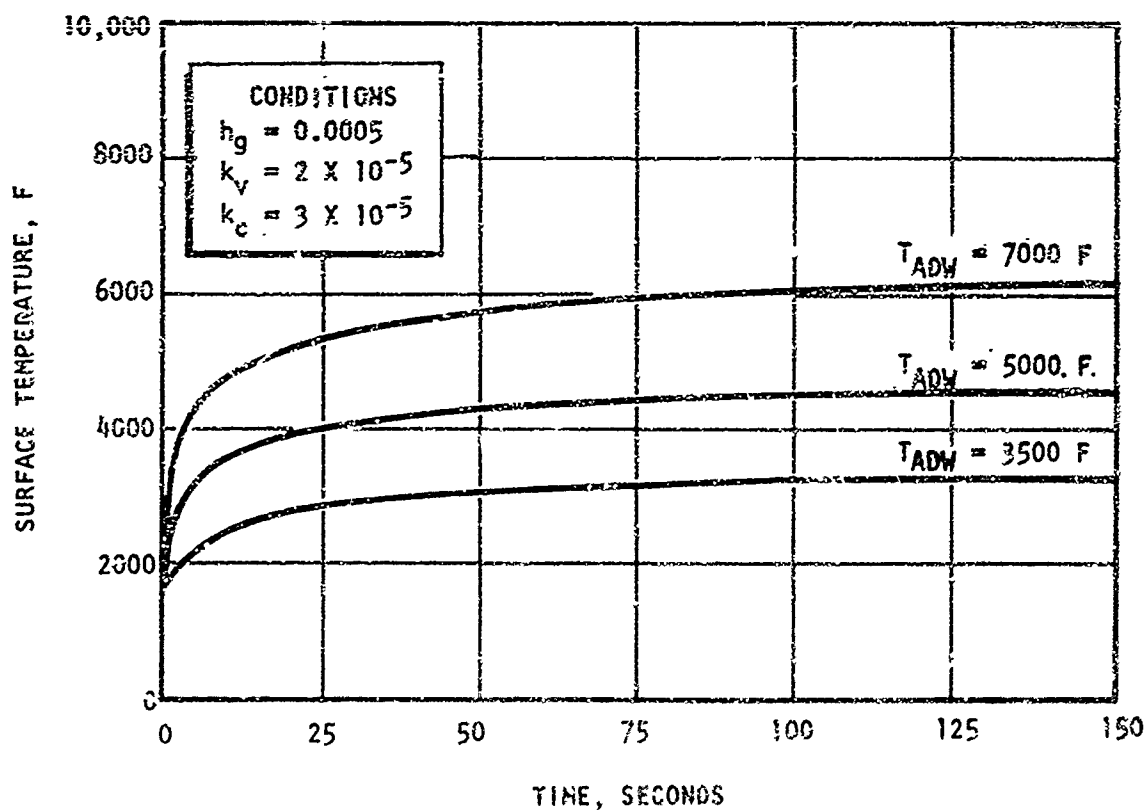Penetration Through Ablative Walls

Figure 34. Effect of Adiabatic Wall Te   .re on the Surface
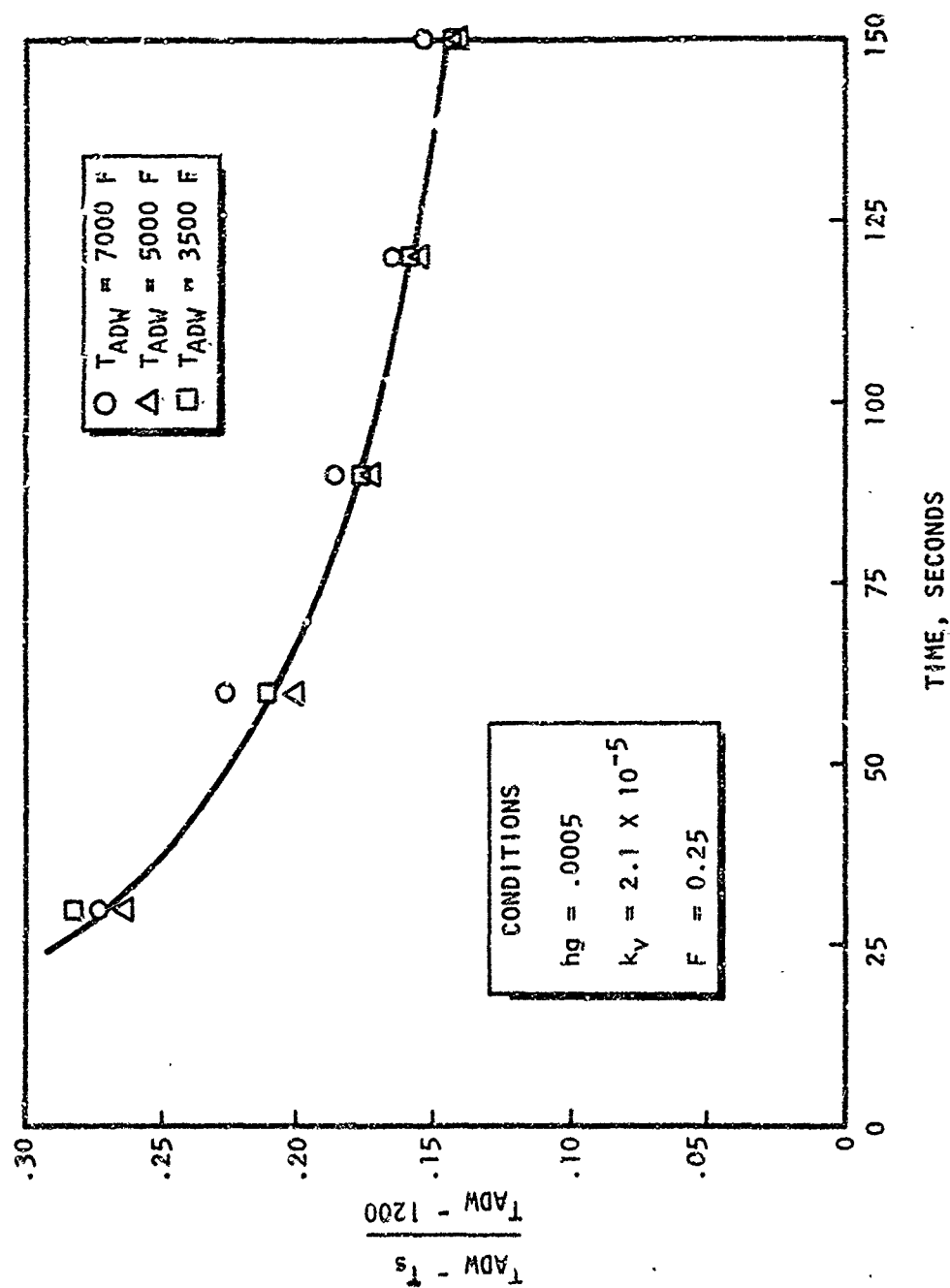Temperature of Ablative Walls

Figure 35. Relation Between Adiabatic Wall Temperature and Surface Temperature Expressed as Unaccomplished Temperature Difference

94

transfer coefficient is shown in Fig. 36 . The two resin fractions.
0.25 and 0.45, represent practical limits for this variable. In Fig. 37
the char rates for the two resin fractions are compared under conditions of
low thermal conductivity and low heat transfer coefficient. As expected,
the larger heat capacity of the high-resin-content ablative material re-
sults in a lower char rate. The effect of resin content on char rate is
not amenable to generalization under high heat transfer conditions because
of the coupled effect of chamber radius on overall heat capacity and radial
char conductance, $(k/\Delta y_c)$. Under conditions of lower heat flux, and partic-
ularly for conditions in which the modified Biot number defined by Eq. 3-1
is greater than 10, the effect of resin content on char rate can be approx-
imated by

$$\frac{(\Delta y_c)_2}{(\Delta y_c)_1} = \sqrt{\frac{F_{R\,1}}{F_{R\,2}}} \qquad (3\text{-}7)$$

The effects of resin content on thermal penetration are shown in Fig. 38
For high conductivity ablatives, the effect of resin content on thermal
penetration is negligible. For low conductivity ablatives, higher resin
content reduces thermal penetration by the same degree to which it reduces
the char rate. Under steady firing conditions, the difference between
the thermal penetration front and the char front is independent of resin
fraction and depends only on the virgin thermal conductivity and the burn
time.

The surface temperature histories of ablative walls with resin contents
of 0.25 and 0.45 for an adiabatic wall temperature of 5000 F, a heat
transfer coefficient of 0.0005 Btu/in^2-sec-F and an average char thermal
conductivity of 7×10^{-6} Btu/in-sec-F are compared in Fig. 39 . The
resin fraction is shown to have a negligible effect on surface temperature.
A similar result is obtained over wide ranges of thermal conductivity,
adiabatic wall temperature, and gas-side heat transfer coefficient. How-
ever, close to the point of complete depletion of resin, the surface
temperature deflects upwards. The lower the initial resin content, the
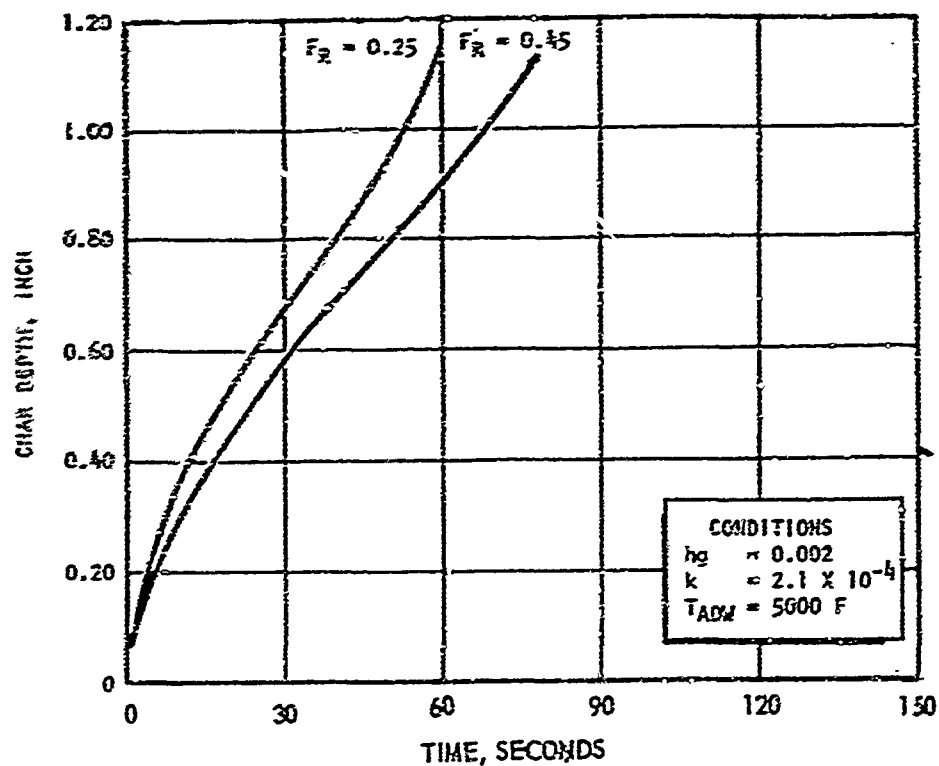earlier is the inflection of the associated temperature history.

Figure 36. Effect of Resin Fraction on Char Front Advance
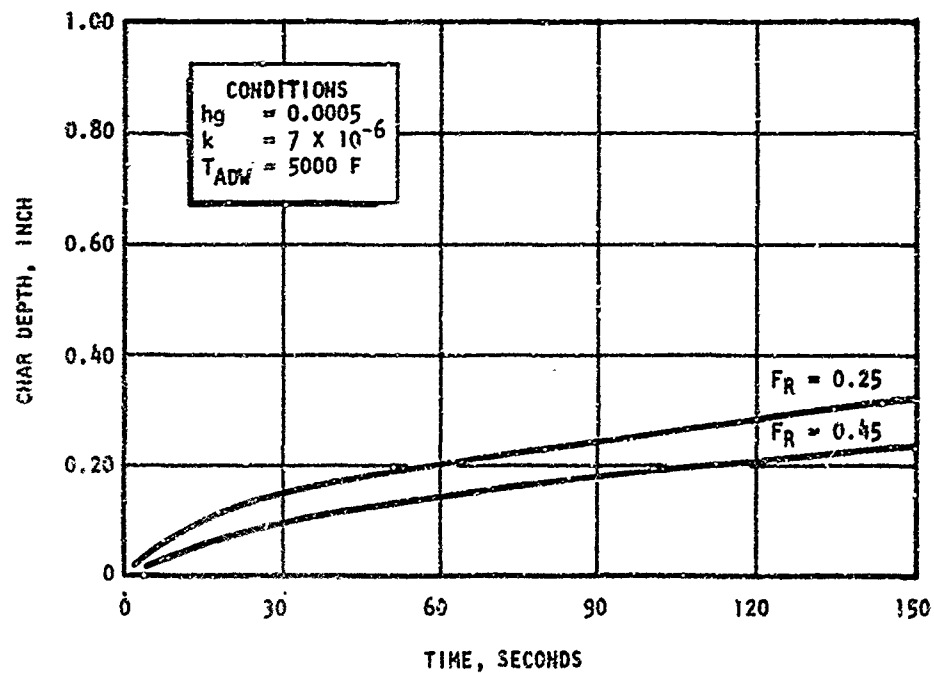For High Thermal Conductivity and High Heat
Transfer Coefficient

Figure 37. Effect of Resin Fraction on Char Front Advance
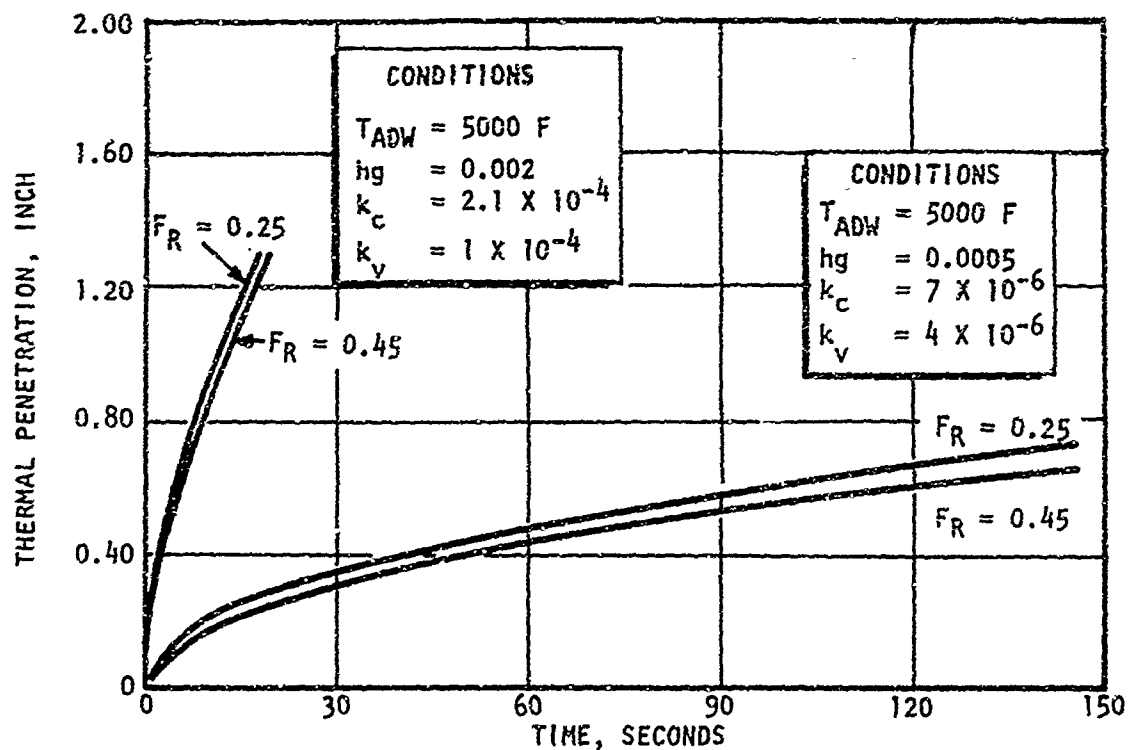For Low Thermal Conductivity and Low Heat
Transfer Coefficient

96

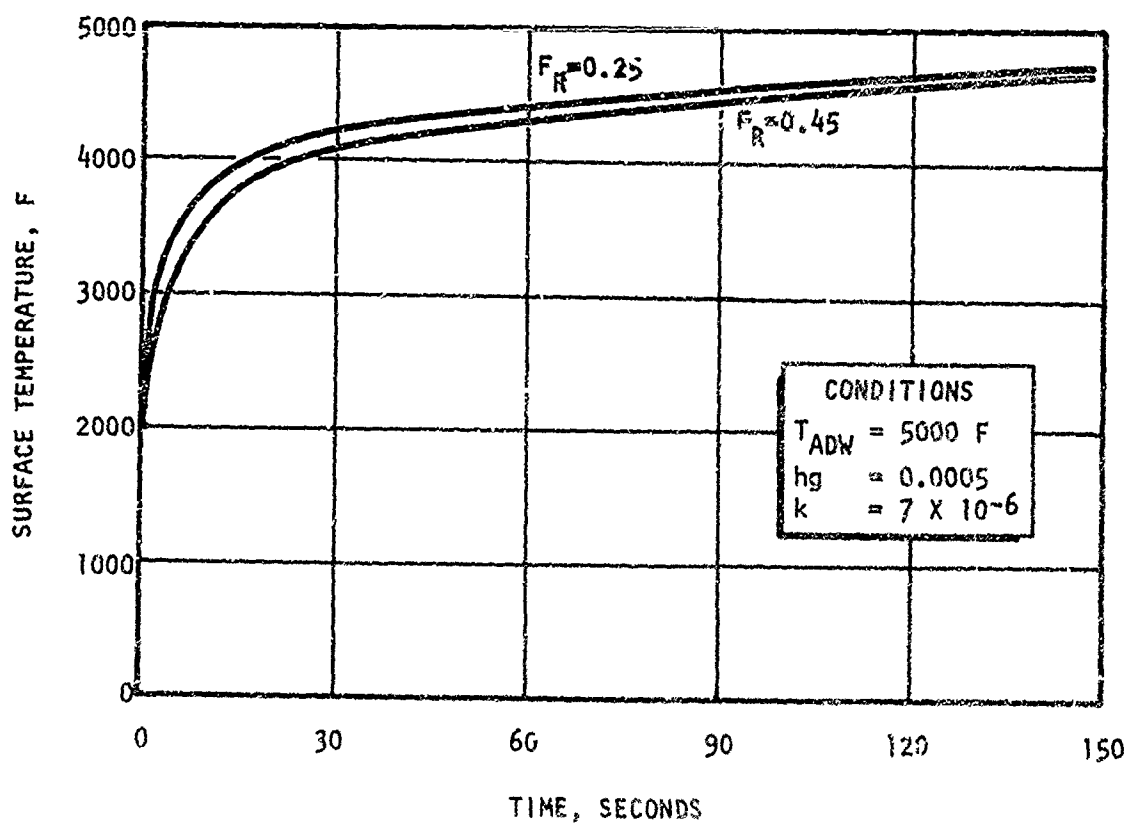Figure 38. Effect of Resin Fraction on
Thermal Penetration

Figure 39. Effect of Resin Fraction on Surface
Temperature of Ablative Walls

97

Heat Transfer Coefficient

The effect of heat transfer coefficient upon char rate through high conductivity and low conductivity ablatives is shown in Fig. 40 and 41, respectively. Through a high conductivity wall, the effect of an increasing heat transfer coefficient is to significantly increase the char rate. In fact, for low values of the modified Biot number defined by Eq. 3-1, the increase in char rate is more than proportional to the increase in heat transfer coefficient. For low conductivity ablatives (Fig. 41), the effect of heat transfer coefficient becomes negligible for heat transfer coefficients above 0.001 Btu/in^2-sec-F. In terms of chamber operating variables, this means that char rate is essentially independent of chamber pressure for chamber pressures above approximately 200 psia.

The effect of heat transfer coefficient on the surface temperature of a low conductivity ablative is shown in Fig. 42. For low conductivity ablatives, and with negligible endothermic surface reactions and surface radiation, the surface temperature closely approaches the adiabatic wall temperature for high or moderate heat transfer coefficients. In fact, for chamber pressures above 200 psia, the ablative surface temperature for low conductivity ablatives* will approximate the adiabatic wall temperature within 100 F in the combustion chamber. No simple general statement can be made with regard to high thermal conductivity ablatives.

The effect of heat transfer coefficient upon thermal penetration through a low conductivity ablative is shown in Fig. 43. As with the adiabatic wall temperature and the resin content, the effect of heat transfer coefficient is to shift the thermal penetration front by a distance equivalent to the shift in char front.

Chamber Radius

The effect of chamber radius on char rate is shown in Fig. 44. For low values of ablative-wall thermal conductivity and heat transfer coefficient, there is essentially no difference in the char depth between chamber radii

---

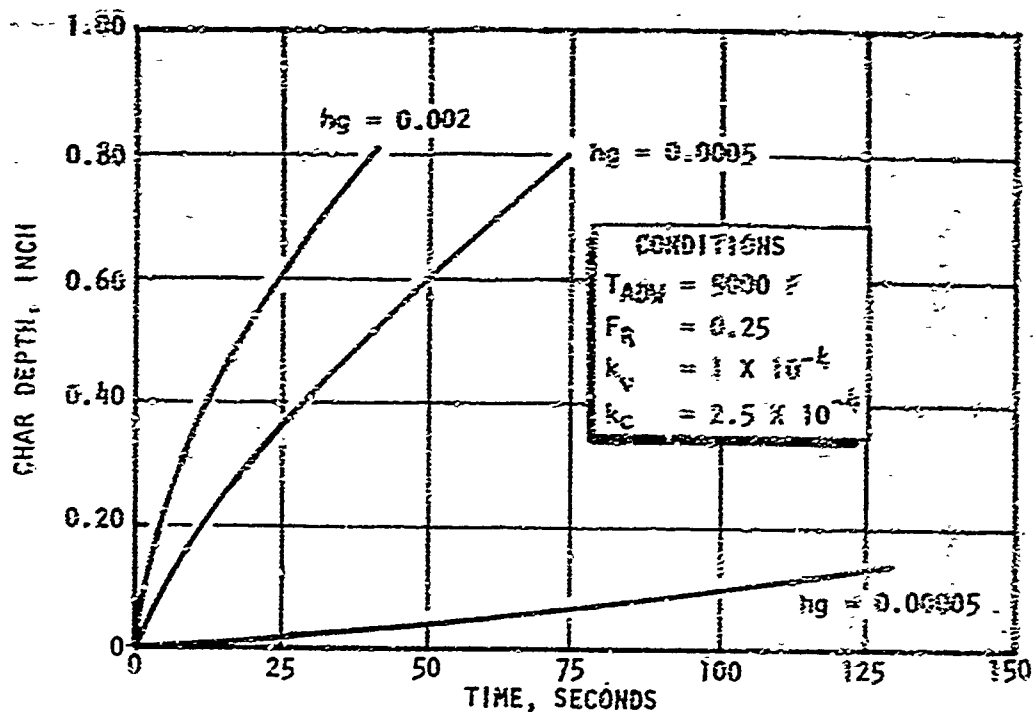*Phenolic-refrasil or phenolic-graphite at orientations greater than 75 degrees.

98

Figure 40. Effect of Heat Transfer Coefficient on Char Front
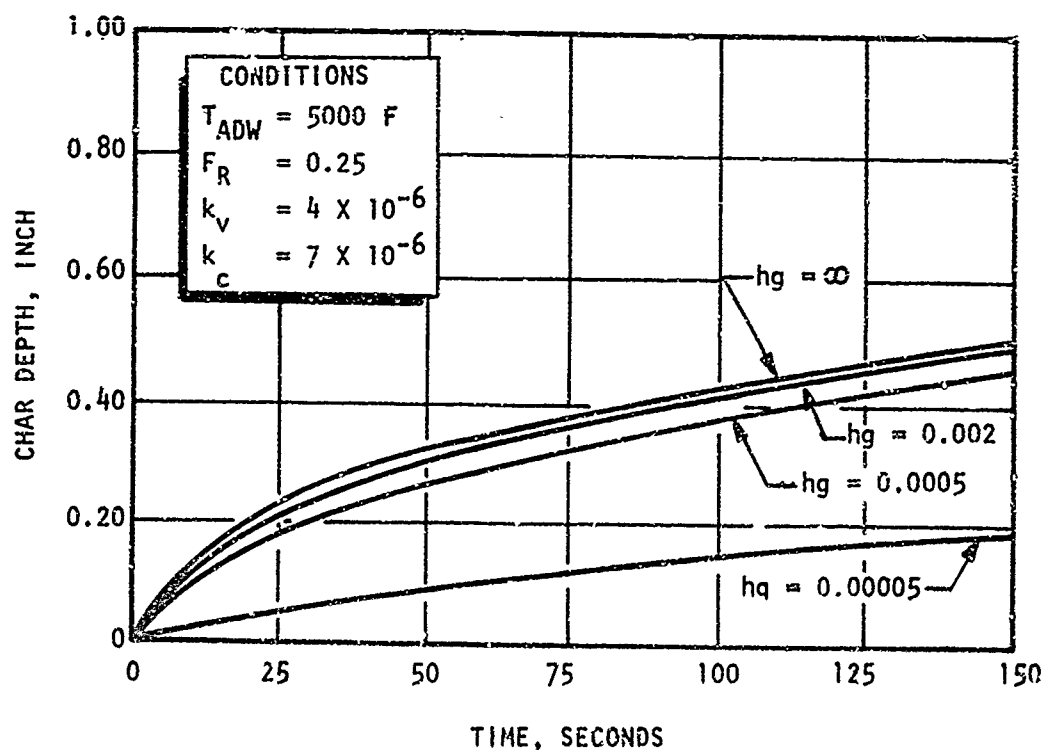Advance Through a High Conductivity Ablative

Figure 41. Effect of Heat Transfer Coefficient on Char Front
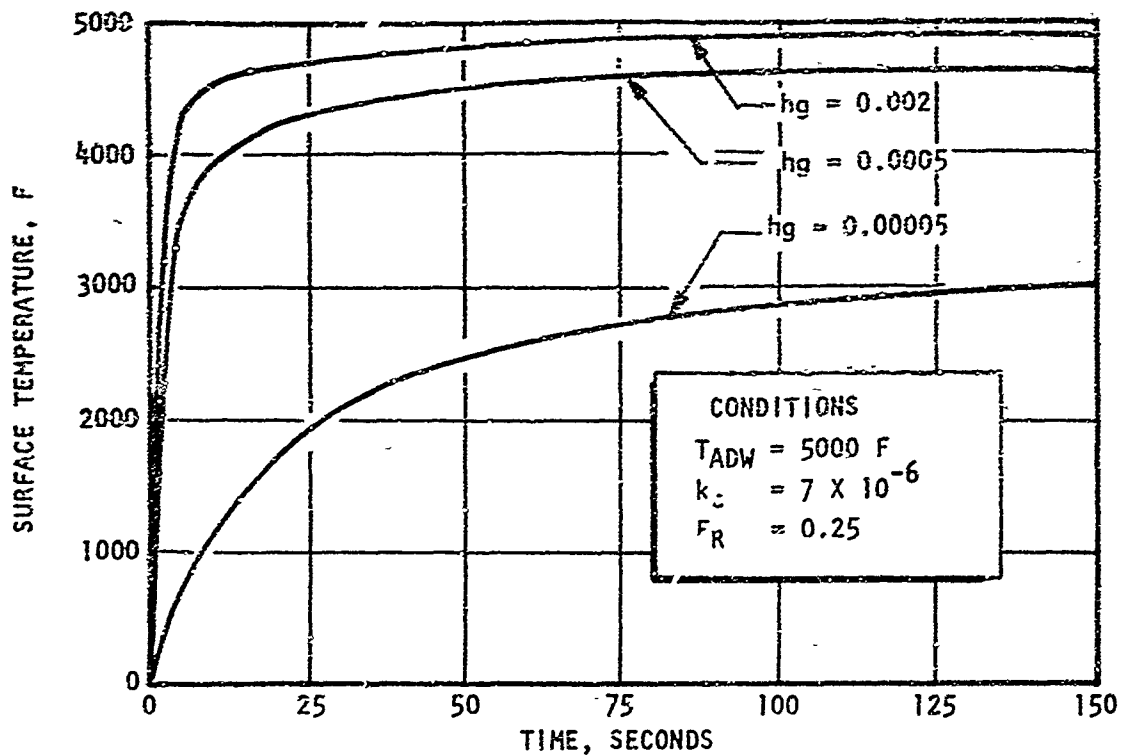Advance Through a Low Conductivity Ablative

Figure 42. Effect of Heat Transfer Coefficient on Surface Temperature of Low-Conductivity Ablative
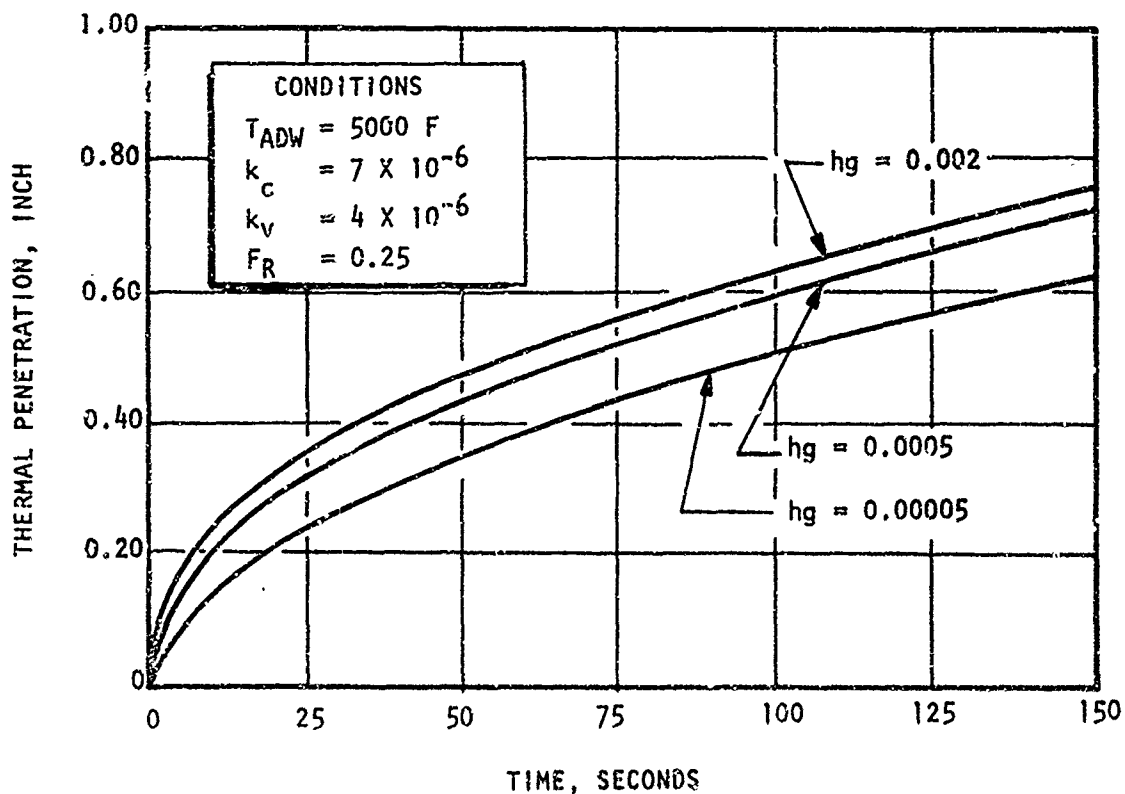

Figure 43. Effect of Heat Transfer Coefficient on Thermal Penetration Through Low-Conductivity Ablative Walls
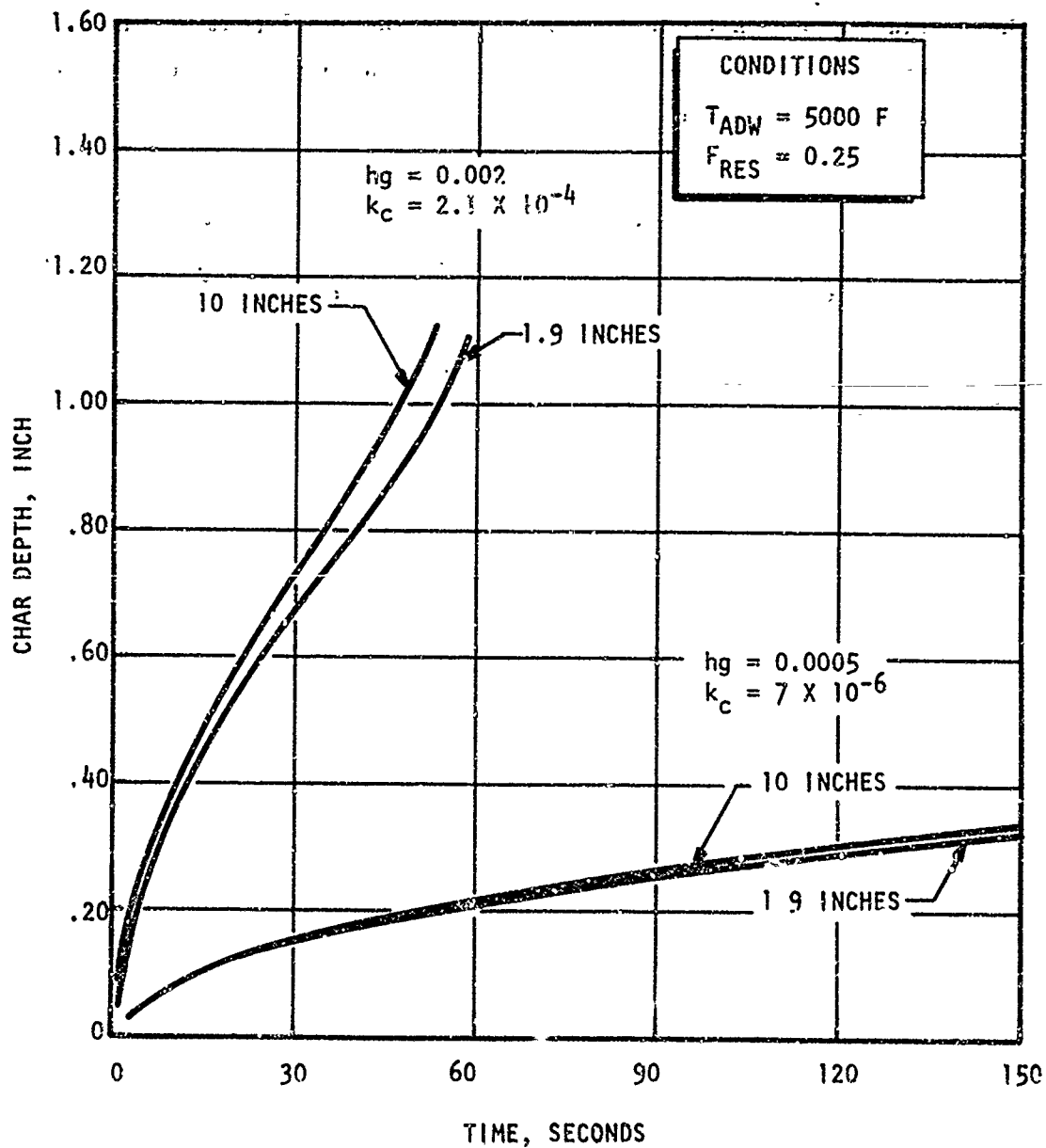
100

Figure 44. Effect of Chamber Radius on Char Front Advance

of 1.90 and 10.0 inches. For high values of ablative wall thermal conductivity and heat transfer coefficient, the char depth for a chamber radius of 1.90 inches is less than for a chamber radius of 10.0 inches. The difference represents the competing effects of the greater heat sink per unit area of hot-gas surface and the greater average normal area to conduction heat transfer per unit hot-gas surface for the small chamber radius. Because the correction for chamber radius is small, the approximation resulting from solution of the implicit relation

$$\frac{(\Delta y_c)_2}{(\Delta y_c)_1} = \frac{\left(R_{o_1} + \Delta y_{c_1}\right)^2 - R_{o_1}^2}{\left(R_{o_2} + \Delta y_{c_2}\right)^2 - R_{o_2}^2} \left(\frac{R_{o_2} + 1/2(\Delta y_c)_2}{R_{o_1} + 1/2(\Delta y_c)_1}\right) \quad (3\text{-}8)$$

may be employed for low thermal conductivity ablatives. To correct the parametric curves of this manual for chamber radius, a value of 1.90 inches should be employed for R_{o_1}.

The effects of chamber radius on surface temperature and thermal penetration are negligible for ablative materials and need not be shown. This is not necessarily the case for passive refractory surfaces.

NOZZLE THROAT EROSION

Surface erosion in ablative rocket engine walls is important primarily in the nozzle throat region because the throat area increase produced by recession may reduce chamber pressure which in turn effects thrust, specific impulse, and propellant flowrates. Some estimation of throat lifetime is therefore desirable before a preliminary multimaterial, rocket-engine wall configuration should be specified for analysis by 2D-ABLATE.

Experimental results (Ref. 25) of firings with the propellant combination of NTO/50% N_2H_4 - 50% UDMH (flame temperature = 5180 F) indicate that refrasil-reinforced ablative materials are poor choices for throat walls for chamber pressures of 100 psia or higher. In environments which do not contain water vapor, phenolic/carbon-cloth soft throats might be considered for low chamber pressures. However, hard graphite throats would be preferable from strength considerations.

The common materials for hard throat inserts are silicon carbide for propellant combinations such as NTO/50% N_2H_4 - 50% UDMH which contain appreciable amounts of water vapor and graphite for fluorinated oxidizer systems which contain little or no water vapor. In noncorrosive gas streams, graphite is able to withstand higher temperatures than silicon carbide which vaporizes because of decomposition at temperatures in the neighborhood of 4700 F (Ref. 21).

The erosion mechanisms for ATJ graphite provided for in 2D-ABLATE include vaporization and chemical reaction. Vaporization is a function of adiabatic wall temperature together with heat and mass transfer coefficients which jointly determine the surface temperature (vapor pressure) and rates at which heat diffuses to the surface and carbon vapors diffuse into the main gas stream. Chemical reaction is determined by adiabatic wall temperature, heat transfer coefficients and free-stream concentrations of corrosive species. To a lesser extent, the thermal conduction of the throat backup material and the view factor to the nozzle exit are also important.

Representative erosion rates for ATJ graphite throat inserts by hydrogen and by water vapor are given in Figs. 45 and 46, respectively, as functions of adiabatic wall temperature and free-stream mole fraction of the reactant gas species. The erosion rates were calculated by a Rocketdyne one-dimensional computer program, THAB, employing the erosion mechanisms of 2D-ABLATE and the recommended erosion properties from Tables 5 through 7. The calculations assume a 2-inch throat diameter, an expansion ratio of 40, and a phenolic-refrasil overwrap. The data apply directly for a chamber pressure of 500 psia. Estimations for other chamber pressures may be obtained from the graphs by employing an effective mole fraction, X_{eff}, defined by

$$X_{eff} = (\frac{p_c}{500})\ X_{p_c}$$

where X_{p_c} is the free-stream mole fraction at the chamber pressure of interest.

Representative erosion rates for silicon carbide throat inserts are given in Fig. 47. The method of calculation and assumed operating conditions are those described in the previous paragraph for ATJ graphite. Because the erosion of silicon is assumed to be strictly by vaporization, the data in Fig. 47 are independent of chamber pressure except for the effect of chamber pressure on heat transfer coefficient and adiabatic wall temperature.
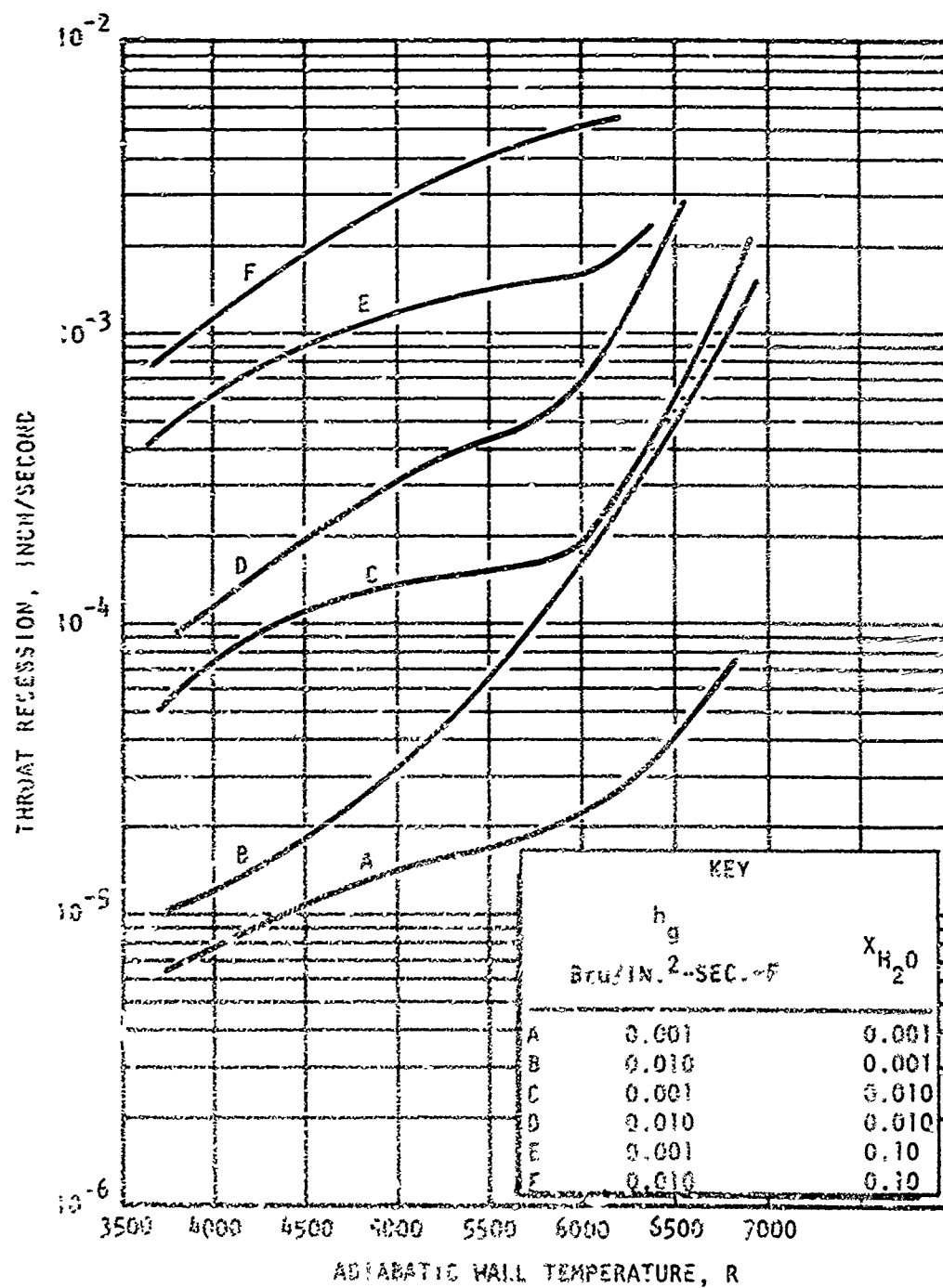
Figure 45   Recession of ATJ Graphite Throat Inserts in a
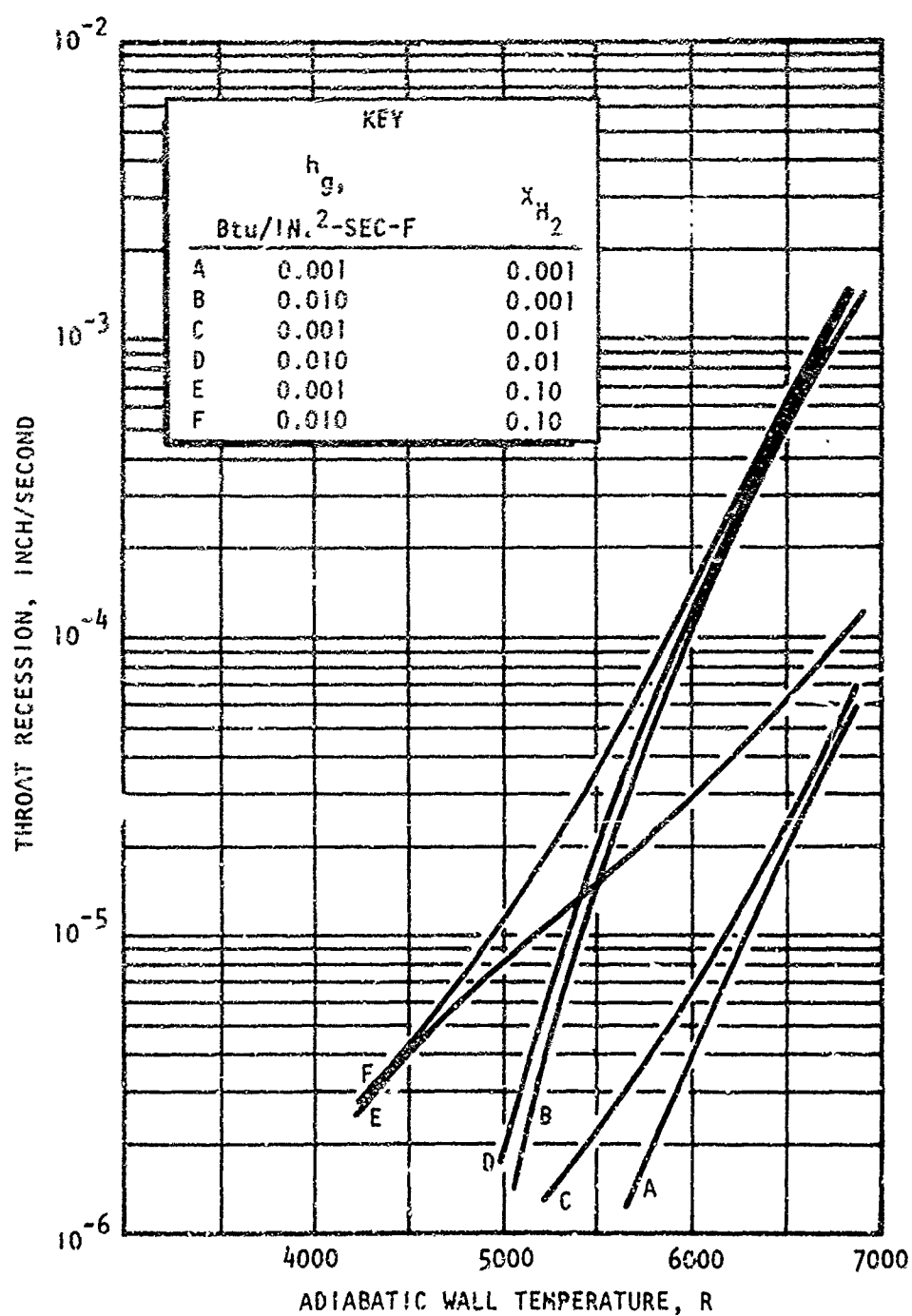Water Vapor Environment at 500-psia Chamber
Pressure

Figure 46. Recession of ATJ Graphite Throat Inserts in a
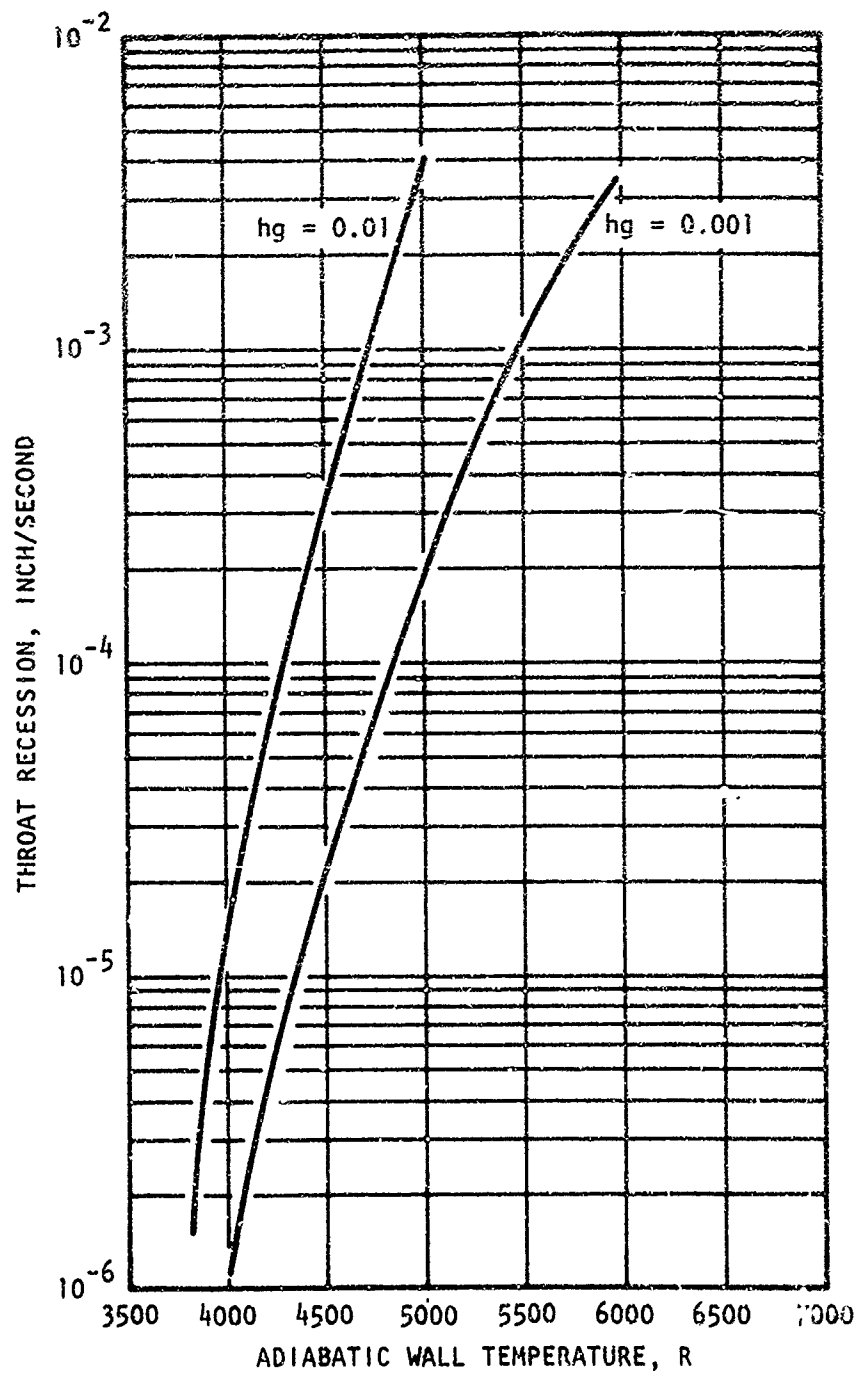Hydrogen Environment at 500 psia

Figure 47. Recession of Silicon Carbide Throat Inserts

TWO-DIMENSIONAL ABLATION

Analysis based upon one-dimensional heat transfer permits estimations of
the required thicknesses of ablative walls, durability of throat inserts,
and insulative overwrap for an ablative engine at given operating condi-
tions. From these estimations and from the chamber dimensions specified
by chamber pressure, thrust, and expansion ratio, a preliminary ablative
wall configuration can be drafted. The char rate and temperature distri-
bution in the actual chamber walls will differ from one-dimensional esti-
mations for the following reasons:

1. The boundary conditions along the combustion chamber and nozzle
   walls vary from the injector to the nozzle exit. These boundary
   conditions include adiabatic wall temperature, heat transfer co-
   efficient, and radiation view factors.

2. The boundaries in the throat region are not normal to the radial
   heat flux vector of a one-dimensional analysis.

3. The differences in thermal conductivity between typical throat
   inserts and ablative materials amplify differences in radial tem-
   perature profile produced by axial variation in boundary condi-
   tions.

4. The anisotropic thermal conductivity of reinforced ablatives will
   amplify axial conduction produced by differences in radial tem-
   perature profile.

To determine the importance of the two-dimensional effects in ablative
chamber walls under steady firing conditions, seven computer runs were
conducted with 2D-ABLATE for representative thrust chamber configurations
and operating conditions. The conditions investigated are listed in
Table 11.

Two propellant combinations, ClF_3/N_2H_4 and N_2O_4/N_2H_4-UDMH(50-50) are con-
sidered. Carbon cloth/phenolic ablative walls in the combustion chamber
and nozzle together with an ATJ graphite throat insert are used with the

TABLE 11

RUN CONDITIONS FOR 2D-ABLATE PARAMETRIC COMPUTATIONS

Computer Run	Propellant Combination	Mixture Ratio	Chamber Pressure, psia	Thrust, pounds	Duration, seconds	Contraction Ratio	Expansion Ratio	Combustion Chamber Wall	Throat	Nozzle Wall	Overwrap
1	ClF_3/N_2H_4	2.5	500	10,000	300	2	20	Phenolic carbon cloth, 45-degree orientation, 0.50 inch thick	ATJ graphite	Phenolic carbon cloth, 45-degree orientation, 0.50 inch thick	Phenolic refrasil, 75-degree orientation, 1.0 inch thick
2	ClF_3/N_2H_4	2.5	50	200	300	4	40	Same as 1	Same as 1	Same as 1	Same as 1
3	ClF_3/N_2H_4	1.0	50	200	300	4	40	Same as 1	Same as 1	Same as 1	Same as 1
4	$N_2O_4/50-50$	1.0	1000	10,000	300	2	20	Phenolic refrasil, 45-degree orientation, 0.50 inch thick	Silicon carbide	Phenolic refrasil, 80-degree orientation, 0.50 inch thick	Phenolic refrasil, 80-degree orientation, 1.0 inch thick
5	$N_2O_4/50-50$	1.0	50	100	300	2	40	Same as 4	Phenolic refrasil, 45-degree orientation	Same as 4	Same as 4
6	$N_2O_4/50-50$	2.0	50	100	300	2	40	Same as 5	Same as 5	Same as 4	Same as 4
7	$N_2O_4/50-50$	2.0	1000	20,000	300	2	20	Same as 4	Same as 4	Same as 4	Same as 4

ClF_3/N_2H_4 propellant combination because of the compatibility of carbon with HF and also because of the high melting point of the reinforcement. With the N_2O_4/N_2H_4-UDMH (50-50) propellant combination, phenolic-refrasil is used for the combustion chamber and nozzle walls; either phenolic-refrasil or a silicon carbide insert is used at the throat. The operating conditions (Table 11) include both high and low chamber pressure (i.e., high and low heat transfer coefficient) and high and low mixture ratios (i.e., high and low adiabatic wall temperature).

Thrust Chamber Geometry

The ablative motor configurations considered in the two-dimensional computer runs are shown in Fig. 48 through 51. In all configurations, internal wall materials in the combustion chamber and throat regions are surrounded by an overwrap of phenolic-refrasil whose reinforcement is oriented for low radial thermal conductivity. For convenience in computer programming, the boundaries and wall material interfaces consist of straight-line segments. Although these geometries are idealized and impractical from mechanical strength and molding considerations, the general results of the thermal analysis of the simpler geometries are applicable to more complex boundaries.

The mixture ratios given in Table 11 are assumed to be the mixture ratios close to the chamber wall, so that the flame temperature for the subject propellant combination at the given mixture ratio is close to the adiabatic wall temperature once combustion is complete. The heat transfer coefficient in the throat region and in the nozzle is defined from graphical correlations given in Appendix D. Radiation to the nozzle exit is based upon a graphical correlation of view factors given in Appendix D.

On the basis of the analysis of the OF_2/MMH ablative chamber in Task II, the following assumptions were made for the two-dimensional computations:

1. The full length of the combustion chamber is required for combustion; i.e., the local adiabatic wall temperature rises linearly

110

PHENOLIC CARBON CLOTH
PHENOLIC REFRASIL
ATJ GRAPHITE
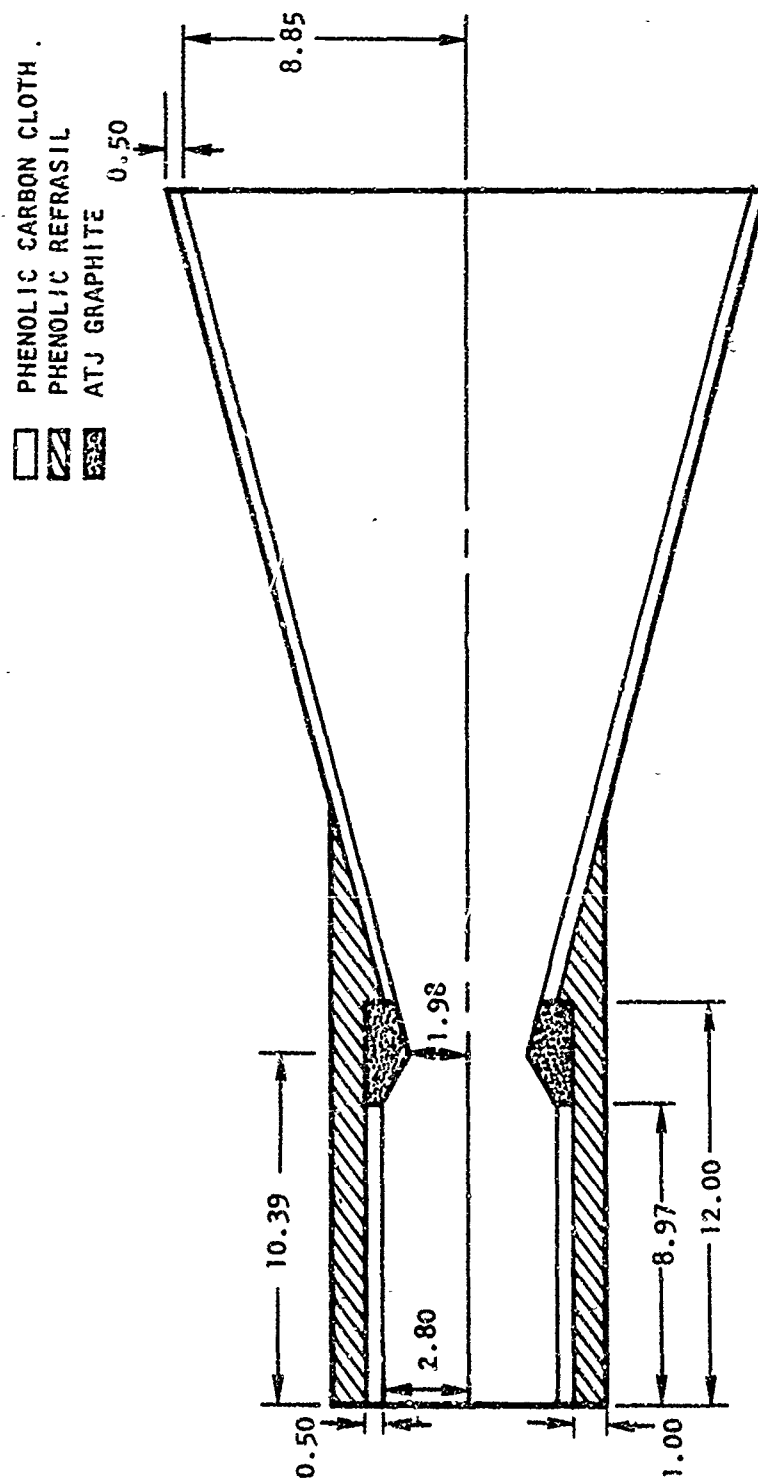
8.85

0.50

1.98

10.39

2.80

8.97

12.00

0.50

1.00

Figure 48. Thrust Chamber Configuration for Computer Run 1

111

PHENOLIC CARBON CLOTH, 45 DEGREES

PHENOLIC REFRASIL, 75 DEGREES

ATJ GRAPHITE

5.36

0.848

22.4

5.64

7.25
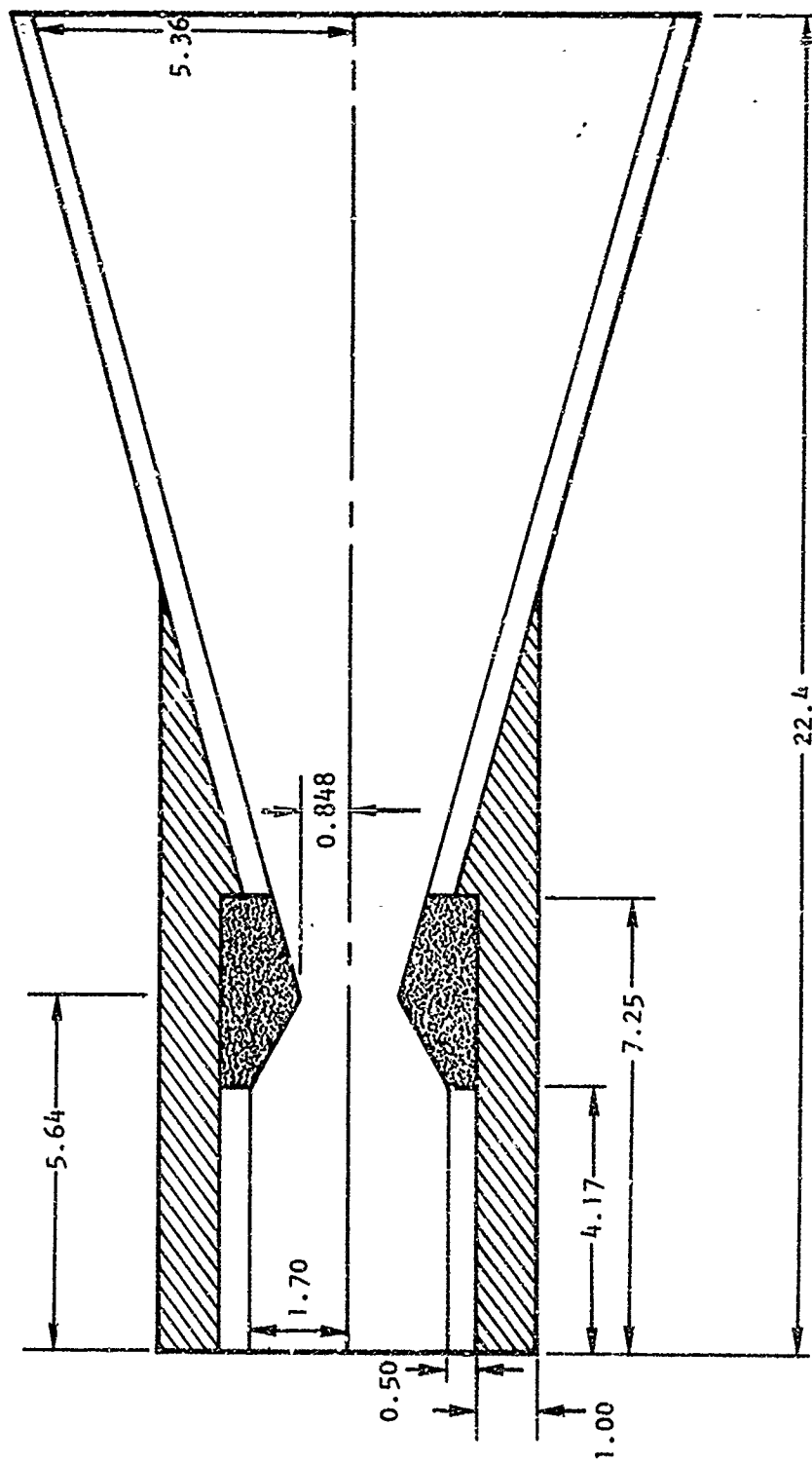
1.70

4.17

0.50

1.00

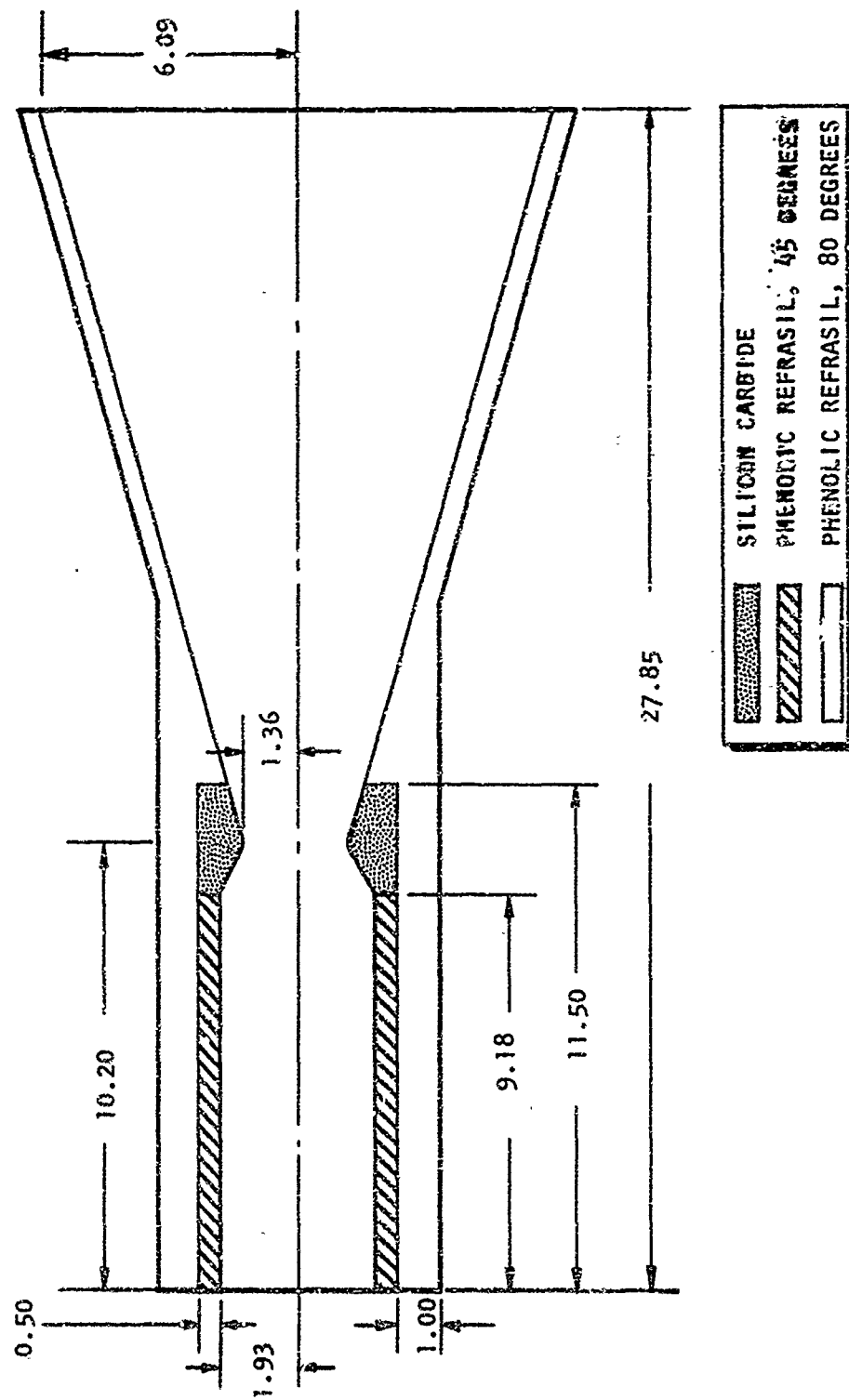Figure 49. Thrust Chamber Configuration for Computer Runs 2 and 3

112

Figure 50. Thrust Chamber Configuration for Computer Runs 4 and 7

113

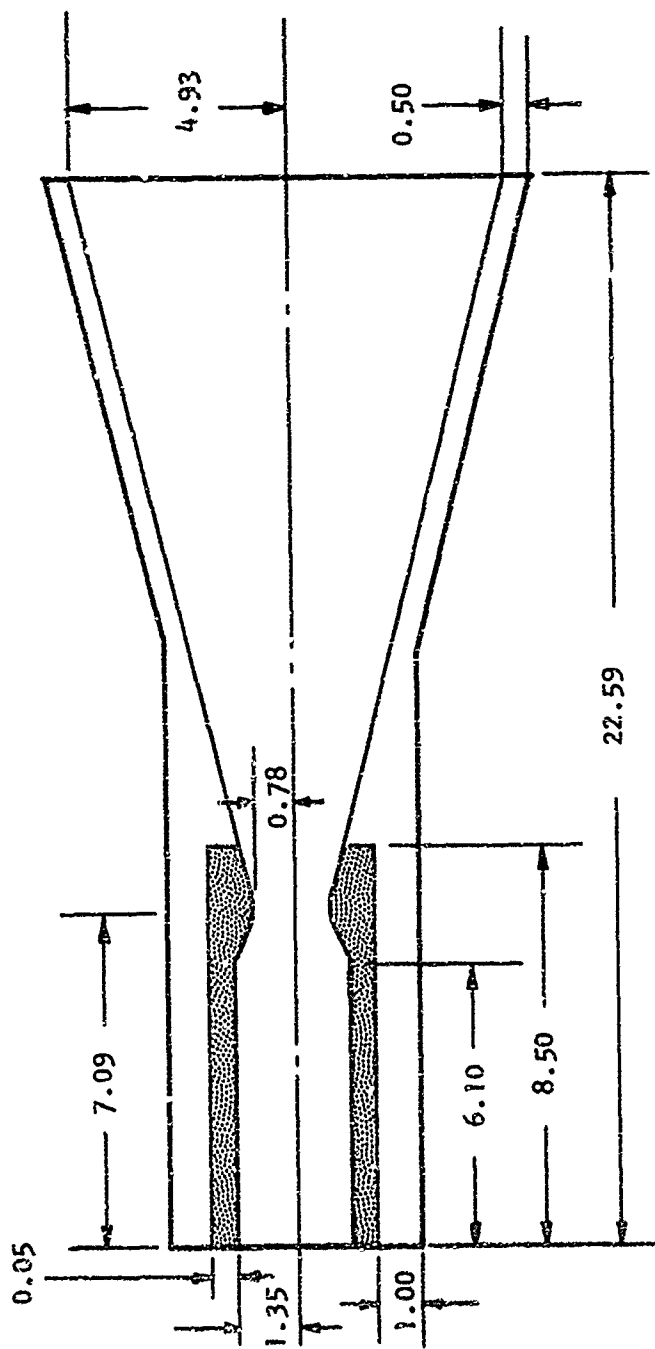**Figure 51.** Thrust Chamber Configuration for Computer Runs 5 and 6

PHENOLIC REFRASIL, 45 DEGREES

PHENOLIC REFRASIL, 80 DEGREES

114

from a value of 2460 R (2000 F) at the injector face to the final adiabatic wall temperature defined by the mixture ratio in the convergent section of the nozzle.

2. The heat transfer coefficient varies locally in the combustion chamber, so that when combined with the ΔT between the true local adiabatic wall temperature and a wall at 500 F (regenerative-cooling wall temperature), the same heat flux is predicted as is obtained by a calculation using the simplified Bartz equation (Ref. 23) for heat transfer coefficient and a ΔT based upon the thermodynamic gas temperature.

The adiabatic wall temperatures after complete combustion and the heat transfer coefficients at the nozzle throat are listed for the seven computer runs in Table 12.

TABLE 12

ADIABATIC WALL TEMPERATURES AND THROAT HEAT TRANSFER
COEFFICIENTS FOR TWO-DIMENSIONAL COMPUTER RUNS

Computer Run	TADW (Mixture Ratio), R	Throat Heat Transfer Coefficient, $Btu/in.^2$-sec-R
1	6780	0.0018
2	6780	0.00029
3	5000	0.00031
4	4600	0.0056
5	4500	0.00038
6	5400	0.00030
7	6000	0.0051

Results

The final char front, gas-side surface temperature profile, and outside
skin temperature profile after a 300-second burn time are graphically
illustrated in Fig. 52 for the chambers lined with the high-conductivity,
phenolic carbon/cloth ablative. In all cases, the char front has penetrated
completely through the carbon cloth ablative into the phenolic-refrasil
overwrap. Around the chamber and throat regions, where the overwrap of
the low-conductivity 75-degree-oriented phenolic-refrasil is 1.0 inch thick,
the outside skin temperature is near or below 100 F. In the nozzle, where
the overwrap tapers to zero thickness, the skin temperature climbs to tem-
peratures over 1000 F. The higher skin temperatures in the nozzle also re-
flect the change in orientation between the overwrap reinforcement and the
nearest hot-gas surface due to the expansion half-angle of the nozzle.

In all cases shown in Fig. 52, the inner surface temperatures rise in the
combustion chamber because of the increase in adiabatic wall temperature.
In the nozzle region, where the adiabatic wall temperature is constant, the
inner surface temperatures fall because of the decrease in heat transfer
coefficient. The difference in the inner surface temperatures shown in
Fig. 52 between computer Runs 1 and 2, which have equivalent adiabatic
wall temperature distributions, shows the effect of chamber pressure (heat
transfer coefficient) upon surface temperature.

Char front and inside and outside surface temperatures for phenolic-refrasil
lined chambers after a 300-second burn time with N_2O_4/N_2H_4-UDMH (50-50) at
a chamber pressure of 1000 psia and mixture ratios of 1.0 and 2.0 are graph-
ically illustrated in Fig. 53. Because of the lower thermal conductivity
of phenolic-refrasil, the char depth is not as high as with the phenolic
carbon-cloth systems. Near the injector end, the char front does not pene-
trate through the inner chamber liner. The lower thermal conductivity
also reduces the outer skin temperature.

For high heat transfer coefficients, the char depth can be calculated by
one-dimensional relations. In Fig. 54 and 55, the char penetration
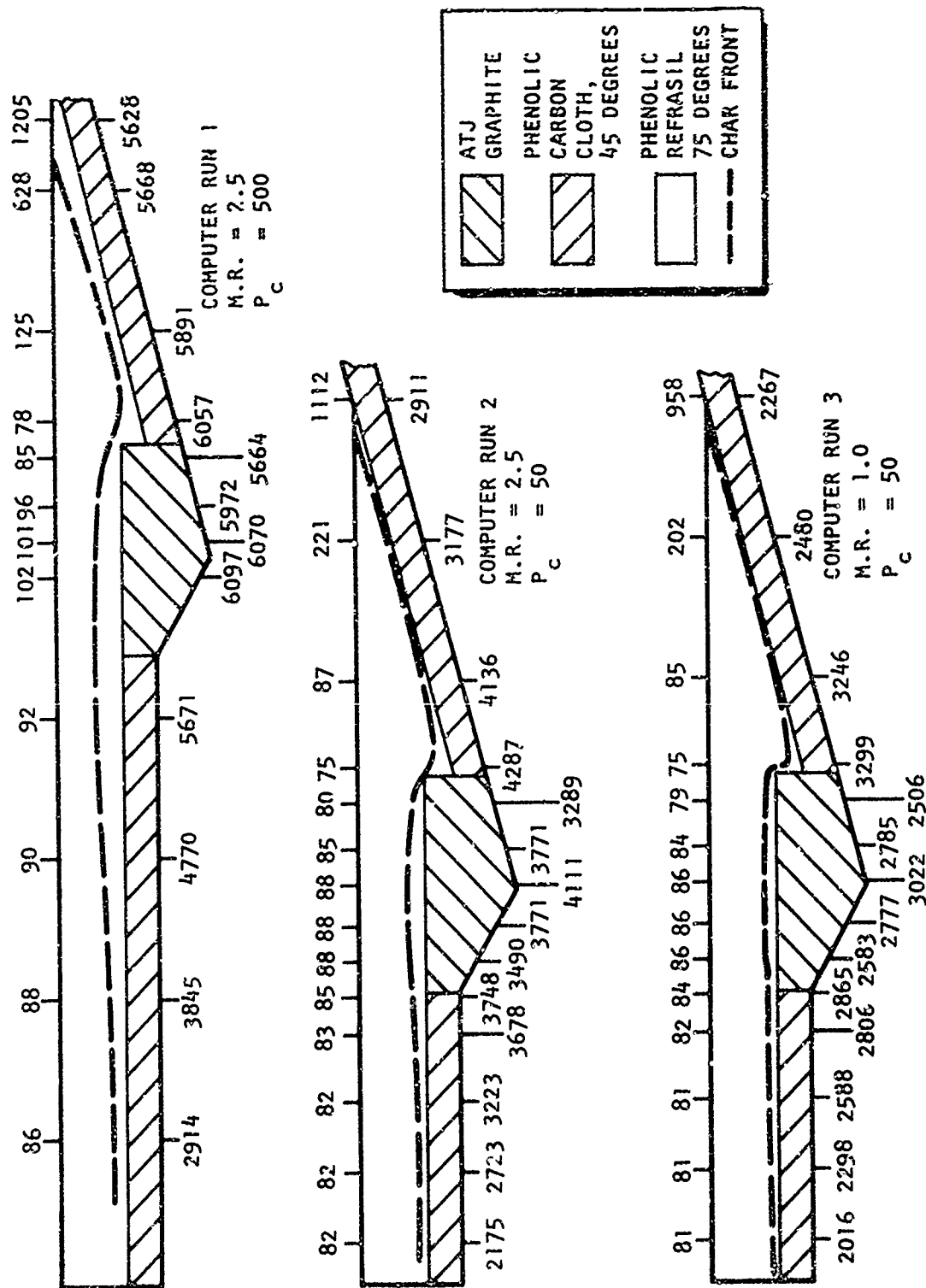
116

Figure 52. Char Fronts, Gas-Side Temperatures, and Outer Skin Temperatures
For Phenolic Carbon Cloth Ablatives After 300-Second Firing
With the Propellant Combination of CTF/N_2H_4

117
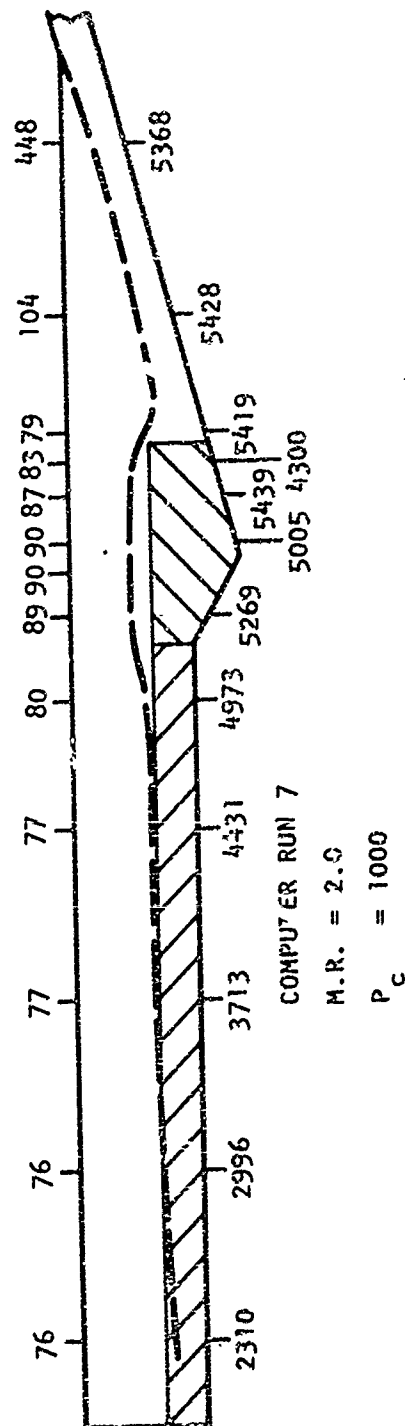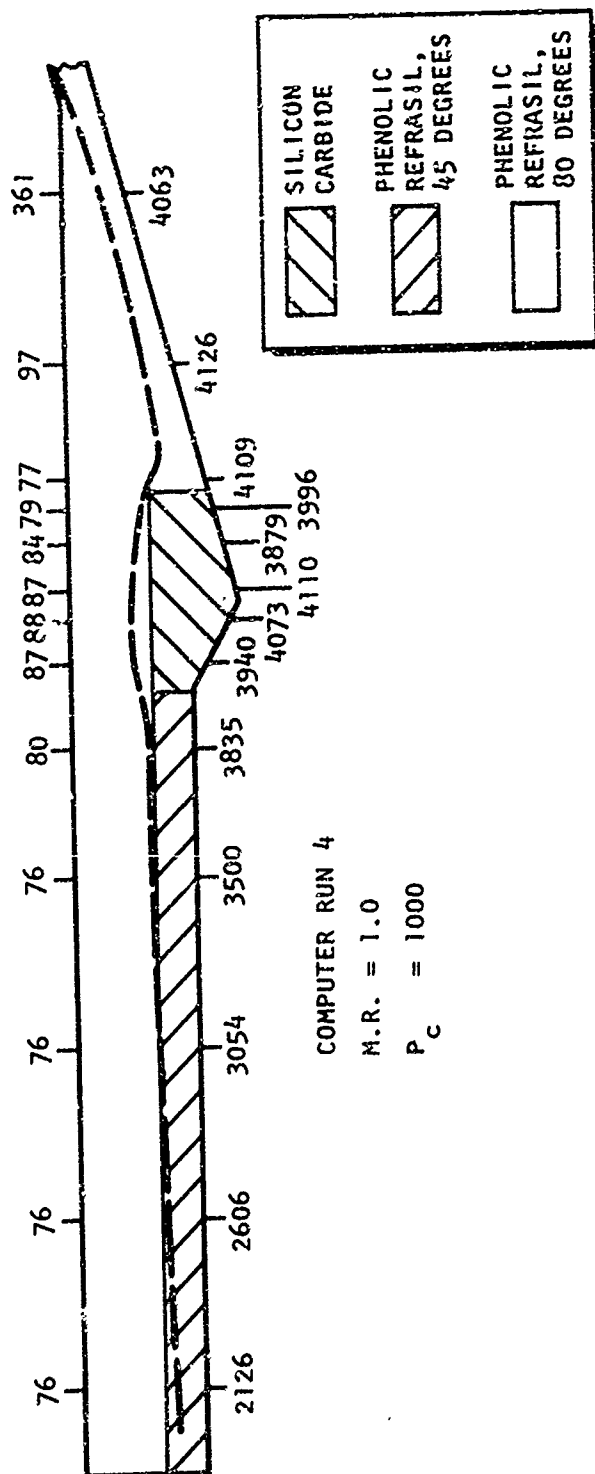
Figure 53. Char Fronts, Gas-Side Temperatures, and Outer Skin Temperatures for Phenolic-Refrasil Ablatives After 300-Second Firing With the Propellant Combination of N_2O_4/50% N_2H_4 – 50% UDMH

Figure 54. Comparison of Combustion-Zone Char Advance By Two- and One-Dimensional Computer Programs -- High Chamber Pressure --

Figure 55. Comparison of Char Advance in Nozzle at an Area Ratio of 2.9 by Two- and One-Dimensional Computer Programs -- High Chamber Pressure --

119

calculated by 2D-ABLATE in computer Run 1 for phenolic/carbon cloth at
a chamber pressure of 500 psia is compared to the char penetration cal-
culated by the one-dimensional graphical relations of Fig. 25 through
44 . In the one-dimensional calculation, local values of adiabatic wall
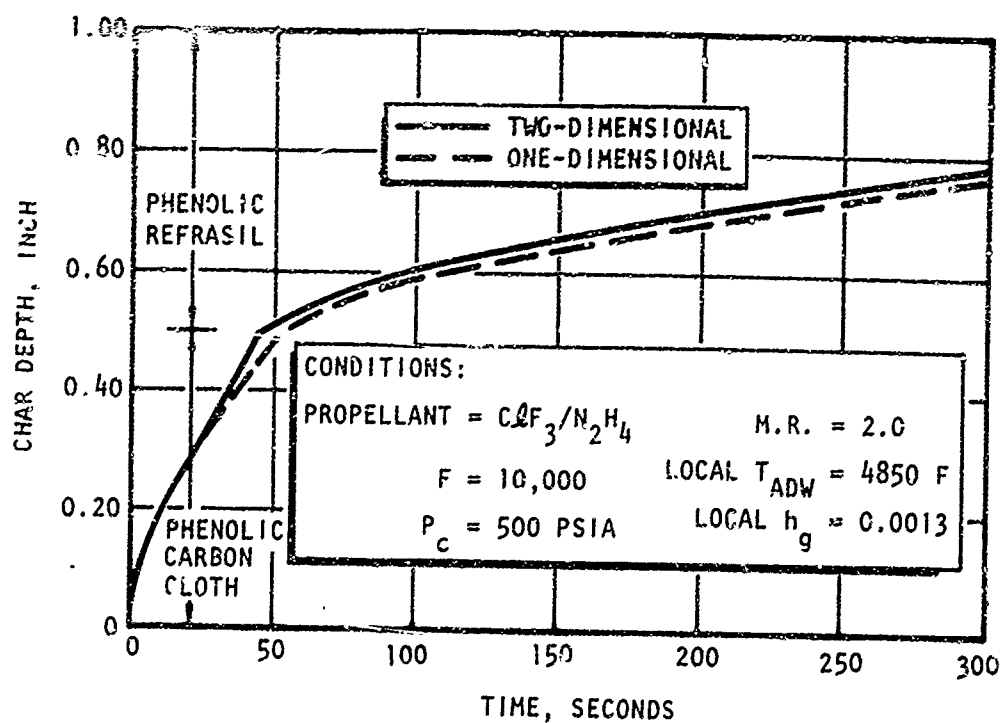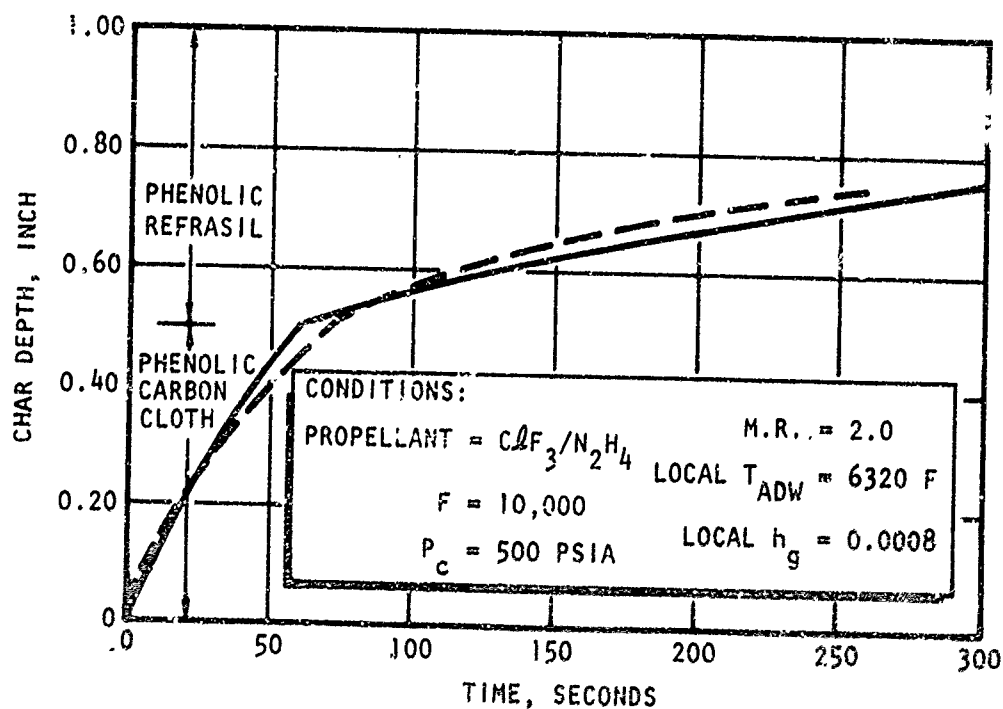temperature and heat transfer coefficient were used together with a radial
thermal conductivity calculated from:

$$K_y = K_\eta \cos^2 \theta + K_\xi \sin^2 \theta$$

and the recommended values of major and minor axis thermal conductivity
from Task 2. Char rate in the overwrap layer was calculated by combining
the thermal resistance of the totally charred inner layer with the gas-
side resistance to yield an overall heat transfer coefficient defined by:

$$\frac{1}{U} = \frac{1}{h_g} + \frac{\Delta x_c}{k_c} \tag{3-9}$$

derived in Appendix E. As shown in Fig. 54 and 55, the agreement between
the one-dimensional and two-dimensional calculations of char depth is
rather good for the operating conditions investigated.

Comparison of the results of one- and two-dimensional calculations of com-
bustion chamber and nozzle char rates for chamber walls of phenolic-refrasil
at a chamber pressure of 1000 psia is given in Fig. 56 through 59 . The
agreement is not as good as with the phenolic/carbon cloth but is certainly
satisfactory for preliminary design purposes, considering the uncertainties
in the specification of adiabatic wall temperature and heat transfer coef-
ficient in real rocket engines.

Operation at low chamber pressures (low heat transfer coefficients) intro-
duces differences between one- and two-dimensional calculations of char
rate (Fig. 60 and 61). In this case, the char rates predicted by 2D-
ABLATE are significantly higher through phenolic/carbon cloth inner cham-
ber liners than those predicted by one-dimensional calculations at a cham-
ber pressure of 50 psia. The difference shown in Fig. 60 and 61 results

Figure 56. Comparison of Char Advance Through Phenolic Refrasil Combustion Chamber Walls by Two- and One-Dimensional Computer Programs at 7.0 Inches From Injector

Figure 57. Comparison of Char Advance Through Phenolic Refrasil Combustion Chamber Walls By Two- and One-Dimensional Computer Programs at 8.5 Inches From Injector

121

Figure 58. Comparison of Char Advance in Combustion Chamber By Two- and One-Dimensional Computer Programs at 8.5 Inches From Injector

Figure 59. Comparison of Char Advance in Combustion Chamber By Two- and One-Dimensional Computer Programs at 7.0 Inches From Injector
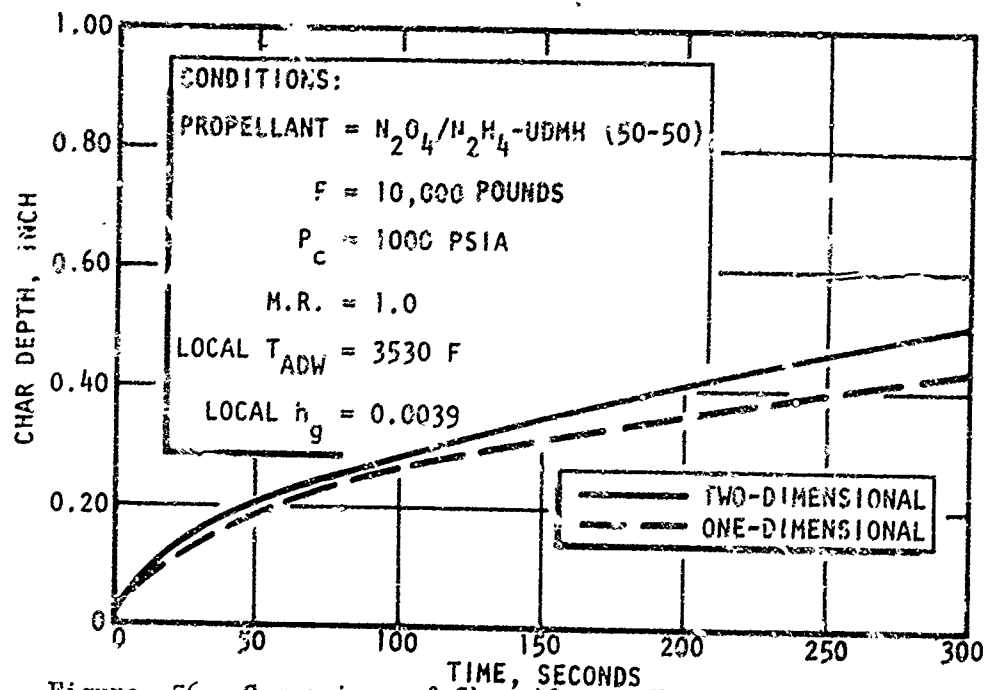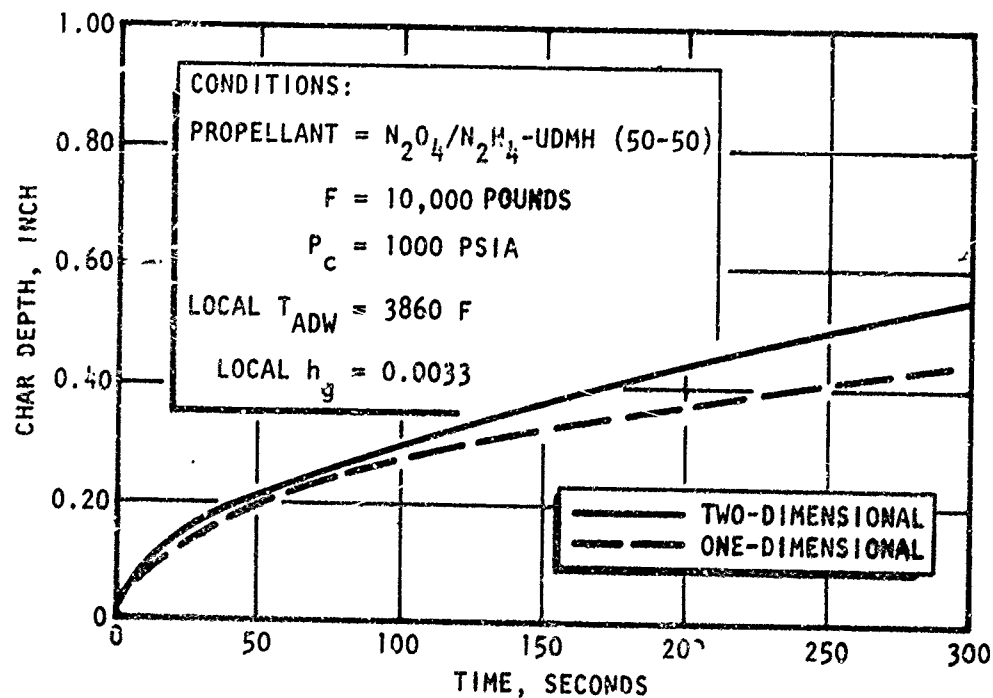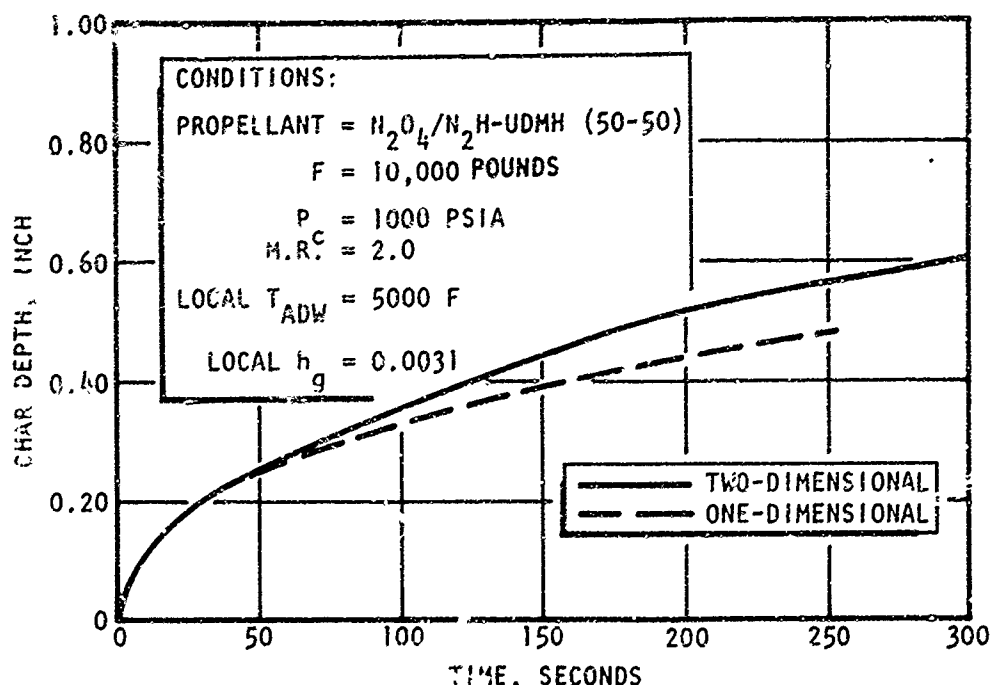
Figure 60. Comparison of Char Advance in Combustion Chamber
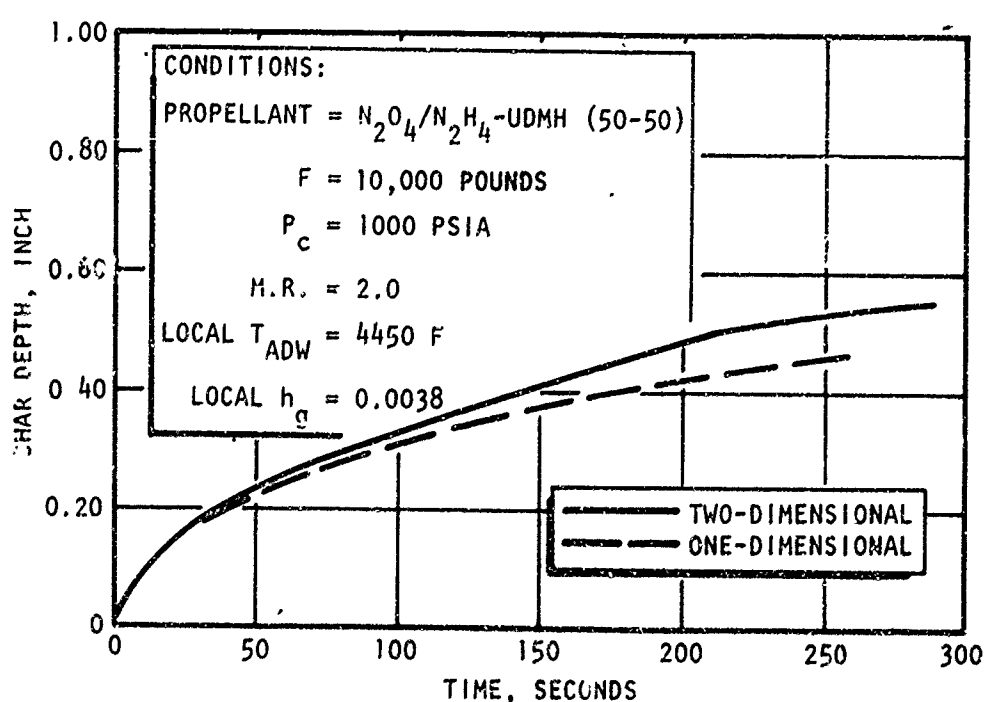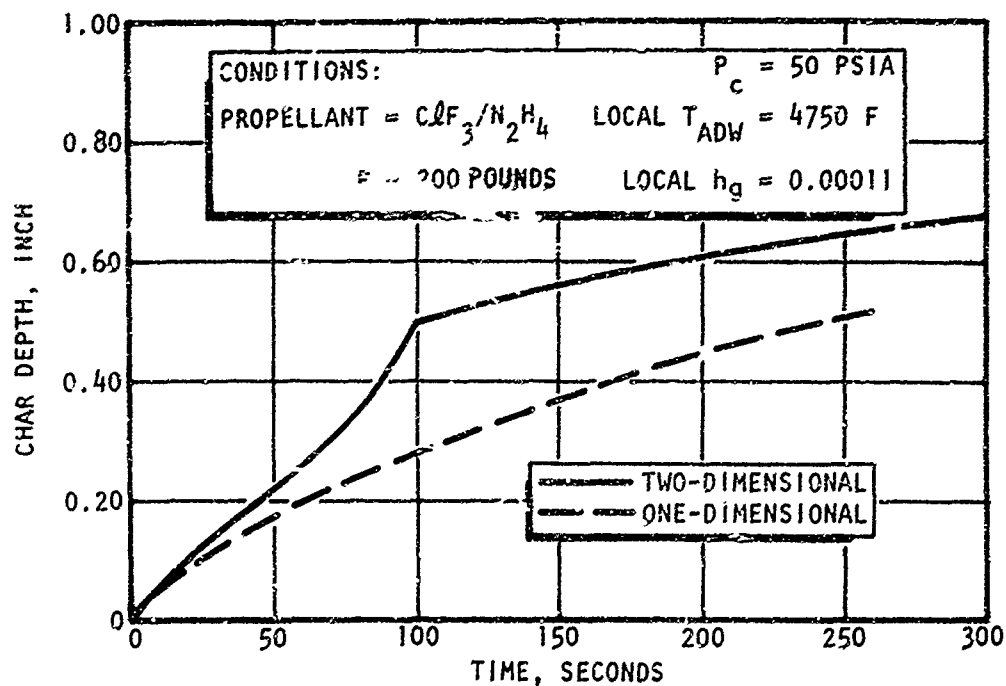By Two- and One-Dimensional Computer Programs at
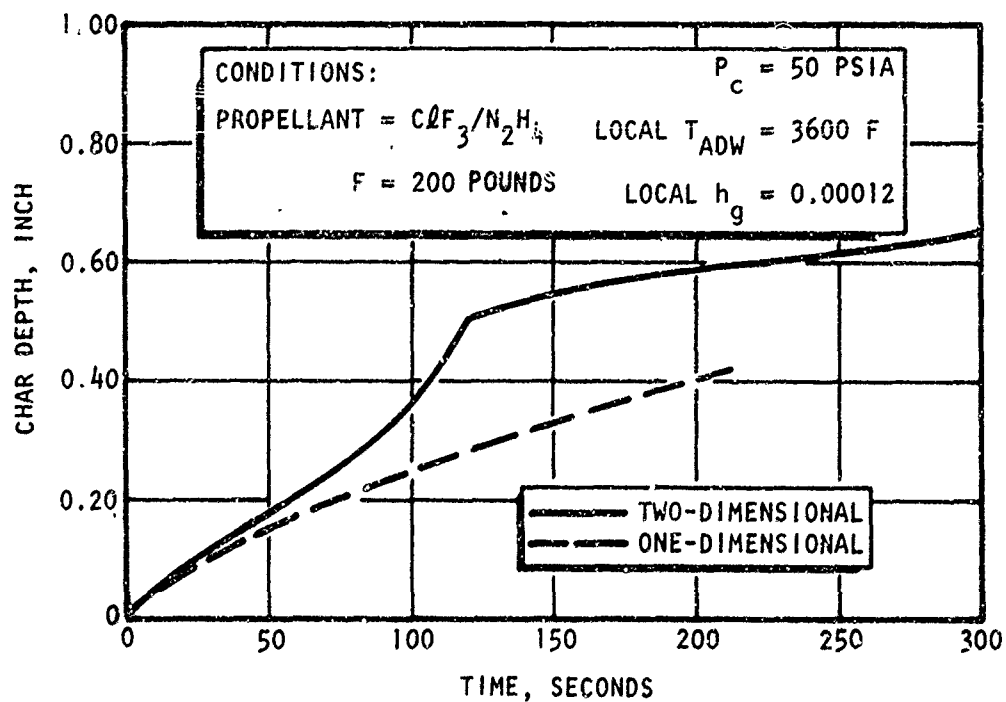3.6 Inches From Injector -- Run 2, Low Chamber Pressure --

Figure 61. Comparison of Char Advance in Combustion Chamber
By Two- and One-Dimensional Technique at 3.6 Inches
From Injector -- Run 3, Low Chamber Pressure --

from the combined effects of the axial gradient in adiabatic wall temperature through the combustion chamber and the high internal conductivity in the phenolic carbon cloth wall relative to the surface heat transfer coefficient at low chamber pressures. The net effect is conduction of extra heat* from the throat region (where the adiabatic wall temperature and heat transfer coefficient are higher) to the combustion chamber walls and, thereby, production of additional charring, above that produced by radial heat transfer. The anisotropic conductivity of reinforced ablatives, particularly favor this type of conduction when the fibers are oriented at appreciable angles from the radial chamber coordinate.

At low chamber pressures, the char rate through soft throat sections is calculated to be higher by 2D-ABLATE than is predicted from one-dimensional calculations (Fig. 62 and 63). In this case, the higher char rates are apparently due to the larger surface area for convective heat transfer in the throat region relative to the area defined for one-dimensional radial heat transfer, i.e., the throat acts like a fin. At high chamber pressures, where the surface resistance to heat transfer is negligible compared to the internal resistance in the walls, the fin effect of the throat is insignificant.

Gas-side surface temperatures at relatively high and relatively low chamber pressures are presented in Fig. 64 and 65. At high chamber pressures, the normalized difference between adiabatic wall temperature and surface temperature, $T_{ADW} - T_S / T_{ADW} - 1200$, drops below 0.10 in less than 100 seconds of burn time except in the expansion region of the nozzle. This means that surface temperatures will typically approach the adiabatic wall temperature to within 500 F unless lowered by surface reactions. Because surface reactions will involve some degree of erosion, a conservative preliminary estimation of the onset of throat erosion should be made on the basis of erosion relations presented in Fig. 45 through 47 at various free-stream concentrations of corrosive species in the combustion gas streams.

---

*In any conduction process, high resistance at the boundaries relative to the internal resistance "ears" the internal temperature profiles.

124

Figure 62. Comparison of Char Advance in a Phenolic-Refrasil Soft Throat by Two- and One-Dimensional Computer Programs
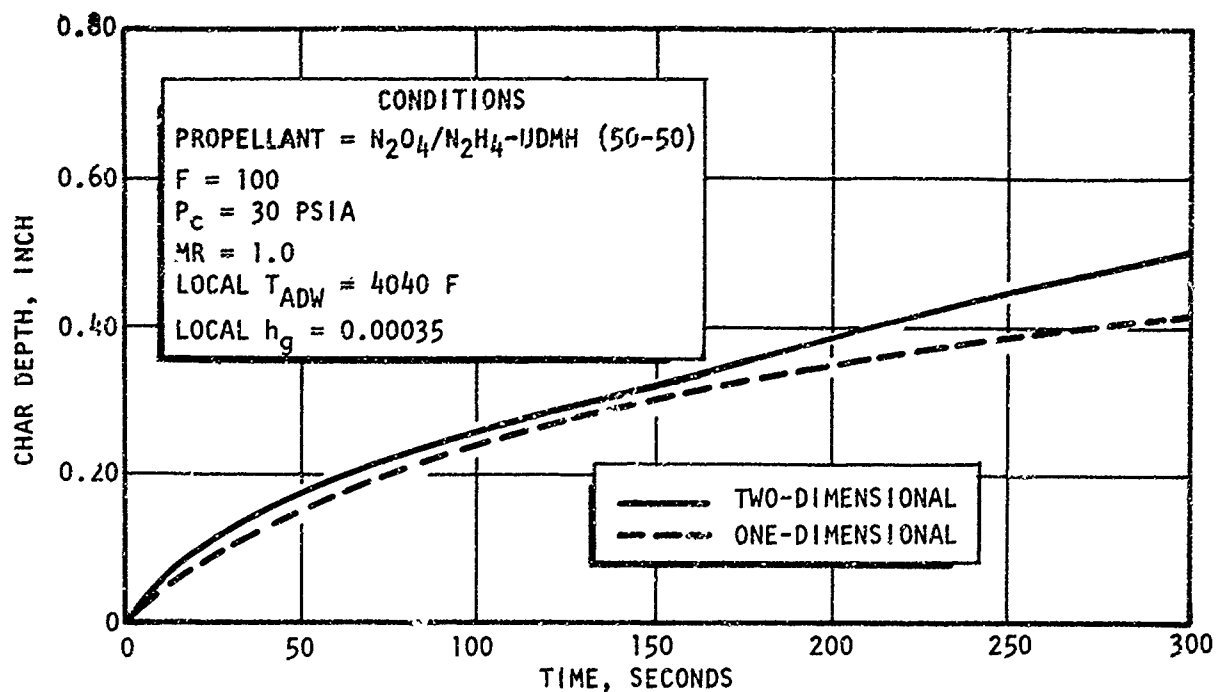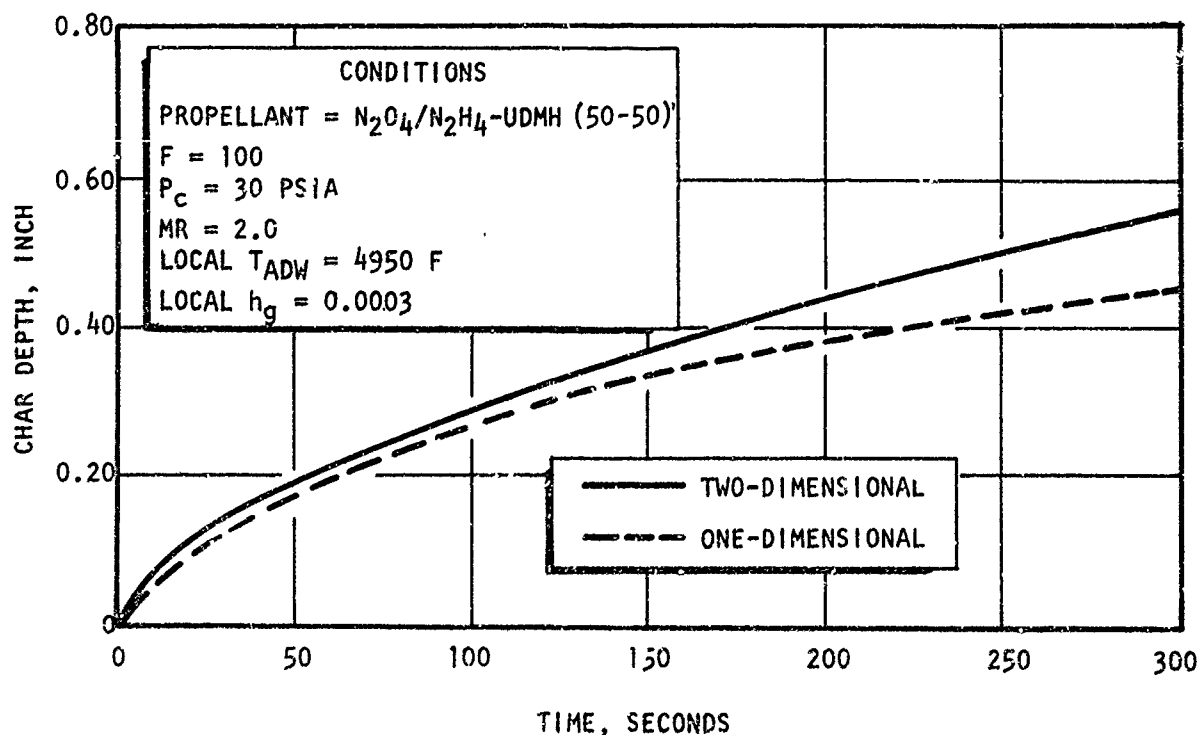

Figure 63. Comparison of Char Advance in a Phenolic-Refrasil Soft Throat by Two- and One-Dimensional Computer Programs
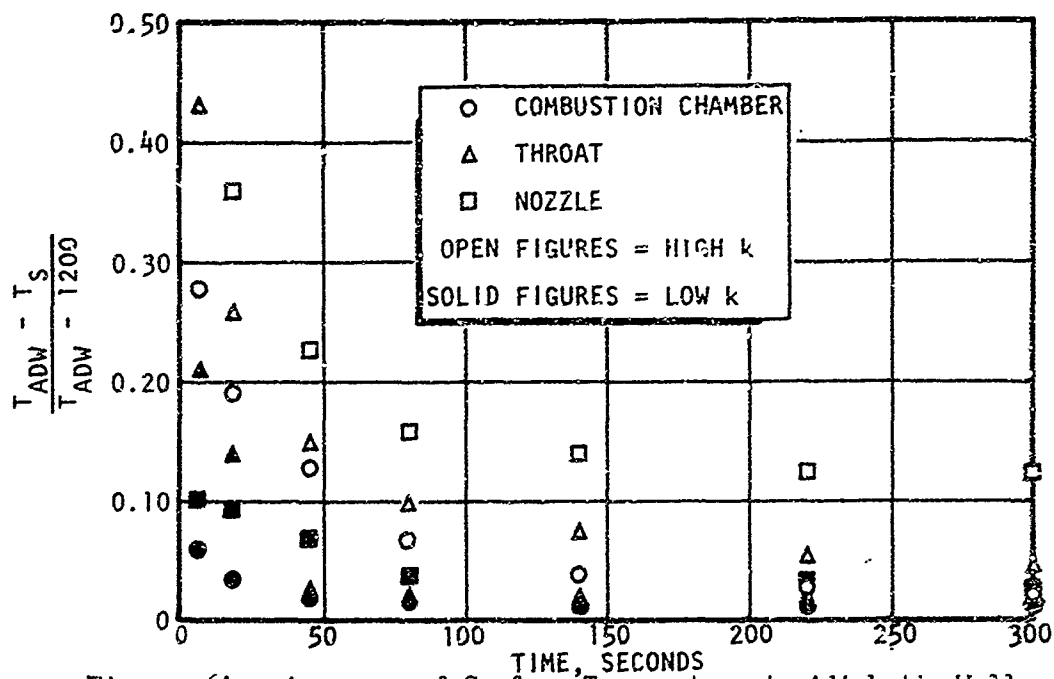
Figure 64. Approach of Surface Temperature to Adiabatic Wall
Temperature for Relatively High Chamber Pressure
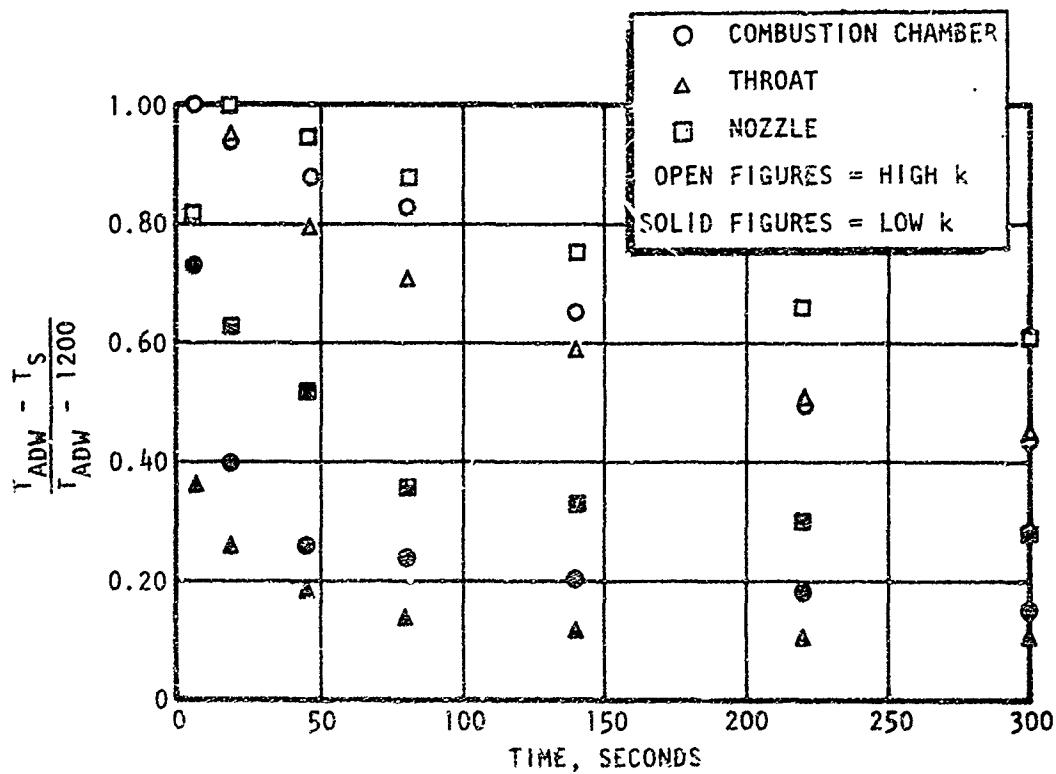
Figure 65. Approach of Surface Temperature to Adiabatic Wall
Temperature for Relatively Low Chamber Pressure

126

According to Fig. 65, the gas-side surface temperatures will be appreciably below the adiabatic wall temperature in all portions of the chamber at low chamber pressures ($<$ 50 psia). A preliminary estimation of throat erosion based upon the adiabatic wall temperature will therefore be conservative at these operating conditions.

Intermittent Duty Cycles

To examine the effects of a multiple start duty cycle, Computer Run 8 was made with the thrust chamber configuration and propellant combination of Computer Run 1 (Table 11 and Fig. 48) but with a burn schedule as shown below:

Time, seconds	Duty
0 to 200	Fire at 500-psia chamber pressure
200 to 2200	Soakback
2200 to 2250	Fire at 100-psia chamber pressure
2250 to 2550	Soakback
2550 to 2580	Fire at 500-psia chamber pressure

The computer run was terminated during the final burn period when the time limit on the IBM-360 computer was exceeded.

At the end of the first burn period, the char front (1000 F isotherm) had penetrated approximately 0.20 inch into the phenolic refrasil overwrap around the combustion chamber and approximately 0.30 inch into the overwrap in the throat region. In the nozzle region charring was complete at area ratios greater than 3.0.

At the end of the 2000-second first soakback period, the char front extended approximately 0.50 inch into the refrasil overwrap around the combustion chamber with essentially the same penetration in the throat region. In the nozzle, the wall was completely charred through for area

ratios between 2.8 and 8. In the combustion chamber, charring continued for practically the entire soakback period. The entire second burn period was required to reheat the char layer in the combustion chamber and throat regions with no additional charring occurring during this period. At the end of the second soakback period (300 second), the char front had penetrated approximately 0.58 inch into the refrasil overwrap in the combustion chamber and 0.65 inch in the throat region. Charring was still in progress at the end of the soakback period.

During the first soakback period, the additional char penetration in the combustion chamber was approximately 45 percent of the total penetration through both the inner carbon cloth and outer refrasil ablative materials which took place during the first burn period; but it was 2-1/2 times the penetration through the refrasil overwrap alone. During the first 500 seconds of soakback, the char rate in the refrasil was almost equal to that at the end of the burn period. In the throat region, the additional char penetration through the refrasil during the first soak period was approximately 70 percent of the penetration through the refrasil during the first burn period. The reason for the high additional char penetration during soakback for the conditions of Computer Run 1 is the high thermal conductivity of both the inner carbon cloth chamber liner and the ATJ-graphite throat insert. As a consequence of their high conductivities, these portions of the chamber wall attain a relatively uniform temperature close to the adiabatic wall temperature and can store a significant amount of heat. Because of the low conductivity of phenolic refrasil, it requires long soakback periods for this heat to be dissipated. The high thermal conductivity of the inner wall materials together with the low conductivity of the phenolic refrasil also produce the long heat-up period before charring resumes upon ablative-motor restart.

At the end of the first burn period, the outer skin temperature of the phenolic refrasil had risen only from 70 to 80 F in the chamber and throat regions, but had risen to 2760 F at an area ratio of 5. At the

128

end of the first soakback period, the skin temperature in the throat region had risen to 520 F, but the nozzle skin temperature had dropped to 1975 F. During the subsequent burn and soakback periods, the chamber and throat region skin temperatures were almost constant, but the nozzle temperatures fluctuated with heating load.

The results of the multiple restart computer experiment described above are specific to the engine configuration and mission cycle specified. However, they reveal the general qualitative trends to be encountered with this type of operation.

The duty cycle of the Apollo Command Module rocket engine which provided the data for evaluating the thermal conductivity of phenolic-refrasil under Task 2 of this study furnishes an example of a combined pulse mode and multiple restart operation. The portion of the duty cycle of the Apollo engine examined and the calculated char penetration through the combustion chamber walls during the periods of pulse, full burn, and soakback operation are summarized in Table 13. Charring occurs during both burn and soakback periods with the actual burn time for the entire duty cycle being 74.7 seconds. The adiabatic wall temperature and heat transfer coefficient in the Apollo engine are 4000 F and 0.00048 Btu/in.^{2}-sec-F in the combustion chamber just ahead of the nozzle throat, while the radial char thermal conductivity for the phenolic-refrasil walls (45-degree reinforcement orientation) is approximately 1.2×10^{-5} Btu/in-sec-F. From one-dimensional calculation for the actual burn time (Figs. 25 and 31), the char depth is approximately 0.23 inch, while rigorous calculation by means of 2D-ABLATE results in a char depth of 0.57 inches.

The general conclusion to be drawn from the intermittent duty cycle modes of operation examined is that the char rates are significantly different from the rates under steady firing conditions and require calculation by numerical methods which consider the specific geometrical arrangement and type of burn cycle of the system.

129

Table 13. Char Penetration Through Combustion
Chamber Wall of Apollo Nozzle

Start of Interval, Seconds	End of Interval, Seconds	Fraction Burn During Interval	Char Depth at End of Interval
0	180	0.08	0.19
180	350	0.0007	0.19
350	363.4	1.00	0.22
363.4	768	0.0725	0.41
768	1052	0.0	0.44
1052	1132	0.089	0.44
1132	1324	0.0	0.44
1324	1440	0.008	0.44
1440	1516	0.123	0.48
1516	1570	0.00	0.53
1570	1760	0.0148	0.57

SUMMARY OF DESIGN PROCEDURES

To effectively employ 2D-ABLATE and the parametric relations in this report, the following general calculational procedures are recommended:

1. Convert engine specifications into heat transfer boundary conditions. The engine specifications are propellant combination, mixture ratio, chamber pressure, thrust, expansion ratio, duty cycle, and proposed injector. From these specifications, the approximate chamber wall contours are defined before a heat transfer design begins. The necessary heat transfer boundary conditions are adiabatic wall temperature profile, heat transfer coefficient profile, and the internal radiation view factors.

    The adiabatic wall temperature is determined from the flame temperature of the propellant combination at the operating mixture ratio. Flame temperature is obtained from any available propellant performance program such as the Rocketdyne N-element program (Ref. 24).

    Local heat transfer coefficients along the chamber axis can be obtained from the graphical relations of Appendix D based upon the simplified Bartz equation (Ref. 23) using combustion gas properties from propellant performance data. Radiation view factors for the throat and nozzle regions are obtainable from graphical correlations such as those given in Appendix D.

2. Choose ablative wall materials on the basis of adiabatic wall temperature and compatability with combustion gases, carbon-cloth phenolics for high-temperature gases with minimal water content, phenolic-refrasil for low flame temperature, and water-containing combustion gases. Reinforcement orientation should be 30 degrees or more from chamber axis to prevent delamination.

131

3. From the average thermal conductivity of the ablative wall chosen,
    the adiabatic wall temperature, and gas-side heat transfer coef-
    ficient, estimate the expected char depth from the curves of
    Fig. 25 through 44 . Interpolate between curves by means of
    Eq. 3-1, 3-2, 3-5, 3-6, 3-7, and 3-8.   Extrapolate to longer
    burn times by assuming that char depth varies as the square
    root of time for long burn time. Make an initial allowance of
    50 percent more char depth for intermittent duty cycle.

4. If char depth is considered excessive, try overwrap of phenolic
    refrasil with orientation nearly parallel to chamber axis for
    low char rate. Calculate char rate in the overwrap layer from
    Eq. 3-9, starting the calculation at the time charring of
    inner wall layer is complete.

5. For chamber pressures above 30 psia and long duty cycles,
    consider hard throats: graphite for fluorinated oxidizers,
    silicon carbide for combustion gases with appreciable oxygen
    or water vapor. Estimate throat erosion from Fig. 45 through
    47 . If erosion is excessive by order of magnitude, chamber
    pressure and/or mixture ratio will have to be changed. If
    erosion is marginal, two-dimensional calculation may change
    prediction.

6. Estimate thermal penetration depth from Eq. 3-3 and Fig. 29.
    If limitations on the outer skin temperature exist, make initial
    estimation of additional overwrap required over and above char
    depth so that thermal penetration does not reach outer skin.

7. Lay out exact contours of wall segments based upon stress and
    fabrication considerations.

8. Test configuration with 2D-ABLATE. If erosion is excessive,
    chamber pressure and/or mixture ratio must be changed. Either
    bulk mixture ratio or mixture ratio near the wall (by injector
    modification) may be changed. Adjust thicknesses of inner and
    outer ablative layers from char and thermal penetration results.
    Consider outer insulation when necessary.

9. Modify adjusted thermal design from strength and fabrication standpoints.

10. Iterate with 2D-ABLATE until design is satisfactory.

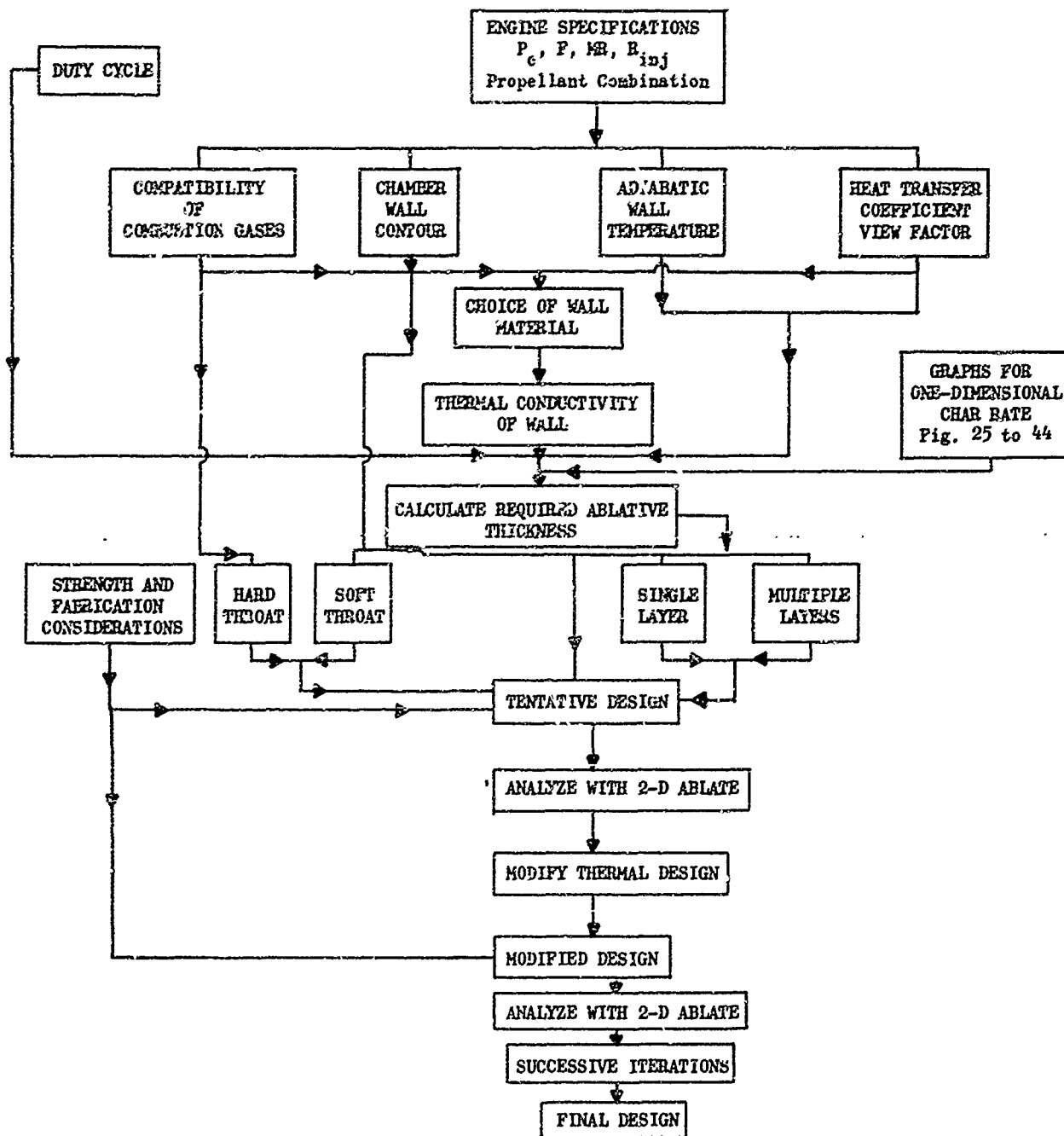A flow diagram for the design procedure is presented in Fig. 66.

Figure 66. Design Procedure for Ablative Rocket Engines

RECOMMENDATIONS FOR FUTURE EFFORTS

The main area of uncertainty in the design of ablatively protected liquid
engines is in the prediction of surface recession rates. Theoretical models
have been drawn up for surface degradation based upon three primary mechanisms:

1. Melting of the surface leading to mechanical removal of char
   through shear and/or pressure gradient

2. Chemical reaction with the combustion gas

3. Sublimation

The present 2-D program includes provisions for all these mechanisms. The
theoretical models on which the calculations are based have been shown to be
in reasonably good agreement with simple experiments. However, because all
models contain Arrhenius-type expontial terms $(e^{-\Delta E/kT})$, they are very
sensitive to c^* efficiency and to mixture ratio which determine gas
temperature. Moreover, because the local mixture ratio affects the
surface reaction (rather than the overall mixture ratio), the reported
bulk mixture ratios given in the usual engine test reports are not
necessarily an accurate measure of the ablative surface environment.
Consequently, most of the data from small engine firings are relatively
useless for checking the validity of computer program calculations.

A particularly disturbing observation concerning average surface recession
rates as usually reported (total change in cross-sectional area divided by
firing time) is the fact that "after" photographs often show scalloping
attributed to oxidizer streaking, whereas the computer program assumes
uniform recession. It is obvious that available surface recession data
can only be applied by a person thoroughly familiar with the injector,
chamber, and instrumentation employed in the test.

Several combinations of analytical and experimental investigations could
advance the state-of-the-art knowledge of surface recession. Such inves-
tigations are recommended to include the following:

1. Critical re-examination of available ablative motor test data; e.g., establish contact with the original investigators, define the additional complications in the reported test data caused by injector effects and process these runs through the 2-D program to determine whether the overall growth of the cross-sectional area can be adjusted to a uniform recession model by a simple accomodation coefficient. The restrictions upon the use of such a coefficient would be established possibly in terms of an injector spray pattern rating.

2. Other analytical attempts to describe nonuniform erosion with the help of the 2-D program.

3. Generation of additional data in critical regions using hardware specifically designed to produce a uniform mixture ratio and a well-developed flow profile throughout the ablative portion of the nozzle. Such firings would check the validity of the uniform recession under the idealized conditions assumed.

4. Variation of the wall mixture ratio in the test apparatus of 3 above through selective hole enlargement in the injector. The resultant effects on throat erosion would be measured in a few firings. The results would be compared to the predictions of previous hot-gas mixing experiments obtained at Rocketdyne and elsewhere to determine the possible variation in mixture ratio effects in an ablative chamber design.

5. Extension of the 2D-ABLATE to cover heat transfer and erosion mechanisms heretofore not included; e.g., effect of solid particles in the gas stream, radiation from gas to wall, variation of the gas-side heat transfer coefficient with time, boundary layer cooling.

6. Extension of the 2D-ABLATE to include calculation of view factor; thermal stress analysis; convective heating, charring and erosion at any boundary with a more flexible mesh procedure to handle alternative configurations.

It should be noted that all recommended tasks are independent of each other; i.e., any task or portion of a task may be executed with little effect on the information to be obtained in the other tasks.

136

A_i, B_i = areas of thrust chamber inside subsurfaces, i=1, ..., N

B = input constant characteristics of the blocking phenomenon

$C(T)$, c_p = specific heat of wall material

$C_{p\infty}$ = free stream specific heat at constant pressure

$F_r(T)$ = fraction of mass converted to gas or fraction remaining as solid due to gas generation reaction r in charring material

$F_{i,k}$, $G_{i,k}$, and $H_{i,k}$ = view factors from inside subsurface i to subsurface k

$f(x,\tau)$ = radial position of receding hot gas boundary

G_x, G_y = axial and radial components of generated gas mass flux in charring material

G_ξ, G_η = components of generated gas mass flux in minor and major directions of conductivity for anisotropic charring material

$G_j(x,\tau)$ = mass flux of gaseous species j at exposed inside surface

$H_j(T)$ = enthalpy of gaseous species j at exposed inside surface

$H(T)$ = enthalpy of gases generated in charring material

ΔH_r = heat of decomposition mode r at eroding wall surface

$h(x,\tau,T)$, h_g = heat transfer coefficient

$\bar{h}_{conv}(x)$ = basic convective heat transfer coefficient prior to modification to account for blocking

$K(T)$, k = thermal conductivity of wall material

K_n = conductivity in the normal direction at the surface of an anisotropic material (see Eq. 23)

K_x, K_y, K_{xy} = conductivities in the axial, radial, and "mixed" directions for an anisotropic material (see Eq. 22)

K_ξ, K_η = conductivities in the minor and major direction for an anisotropic wall material

n, s	= outward normal and counterclockwise tangential directions
n_j	= known constant for gaseous species j at exposed inside surface (see Eq. 9)
Q_r	= reference heat of reaction for gas-generation reaction r in charring material
$q(x,\tau)$	= heat flux
$R_G(x,y,\tau)$	= ratio, $\bar{K}_x G_x / K_y G_y$
$T(x,y,\tau)$	= temperature of wall material
$T_{aw}(x)$	= adiabatic wall temperature
$T_{max}(x,y,\tau)$	= maximum value of T achieved by time τ at point (x,y) in wall material
T_{py}	= minimum pyrolysis temperature of charring material
v	= normal velocity of gas or liquid at exposed inside surface
x,y	= axial and radial coordinates
X	= mole fraction
$\Delta x, \Delta y$	= axial and radial distance increments
$\beta_f(x)$	= radiation view factor from wall surface to outside environment
δ	= spatial difference operator
ϵ	= emissivity of material surface
$\rho(T)$	= spatial density
η, ξ	= major and minor directions of conductivity for an anisotropic material
σ	= Stefan-Boltzmann constant
τ	= time
$\Delta\tau$	= time increment used for time step calculations
θ	= angular displacement of ξ and η directions from x and y directions, respectively, for an anisotropic material
U	= overall heat transfer coefficient
Pr	= Prandtl number

Subscripts

A, B, C, D = points adjacent to interior point 0 in finite difference analog of energy equation

conv = due to convection

eff = effective

env = due to environmental heating

0 = interior point (x_i, y_j)

r = index ranging over erosion modes at the exposed inside surface or over gas generation reactions in a charring material

rad = due to radiation

rerad = due to radiative exchange at the exposed inside surface

v = virgin

c = char

Units

When not otherwise specified, the following units apply:

h_g = Btu/in.^{2}-sec-F

k = Btu/in.-sec-F

ρC_p = Btu/in.^{3}-F

REFERENCES

1. Rivers, W. J., R. Van Wyk, J. D. Seader, H. A. Friedman, and H. N. Chu: Final Report. Effect of Rocket Engine Combustion on Chamber Materials. Part I: One-Dimensional Computer Program, Rocketdyne Report R-6050-1, AFRPL-TR-65-13, Edwards, California, Contract AF04(611)-9714, January, 1965.

2. Friedman, H. A., S. P. Persselin, B. L. McFarland and J. D. Seader: Final Report, Effect of Rocket Engine Combustion on Chamber Materials, Part II: Two-Dimensional Computer Program, Rocketdyne Report R-6050-2, AFRPL-TR-65-176, Edwards, California, Contract AF04(611)-9714, September 1965 (DDC No. AD-473111).

3. Van Wyk, R., Operating Instructions for the Final Version of the One-Dimensional Ablation Program, Applied Mathematics and Mechanics Unit Memorandum AMMM 65-4, Rocketdyne, a Division of North American Aviation, Inc., Canoga Park, California, 20 August 1965.

4. Friedman, H. A., Operating Instruction for the Fortran IV Ablation Program, 2D-ABLATE, Rocketdyne Research Memorandum RM1212-351, Rocketdyne, A Division of North American Aviation, Inc., Canoga Park, California, 22 February 1966.

5. Peaceman, D. W. and H. H. Rachford, Jr.: "The Numerical Solution of Parabolic and Elliptic Differential Equations," J. Soc. Ind. Appl. Math., 3, pages 28-41, 1955.

6. Desmon, L. G. and G. B. Avis: CYLHEAT Handbook - Vol. I. Transient Body Temperature Response Curves for Hollow Cylinders with Heated Interior and Insulated Exterior, Allegany Ballistics Lab. Report No. ABL/X-123, July 1964.

7. R-15107-2: Volume 2 Final Report, Qualification Test Report for the Apollo Command Module Rocket Engine and Nozzle Extension, Rocketdyne Spacecraft Engine Division, Contract NAS 9-150, February 1966.

8. Pesler, L. W. and H. T. Iida: IBM 7094 Two-Dimensional Transient Heat Conduction Program, SID64-1305, NAA Space and Information Systems Division, Downey, California, 9 May 1964.

9. Hottel, H., "Radiation Heat Transmission," Chapter 4 in Heat Transmission, ed. by W. H. McAdams, 3rd ed., McGraw-Hill, N. Y., 1954.

141

10. deSoto, S., Thermal Radiation, Lecture 6 of Advanced Heat Transfer Seminar, Rocketdyne, February 1965.

11. Harmon, T. J.: "Apollo SE-8 Test Report Rocket Engine Assembly Unit No. 8804," Interim Report STR 4383-6692, Rocketdyne, a Division of North American Aviation, Inc., Canoga Park, California, 17 May 1965.

12. ML-TDR-64-204: Design Data for Materials Employed in Thermal Protective Systems on Advanced Aerospace Vehicles, AF Materials Laboratory, Wright-Patterson AFB, Ohio, 1965.

13. TR-60-924: Thermal Properties of Thirteen Solid Materials to 5000 F for Their Destruction Temperatures, Directorate of Materials and Processes, Wright-Patterson AFB, Ohio, 1962.

14. Ladacki, M., J. Hamilton and S. Cohz: "Heat of Pyrolysis of Resin in Silica — Phenolic Ablator," AIAA Journal, 4, 10, 1798-1802, October 1966.

15. R-15106: Thermophysical Property Measurements of the Nozzle Extension Material for the Apollo Command Module Reaction Control Engines, Rocketdyne, a Division of North American Aviation, Inc., Canoga Park, California.

16. R-6025-2: Chamber Technology for Space Storeable Propellants — Task II, Interim Report, Volume 2, Contract NAS7-304, Rocketdyne, a Division of North American Aviation, Inc., Canoga Park, California, October 1965.

17. WADC-TR58-476: Thermophysical Properties of Solid Material, Volume 1, Elements, ASTIA AD247193, August 1960.

18. EN-S-0059: Scale Model Heat Transfer Tests for the Nerva Nozzle, CY 1963, Aerojet General Corporation, March 1964.

19. Rogers, J. D., and A. Soesonke: Graphite-Hydrogen-Methane Kinetics Above 1500°," LAMS-2896, 26 May 1963.

20. Jones, W. H. and Delaney, L. J., An Analysis of the Materials Problems for Throat Inserts of High-Energy Solid Propellant Rockets, IDA/RESD TR 62-19, ASTIA 404662, October 1962.

21. ASD-TDR-63-737: Chemical Reactions Between Plastic Composite Materials and Propellant Exhaust Products, Vol. 1, AF Materials Laboratory, Wright-Patterson AFB, Ohio, 1963.

22. U561-66-12: Chamber Technology for Space Storable Propellants, Sixth Quarterly Report, NAS 7-304, January 1966

23. Bartz, D. R.: "A Simple Equation for Rapid Estimation of Rocket Nozzle Convective Heat Transfer Coefficients," Jet Propulsion, 21, No. 1, 1957.

24. Thompson, R. J., Jr.: "High-Temperature Thermodynamic and Theoretical Performance Evaluation of Rocket Propellants," The Chemistry of Propellants, Pergamon Press, 1966, 25-120.

25. ASD-TDR-63-737: Thermal Erosion of Ablative Materials, Part II, AF Materials Laboratory, Wright Patterson AFB, Ohio, 1965.

CALCULATION OF VIEW FACTORS BY THE DISK METHOD

To calculate view factors $F_{i,j}$ from the inside surface areas A_i to A_j, $i, j = 1, \ldots, N$, by the disk method, we subdivide the chamber interior into N conical disks (e.g., Fig. A-1 where N is taken to be 10) with $N + 1$ circular bounding base areas A_{α_i}, $i = 1, \ldots, N + 1$. Under the assumption of no occultation or shading, the view factors F_{α_i, α_j} from A_{α_i} to A_{α_j}, $i, j = 1, \ldots, N + 1$, are given by the following relation (Ref. 10):

$$F_{\alpha_i, \alpha_j} = \left[z_{ij} - \left(z_{ij}^2 - 4 A_{\alpha_i} A_{\alpha_j} \right)^{1/2} \right] / 2 A_{\alpha_i}, \qquad (A-1)$$

where

$$z_{ij} = A_{\alpha_i} + A_{\alpha_j} + \left(x_{\alpha_j} - x_{\alpha_i} \right)^2 \qquad (A-2)$$

and x_{α_i} is the axial position of the plane α_i. From Eq. A-1 and A-2, it can be seen that $F_{\alpha_i, \alpha_i} = 1$ for all values of i. In practice, we would only use Eq. A-1 for $i \leq j$. For F_{α_j, α_i} we would use

$$F_{\alpha_j, \alpha_i} = A_{\alpha_i} F_{\alpha_i, \alpha_j} / A_{\alpha_j}.$$

For the checkout case described earlier in this report, the inclination of the inside surface from the horizontal did not exceed 20 degrees so that the assumption of no occultation or shading (required for the use of Eq. A-1) is reasonable. Using Eq. A-1, we can calculate the desired array $F_{i,j}$, $i, j = 1, \ldots, N$, as follows:

$$F_{i,i} = 1 - \left(A_{\alpha_i} + A_{\alpha_{i+1}} - 2 A_{\alpha_i} F_{\alpha_i, \alpha_{i+1}} \right) / A_i, \quad i = 1, \ldots, N, \qquad (A-3)$$
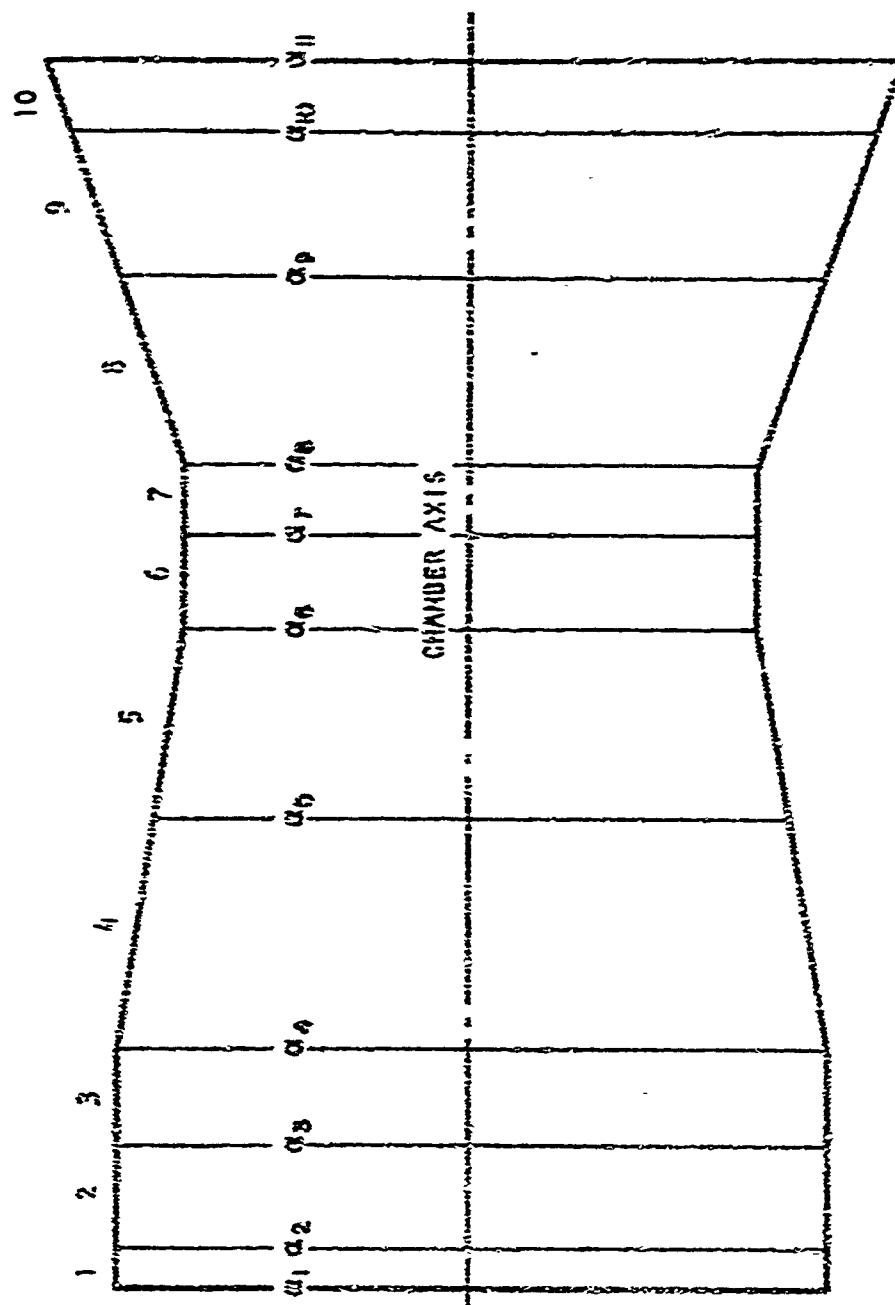
Figure A-1. Subdivision of Chamber Into Conical Disks for Calculation of View Factors

$$P_{i,i+k} = \left[A_{\alpha_{i+1}} \left(P_{\alpha_{i+1},\alpha_{i+k}} - P_{\alpha_{i+1},\alpha_{i+k+1}} \right) - \right.$$

$$\left. A_{\alpha_i} \left(P_{\alpha_i,\alpha_{i+k}} - P_{\alpha_i,\alpha_{i+k+1}} \right) \right] / A_i, \tag{A-4}$$

$$P_{i+k,i} = A_i P_{i,i+k} / A_{i+k}, \quad i = 1,\dots, N-1; \; k = 1,\dots, N-i.$$

The derivation of Eq. A-3 and A-4 requires use of an interim array of view factors from the inside surface areas A_i to the base areas A_{α_j}, $i = 1,\dots, N$, $j = 1,\dots N - 1$, given by the following:

$$F_{i,\alpha_j} = \left(A_{\alpha_{i+1}} P_{\alpha_{i+1},\alpha_j} - A_{\alpha_i} P_{\alpha_i,\alpha_j} \right) / A_i \tag{A-5}$$

The procedure will be indicated for several values of i and k. The rest is done similarly. To get $P_{1,1}$, we start by writing the identities relating surfaces within the first disk:

$$P_{1,1} + P_{1,\alpha_1} + F_{1,\alpha_2} = 1, \tag{A-6}$$

$$F_{\alpha_1,1} + F_{\alpha_1,\alpha_2} = 1, \tag{A-7}$$

$$P_{\alpha_2,1} + F_{\alpha_2,\alpha_1} = 1. \tag{A-8}$$

From Eq. A-7 and A-8 and the identity

$$A_r P_{r,s} = A_s F_{s,r}, \tag{A-9}$$

we obtain the following relationships:

$$P_{1,\alpha_1} = A_{\alpha_1} \left(1 - F_{\alpha_1,\alpha_2} \right) / A_1, \tag{A-10}$$

$$F_{1,\alpha_2} = A_{\alpha_2} \left(1 - F_{\alpha_2,\alpha_1} \right) / A_1 = \left(A_{\alpha_2} - A_{\alpha_1} P_{\alpha_1,\alpha_2} \right) / A_1. \tag{A-11}$$

Substitution of P_{1,α_1} and P_{1,α_2} in Eq. A-6 and rearranging will yield Eq. A-3 for the case of $i = 1$.

Similarly, to get $F_{1,2}$ we start by writing one identity based upon analysis of the second disk:

$$F_{\alpha_3,\alpha_2} + F_{\alpha_3,2} = 1 \tag{A-12}$$

as well as two others obtained by treating the first two disks as a single disk (by removing side A_{α_2}):

$$F_{1,\alpha_1} + F_{1,1} + F_{1,2} + F_{1,\alpha_3} = 1, \tag{A-13}$$

$$F_{\alpha_3,\alpha_1} + F_{\alpha_3,1} + F_{\alpha_3,2} = 1. \tag{A-14}$$

By combining Eq. A-6 and A-11 with A-13, and Eq. A-12 with A-14, we obtain the following expressions:

$$F_{1,2} + F_{1,\alpha_3} = (A_{\alpha_2} - A_{\alpha_1} F_{\alpha_1,\alpha_2}) / A_1, \tag{A-15}$$

$$F_{\alpha_3,\alpha_1} + F_{\alpha_3,1} = F_{\alpha_3,\alpha_2}. \tag{A-16}$$

From Eq. A-16 and A-9 we get

$$F_{1,\alpha_3} = (A_{\alpha_2} F_{\alpha_2,\alpha_3} - A_{\alpha_1} F_{\alpha_1,\alpha_3}) / A_1, \tag{A-17}$$

and finally, from Eq. A-15 and A-17, we obtain

$$F_{1,2} = \left[A_{\alpha_2} (1 - F_{\alpha_2,\alpha_3}) - A_{\alpha_1} (F_{\alpha_1,\alpha_2} - F_{\alpha_1,\alpha_3}) \right] / A_1. \tag{A-18}$$

Eq. A-18 is a special case of Eq. A-4 for $i = 1$ and $k = 1$.

In a similar fashion, we can derive the following:

$$F_{1,3} + F_{1,\alpha_4} = (A_{\alpha_2} F_{\alpha_2,\alpha_3} - A_{\alpha_1} F_{\alpha_1,\alpha_3}) / A_1, \tag{A-19}$$

$$F_{\alpha_4,\alpha_1} + F_{\alpha_4,1} = F_{\alpha_4,\alpha_2}, \tag{A-20}$$

148

and

$$F_{1,\alpha_4} = (A_{\alpha_2} \, F_{\alpha_2,\alpha_4} - A_{\alpha_1} \, F_{\alpha_1,\alpha_4}) / A_1, \qquad\qquad \text{(A-21)}$$

and, finally, the following special case of Eq. A-4 for $i = 1$ and $k = 2$:

$$F_{1,3} = \left[A_{\alpha_2} \, (F_{\alpha_2,\alpha_3} - F_{\alpha_2,\alpha_4}) - A_{\alpha_1} \, (F_{\alpha_1,\alpha_3} - F_{\alpha_1,\alpha_4}) \right] / A_1. \quad \text{(A-22)}$$

The remainder of the $F_{i,j}$ can be obtained in a similar fashion (or by induction).

APPENDIX B

DEVELOPMENT OF THE ANISOTROPIC ENERGY EQUATION

To derive the form of the anisotropic energy equation as given by Eq. 21 and the expression given by Eq. 23 for the normally directed conductivity at a boundary of an anisotropic material, a transformation through a rotation θ is required from gradients in the x and y directions to gradients in the ξ and η directions and vice versa. Geometrical considerations yield the following expressions:

$$\frac{\partial}{\partial \xi} = \cos\theta \frac{\partial}{\partial x} + \sin\theta \frac{\partial}{\partial y}, \tag{B-1}$$

$$\frac{\partial}{\partial \eta} = -\sin\theta \frac{\partial}{\partial x} + \cos\theta \frac{\partial}{\partial y}, \tag{B-2}$$

$$\frac{\partial}{\partial x} = \cos\theta \frac{\partial}{\partial \xi} - \sin\theta \frac{\partial}{\partial \eta}, \tag{B-3}$$

$$\frac{\partial}{\partial y} = \sin\theta \frac{\partial}{\partial \xi} + \cos\theta \frac{\partial}{\partial \eta}. \tag{B-4}$$

If we further stipulate that the two coordinate systems possess a common origin, then, from Eq. B-1 through B-4, we can also write

$$x = \xi \cos\theta - \eta \sin\theta, \tag{B-5}$$

$$y = \xi \sin\theta + \eta \cos\theta. \tag{B-6}$$

To derive Eq. 21, we start with the energy equation expressed in the coordinates ξ and η and then transform it to x and y coordinates using Eq. B-1 through B-6. This would be straightforward were it not for the need to include the radial effect in the ξ and η system, which makes it more difficult to get started. If x and y were cartesian coordinates rather than cylindrical, the energy equation would take the following

form in the ξ and τ system (where for convenience of notation we omit the subscript "eff" on C):

$$\rho C \frac{\partial T}{\partial \tau} = \frac{\partial}{\partial \xi}\left(K_\xi \frac{\partial T}{\partial \xi}\right) + \frac{\partial}{\partial \eta}\left(K_\eta \frac{\partial T}{\partial \eta}\right) - \frac{dH}{dT}\left(G_\xi \frac{\partial T}{\partial \xi} + G_\eta \frac{\partial T}{\partial \eta}\right) \tag{B-7}$$

A strictly geometric argument entailing Eq. B-6 above would show that the radial effect can be introduced into Eq. B-7 by adding the following term to the right hand side:

$$\frac{K_y}{\xi \sin\theta + \eta \cos\theta}\left(\sin\theta \frac{\partial T}{\partial \xi} + \cos\theta \frac{\partial T}{\partial \eta}\right), \tag{B-8}$$

where the expression for K_y, the radial component of conductivity, is to be determined as a function of K_ξ, K_η, and θ during the transformation of the rest of the equation to x and y coordinates. Thus, we transform Eq. B-7, augmented by the radial term B-8, to x-y coordinates by substituting from Eq. B-1 through B-6, as follows:

$$\rho C \frac{\partial T}{\partial \tau} = \left(\cos\theta \frac{\partial}{\partial x} + \sin\theta \frac{\partial}{\partial y}\right)\left[K_\xi \left(\cos\theta \frac{\partial T}{\partial x} + \sin\theta \frac{\partial T}{\partial y}\right)\right] +$$

$$\left(-\sin\theta \frac{\partial}{\partial x} + \cos\theta \frac{\partial}{\partial y}\right)\left[K_\eta \left(-\sin\theta \frac{\partial T}{\partial x} + \cos\theta \frac{\partial T}{\partial y}\right)\right] + \frac{K_y}{y} \frac{\partial T}{\partial y} -$$

$$\frac{dH}{dT}\left[G_\xi \left(\cos\theta \frac{\partial T}{\partial x} + \sin\theta \frac{\partial T}{\partial y}\right) + G_\eta \left(-\sin\theta \frac{\partial T}{\partial x} + \cos\theta \frac{\partial T}{\partial y}\right)\right]$$

$$= \frac{\partial}{\partial x}\left[(K_\xi \cos^2\theta + K_\eta \sin^2\theta) \frac{\partial T}{\partial x}\right] + \frac{\partial}{\partial y}\left[(K_\xi \sin^2\theta + K_\eta \cos^2\theta) \frac{\partial T}{\partial y}\right] +$$

$$\frac{K_y}{y} \frac{\partial T}{\partial y} - \frac{dH}{dT}\left[(G_\xi \cos\theta - G_\eta \sin\theta) \frac{\partial T}{\partial x} + (G_\xi \sin\theta + G_\eta \cos\theta) \frac{\partial T}{\partial y}\right] +$$

$$\frac{\partial}{\partial y}\left[(K_\xi - K_\eta) \sin\theta \cos\theta \frac{\partial T}{\partial x}\right] + \frac{\partial}{\partial x}\left[(K_\xi - K_\eta) \sin\theta \cos\theta \frac{\partial T}{\partial y}\right]$$

$$= \frac{\partial}{\partial x}\left(K_x \frac{\partial T}{\partial x}\right) + \frac{1}{y} \frac{\partial}{\partial y}\left(y K_y \frac{\partial T}{\partial y}\right) - \frac{dH}{dT}\left(G_x \frac{\partial T}{\partial x} + G_y \frac{\partial T}{\partial y}\right) +$$

$$2K_{xy} \frac{\partial^2 T}{\partial x \partial y} + 2 \frac{dK_{xy}}{dT} \frac{\partial T}{\partial x} \frac{\partial T}{\partial y}, \tag{B-9}$$

and we have Eq. 21, where K_x, K_y. and K_{xy} are defined as in Eq. 22 and where

$$G_x = G_\xi \cos\theta - G_\eta \sin\theta,$$

$$G_y = G_\xi \sin\theta + G_\eta \cos\theta. \tag{B-10}$$

We derive Eq. 23 for the normal conductivity K_n by transforming from K_ξ and K_η to the outward normal direction just as we did to the x and y directions; i.e., with squares of direction cosines as in Eq. 22 (we note that $\cos(\varphi + \pi/2) = -\sin\varphi$ for any angle φ), where the direction angles $\theta - \alpha + \frac{\pi}{2}$ and $\theta - \alpha + \pi$ are indicated in Fig. B-1.

Thus we can immediately write the following:

$$
\begin{aligned}
K_n &= K_\xi \cos^2\left(\theta - \alpha + \frac{\pi}{2}\right) + K_\eta \cos^2(\theta - \alpha + \pi) \\
&= K_\xi \left(\sin^2\theta \cos^2\alpha - 2\sin\theta \cos\theta \sin\alpha \cos\alpha + \cos^2\theta \sin^2\alpha\right) + \\
&\quad K_\eta \left(\cos^2\theta \cos^2\alpha + 2\sin\theta \cos\theta \sin\alpha \cos\alpha + \sin^2\theta \sin^2\alpha\right) \\
&= K_x \sin^2\alpha + K_y \cos^2\alpha - 2 K_{xy} \sin\alpha \cos\alpha \\
&= \left[\left(\frac{\partial f}{\partial x}\right)^2 K_x + K_y - 2 \frac{\partial f}{\partial x} K_{xy}\right] \Big/ \left[1 + \left(\frac{\partial f}{\partial x}\right)^2\right]. \tag{B-11}
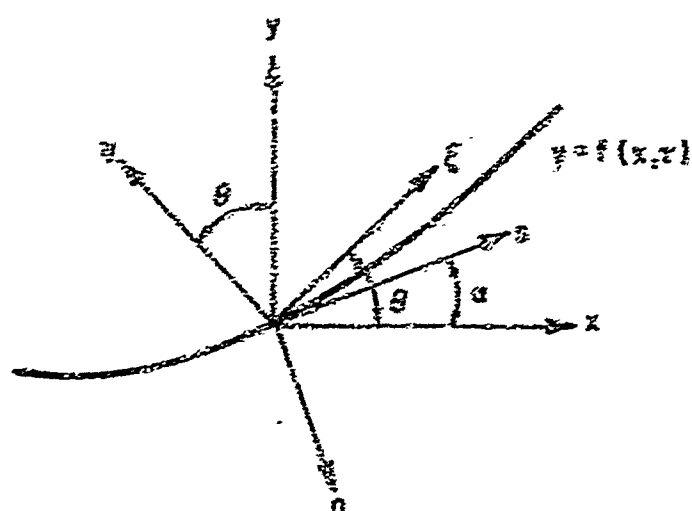\end{aligned}
$$

Figure B-1   Directions and Angles Required to Obtain K_n at a
Boundary or Interface $y = f(x, \tau)$

FINITE DIFFERENCE ANALOGS OF $\dfrac{\partial^2 T}{\partial x \partial y}$

Several finite difference analogs of the mixed temperature derivative, $\partial^2 T/\partial x \partial y$, were expressed in Eq. 25 through 30, varying from first to second order accurate depending upon the geometry. In the derivations below, the mixed difference $\delta^2_{xy} T_0$ at a regular point 0 (see Fig. 8 for labeling of the points) given by Eq. 26 is obtained from Taylor series expressed about the point 0 for the temperatures at the points E, F, G, and H. On the other hand, the remaining analogs, given by Eq. 27 through 30, were derived from Taylor series for the temperature gradients at the points A, B, C, and D. The latter approach proved to be more applicable to the mesh-boundary configurations employed in the 2D-ABLATE program, and thus Eq. 26 was not used in the program except through chance when Eq. 27 or 28 happened to reduce to Eq. 25 (which is a special case of Eq. 26).

To derive Eq. 26, we express the temperatures at the points E, F, G, and H (Fig. 9a) in Taylor series about a regular point 0, explicitly including terms up through fourth order. Only the expression for T_E will be exhibited, as follows, the remainder being easily expressed similarly (the subscripts on T refer to partial derivatives at the point 0):

$$T_E = T_0 + \Delta x_A T_{x,0} + \Delta y_B T_{y,0} + \frac{\Delta x_A^2}{2} T_{xx,0} + \Delta x_A \Delta y_B T_{xy,0} + \frac{\Delta y_B^2}{2} T_{yy,0} +$$

$$\frac{\Delta x_A^3}{6} T_{xxx,0} + \frac{\Delta x_A^2}{2} \Delta y_B T_{xxy,0} + \Delta x_A \frac{\Delta y_B^2}{2} T_{xyy,0} + \frac{\Delta y_B^3}{6} T_{yyy,0} +$$

$$\frac{\Delta x_A^4}{24} T_{xxxx,0} + \frac{\Delta x_A^3}{6} \Delta y_B T_{xxxy,0} + \frac{\Delta x_A^2}{2} \frac{\Delta y_B^2}{2} T_{xxyy,0} + \Delta x_A \frac{\Delta y_B^3}{6} T_{xyyy,0} +$$

$$\frac{\Delta y_B^4}{24} T_{yyyy,0} + \cdots \tag{C-1}$$

Combining T_E, T_F, T_G, and T_H, we obtain

$$T_E - T_F + T_G - T_H = (\Delta x_A + \Delta x_C)(\Delta y_B + \Delta y_D)\left[T_{xy,0} + \frac{\Delta x_A - \Delta x_C}{2} T_{xxy,0} + \right.$$

$$\frac{\Delta y_B - \Delta y_D}{2} T_{xyy,0} + \frac{\Delta x_A^2 - \Delta x_A \Delta x_C + \Delta x_C^2}{6} T_{xxxy,0} + \quad\quad\quad (C-2)$$

$$\frac{\Delta x_A - \Delta x_C}{2} \frac{\Delta y_B - \Delta y_D}{2} T_{xxyy,0} + \frac{\Delta y_B^2 - \Delta y_B \Delta y_D + \Delta y_D^2}{6} T_{xyyy,0} + \ldots \left.\right]$$

or

$$\frac{T_E - T_F + T_G - T_H}{(\Delta x_A + \Delta x_C)(\Delta y_B + \Delta y_D)} = T_{xy,0} + 0\,(\Delta x_A - \Delta x_C) + 0\,(\Delta y_B - \Delta y_D) +$$

$$0\,(\Delta x_A^2 - \Delta x_A \Delta x_C + \Delta x_C^2) + 0\left[(\Delta x_A - \Delta x_C)(\Delta y_B - \Delta y_D)\right] +$$

$$0\,(\Delta y_B^2 - \Delta y_B \Delta y_D + \Delta y_D^2) \quad\quad\quad\quad\quad (C-3)$$

The left side of Eq. C-3 is the mixed difference analog, $\delta_{xy}^2 T_0$, as expressed by Eq. 26, and the right side indicates how closely the difference analog approximates the mixed derivative, $T_{xy,0}$. If $\Delta x_A \gg \Delta x_C$, $\Delta x_A \ll \Delta x_C$, $\Delta y_B \gg \Delta y_D$, or $\Delta y_B \ll \Delta y_D$, Eq. C-3 is essentially first order accurate. If, on the other hand, $\Delta x_A = \Delta x_C = \Delta x$ and $\Delta y_B = \Delta y_D = \Delta y$, Eq. C-3 reduces to Eq. 25 and the truncation error reduces to $0\,(\Delta x^2) + 0\,(\Delta y^2)$.

The derivation of Eq. 27 and 28 is considerably simpler, requiring fewer terms of the Taylor series and yet yields, in general, a more accurate formula. Here we express temperature gradients instead of temperatures at the points A, B, C, and D in Taylor series about the point 0, as follows:

$$T_{y,A} = T_{y,0} + \Delta x_A\, T_{xy,0} + \frac{\Delta x_A^2}{2} T_{xxy,0} + \frac{\Delta x_A^3}{6} T_{xxxy,0} + \ldots \quad (C-4)$$

$$T_{y,C} = T_{y,0} - \Delta x_C T_{xy,0} + \frac{\Delta x_C^2}{2} T_{xxy,0} - \frac{\Delta x_C^3}{6} T_{xxxy,0} + \dots \quad (C-5)$$

$$T_{y,B} = T_{y,0} + \Delta y_B T_{xy,0} + \frac{\Delta y_B^2}{2} T_{xyy,0} + \frac{\Delta y_B^3}{6} T_{xyyy,0} + \dots \quad (C-6)$$

$$T_{y,D} = T_{y,0} - \Delta y_D T_{xy,0} + \frac{\Delta y_D^2}{2} T_{xyy,0} - \frac{\Delta y_D^3}{6} T_{xyyy,0} + \dots \quad (C-7)$$

From Eq. C-4 and C-5, we obtain

$$\frac{\Delta x_C^2 \, T_{y,A} - (\Delta x_C^2 - \Delta x_A^2) \, T_{y,0} - \Delta x_A^2 \, T_{y,C}}{\Delta x_A \, \Delta x_C \, (\Delta x_A + \Delta x_C)} = T_{xy,0} +$$

$$\frac{\Delta x_A \, \Delta x_C}{6} T_{xxxy,0} + \dots = T_{xy,0} + 0 \left(\Delta x_A \, \Delta x_C \right) \quad (C-8)$$

and, similarly, from C-6 and C-7, we have

$$\frac{\Delta y_D^2 \, T_{x,B} - (\Delta y_D^2 - \Delta y_B^2) \, T_{x,0} - \Delta y_B^2 \, T_{x,D}}{\Delta y_B \, \Delta y_D \, (\Delta y_B + \Delta y_D)} = T_{xy,0} +$$

$$0 \left(\Delta y_B \, \Delta y_D \right) \quad (C-9)$$

Eq. C-8 is applicable to the 2D-ABLATE program, as discussed between Eq. 28 and 29 in the text, whenever both the points A and C are regular and, similarly, Eq. C-9 is applicable when points B and D are regular. To obtain Eq. 27 and 28 from Eq. C-8 and C-9, respectively, we replace $T_{y,0}$, $T_{y,A}$, $T_{y,C}$, $T_{x,0}$, $T_{x,B}$, and $T_{x,D}$ in Eq. C-8 and C-9 by second order accurate centered finite difference analogs. In doing this, however, examination of the error term involved in each would seem to indicate that Eq. 28, although second order accurate in the x-direction, is in all cases only first order accurate in the y-direction, and that Eq. 29 similarly, is only first order accurate in the x-direction. That this cannot be true and, indeed, leads to contradiction is demonstrated by analyzing the case in which all the points diagonally adjacent to the point 0 are regular (Fig. 9a). In that case, Eq. 28 and 29 reduce to the same difference equation. But then the assertion above concerning the error would lead

to the conclusion that the resulting difference equation both is and is
not second order accurate, which is absurd. As a matter of fact, by
deriving Eq. 28 or 29 for the case of Fig. 9a from Taylor series for the
temperatures at the points A, B, C, D, E. F, G, and H, the error can be
shown to be $0 \left(\Delta x_A \Delta x_C \right) + 0 \left(\Delta y_B \Delta y_D \right)$. This is an explicit demon-
stration of second order accuracy and proves that Eq. 28 and 29 are more
accurate than Eq. 26. When the points diagonally adjacent to the point
0 are not regular (in which case, Eq. 26 would not even be applicable),
it can be shown that Eq. 28 is between first and second order accurate
in the y-direction (in a sense similar to Eq. C-3) and Eq. 29 is the same
in the x-direction. For the point configuration depicted in Fig. C-1,
for example, the error in Eq. 28 is $0 \left(\Delta x_A \Delta x_C \right) + 0 \left(\Delta y_B - \Delta y_{F_2} \right) +$
$0 \left(\Delta y_B \Delta y_D \right)$, which yields essentially first order accuracy in the y-
direction for $\Delta y_{F_2} \ll \Delta y_B$ and second order accuracy for $\Delta y_{F_2} \cong \Delta y_B$.

As stated above, either Eq. 28 or 29 does not apply when one or more of
the points A, B, C, and D is irregular (Fig. 9r). If, for example,
point C is irregular we would obtain the following expression (instead
of Eq. C-8 above) directly from Eq. C-4:

$$\frac{T_{y,A} - T_{y,0}}{\Delta x_A} = T_{xy,0} + 0 \left(\Delta x_A \right) \tag{C-10}$$

As with Eq. C-8, when we substitute the second order accurate difference
analog $\delta_y T_A$ and $\delta_y T_0$ for the first derivatives in Eq. C-10, the resulting
difference analog (given as part of Eq. 29) is between first and second
order accurate in the y-direction. The rest of the expressions given by
Eq. 29 and 30 are similarly obtained.

Figure C-1. Mesh Point Arrangement for Assessing
Accuracy of Mixed Difference Analog
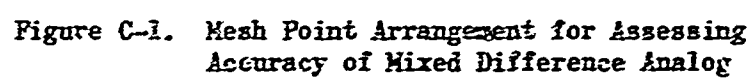
SIMPLIFIED CALCULATION OF NOZZLE HEAT TRANSFER COEFFICIENTS
AND RADIATIVE VIEW FACTORS TO
OUTSIDE ENVIRONMENT

At the throat of a rocket nozzle, the simplified correlation of Bartz
(Ref. 23) can be written as follows:

$$h_g^* = 0.417 \, C_p \left(\frac{1}{D^*}\right)^{0.2} (\mu)^{0.2} \left(\frac{\sigma}{Pr^{0.6}}\right) \left(\frac{P_c}{c^*}\right)^{0.8} \tag{D-1}$$

where h_g^* is the heat transfer coefficient ($Btu/in.^2$-sec-F) at the throat.
The throat diameter, D^*, and the chamber pressure, P_c, are defined by the
engine operating conditions. The specific heat of the combustion gas,
C_p, and the characteristic exhaust velocity of the gas, c^*, are given
by propellant performance data at the operating conditions (Ref. 24).
Propellant performance data also provide the combustion gas temperature,
T_g, the specific heat ratio, γ, and the average molecular weight, $\overline{M}$, from
which the gas viscosity, μ, the Prandtl number, Pr, and the reference
property parameter, σ, are defined.

For most applications, the dimensional groups of Eq. D-1 can be obtained
with sufficient accuracy from simple graphical correlations. Figure D-1
shows $(1/D^*)^{0.2}$ as a function of P_c and the rocket engine thrust, F.
Figure D-2 shows $(P_c/c^*)^{0.8}$ as a function of (P_c/c^*). In Fig. D-3, the
viscosity factor, $\mu^{0.2}$, is plotted vs the product, $\overline{M}T_g$, while Fig. D-4
shows the relation between $(\sigma/Pr^{0.6})$ and γ.

For ablative motor calculations, h_g at the axial location x can be
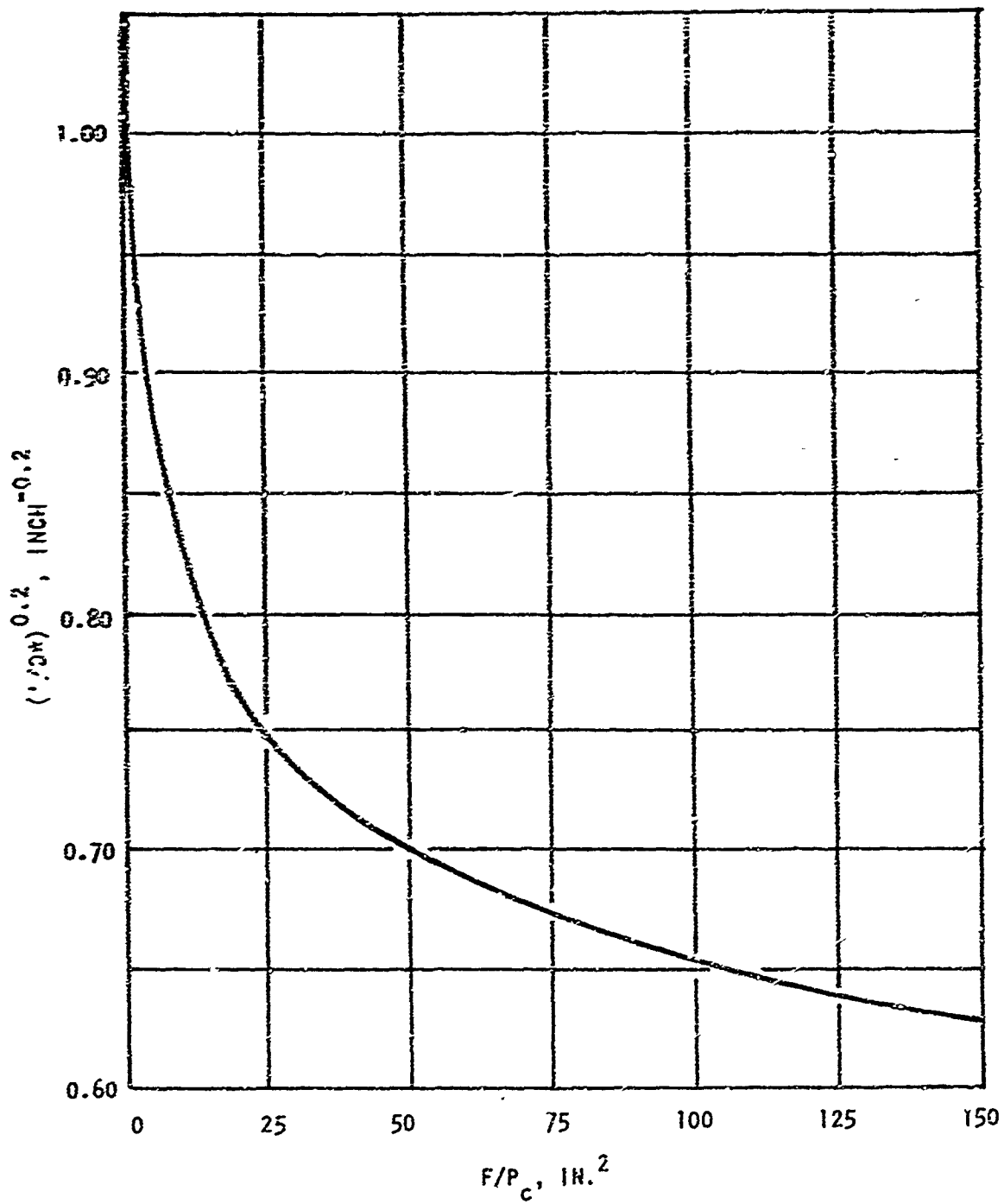related to h_g^* by

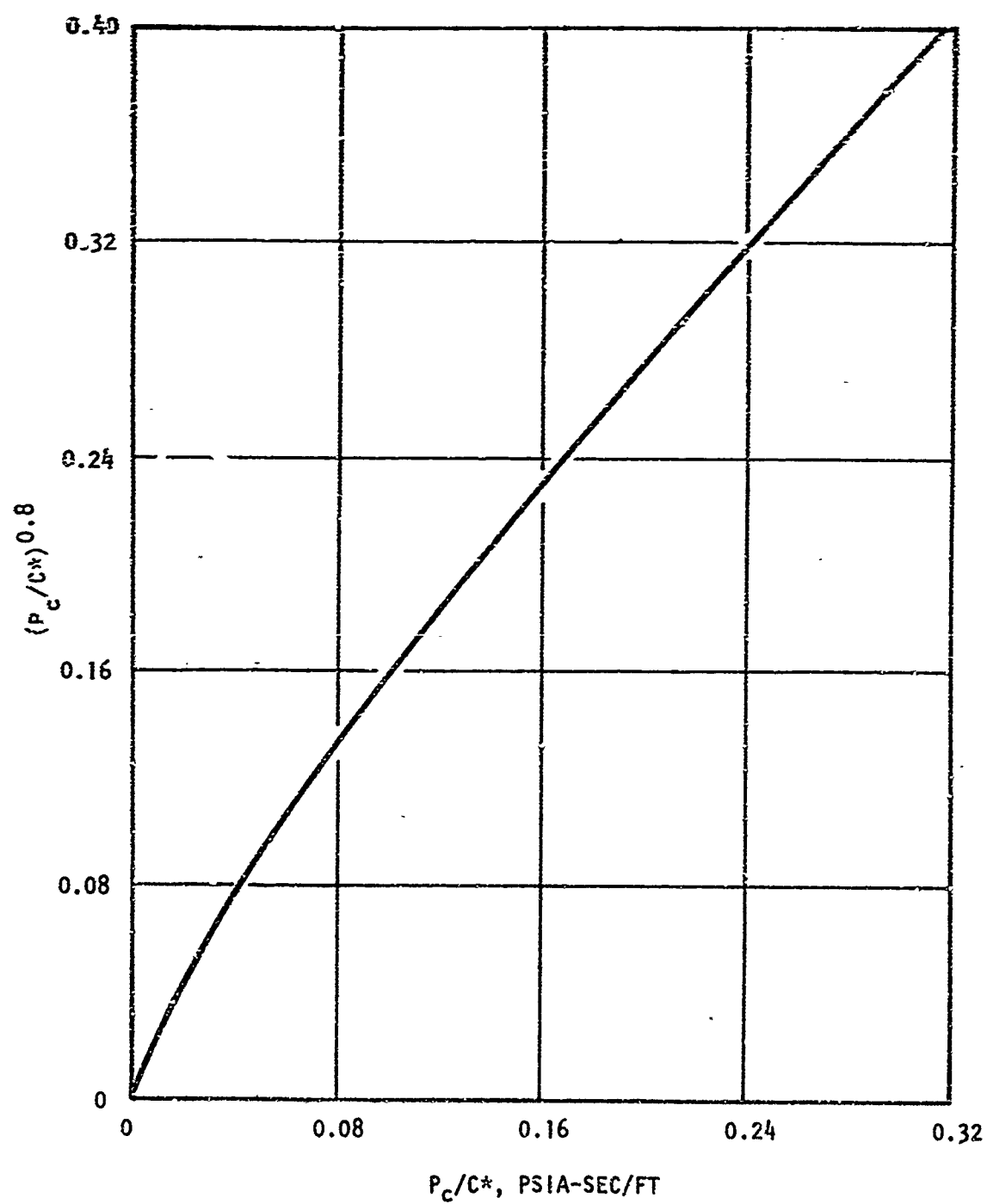Figure D-1. Variation of $(1/D^*)^{0.2}$ With Thrust/P_c Ratio

Figure D-2. Variation of $(P_c/c*)^{0.8}$ With the Ratio of Chamber Pressure to $c*$
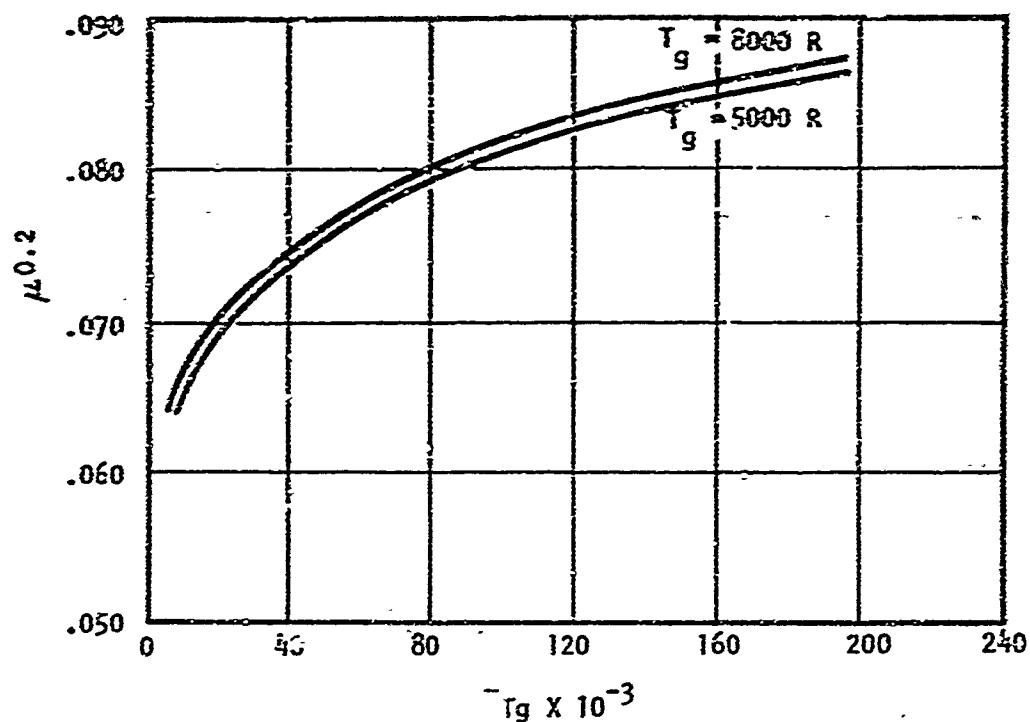
163

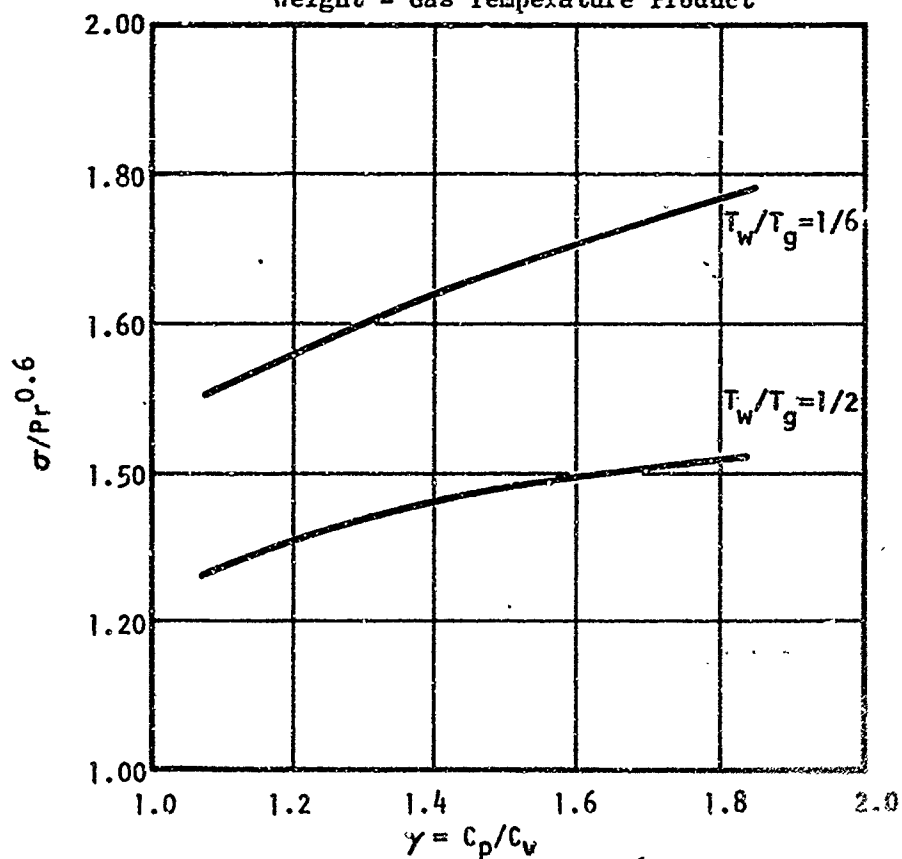Figure D-3. Viscosity Factor as a Function of the Molecular Weight – Gas Temperature Product

Figure D-4. Variation of $\sigma/Pr^{0.6}$ With Specific Heat Ratio

164

$$h_g(x) = h_g^* \left[\frac{D^*}{D(x)}\right]^{1.8} \qquad (D-2)$$

In the throat and expansion regions of the nozzle, the view factor between an element on the inner surface of a 15-degree nozzle and the nozzle exit is given in Fig. D-5.
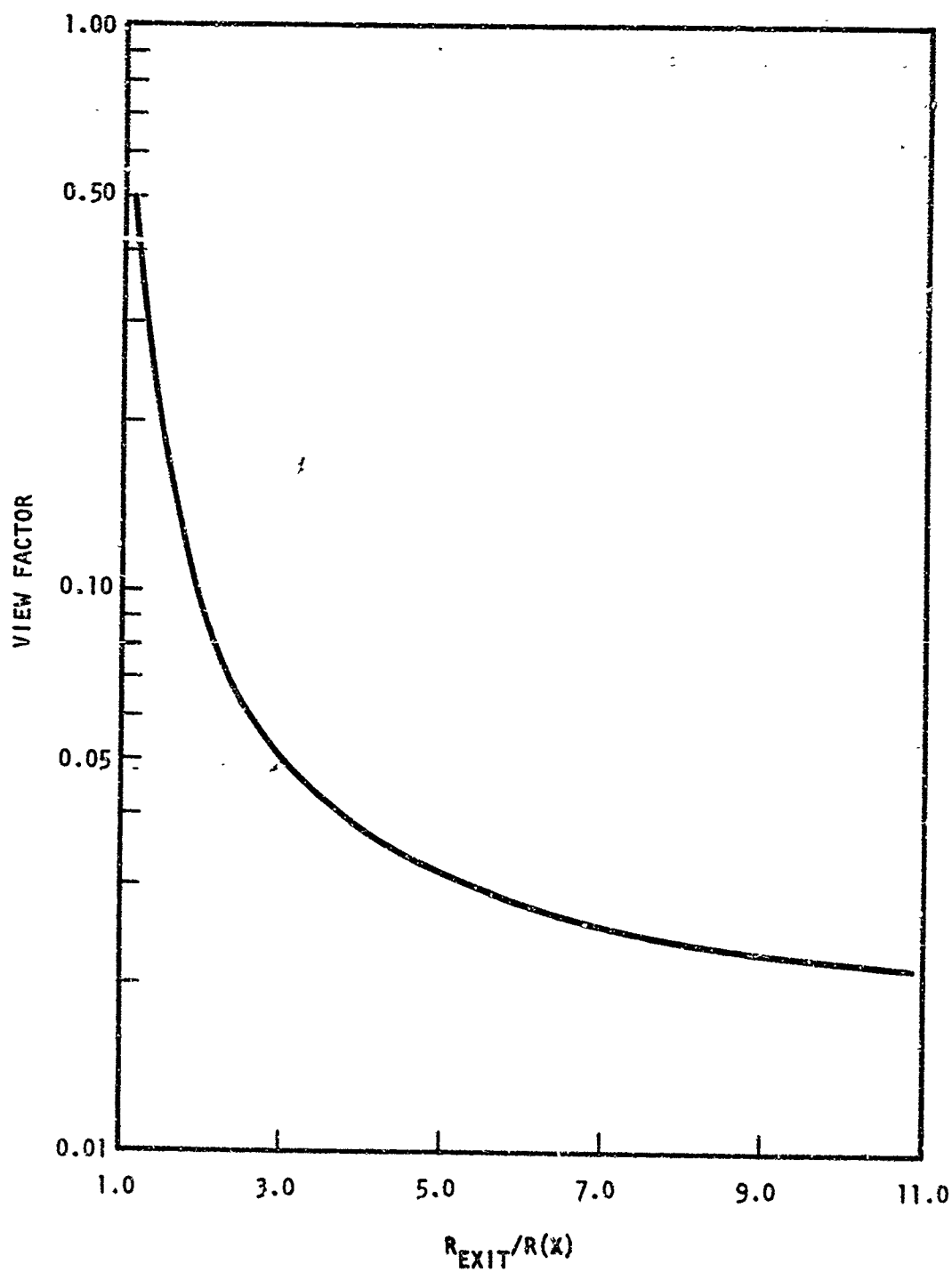
Figure D-5. Variation of View Factor Between Nozzle Surface Element and Nozzle Exit as a Function of the Ratio Between Nozzle Exit Radius and Local Radius

SIMPLIFIED CALCULATION OF CHAR RATE IN THE OVERLAY OF AN ABLATIVE WALL

After the width of the totally charred region becomes thick, relative to the reaction zone in which resin pyrolysis and gas cracking take place, the following simple relation can be written by ignoring the sensible heating of the char layer

$$(q/A)_{char} = U \left(T_{AIH} - T_c \right) \tag{E-1}$$

where U is an overall heat transfer coefficient relating the total heat flux absorbed by the char reaction and the overall temperature difference between combustion gas and an effective char temperature. Equation E-1 can be rewritten in terms of the char rate as

$$\rho_v \bar{Y}_R \, \Delta H \frac{dY_c}{dt} = U \left(T_{AIH} - T_c \right)$$

$$= U \, \Delta T_{eff} \tag{E-2}$$

when $\rho_v \bar{Y}_R \Delta H$ is the heat absorbed per unit volume of virgin resin charred and Y_c is the effective char front. With this model, U is given by

$$\frac{1}{U} = \frac{1}{h_g} + \frac{Y_c}{k_c} \tag{E-3}$$

Equation E-2 can be integrated to give

$$Y_c = k_c \left[\sqrt{\frac{1}{h_g^2} + \frac{2 \, \Delta T_{eff} \, t}{k_c \, \rho_v \bar{Y}_R \Delta}} \; - \frac{1}{h_g} \right] \tag{E-4}$$

167

For long firing times, the term $\dfrac{2 \, \Delta T_{eff} \, t}{k_c \rho_v F_R \, \Delta H}$ is dominating so that the one-dimensional interpolation equations (Eq. 3-2, 3-6, and 3-7) are obtained. The best agreement between the one-dimensional calculations and Eq. E-4 occurs when T_c is defined as 1200 F.

For charring through multiple layers, Eq. E-4 becomes

$$Y_{c_2} = k_{c_2} \left[\sqrt{ \frac{1}{U_2} + \frac{2 \, \Delta T_{eff} \, t_2}{k_{c_2} \rho_v F_R \, \Delta H} } - \frac{1}{U_2} \right] \tag{E-5}$$

where

$$\frac{1}{U_2} = \frac{1}{h_g} + \frac{Y_{c_1}}{k_{c_1}} + \frac{Y_{c_2}}{k_{c_2}} \tag{E-6}$$

In Eq. E-5, the time t_2 begins when the inner layer of thickness Y, has completely charred through.

DOCUMENT CONTROL DATA - R&D

(Security classification of title, body of abstract and indexing annotation must be entered when the overall report is classified)

1. ORIGINATING ACTIVITY (Corporate author)	2a. REPORT SECURITY CLASSIFICATION
Rocketdyne, a Division of North American Aviation, Inc., 6633 Canoga Avenue, Canoga Park, California	UNCLASSIFIED
	2b. GROUP

3. REPORT TITLE

Designer's Guide and Computer Program for Ablative Materials in Liquid Rocket Thrust Chambers

4. DESCRIPTIVE NOTES (Type of report and inclusive dates)

Final Report (1 April 1966 through 30 April 1967)

5. AUTHOR(S) (Last name, first name, initial)

Friedman, H. A., Hines, W. S.; Cunial, G. D.

6. REPORT DATE	7a. TOTAL NO. OF PAGES	7b. NO. OF REFS
April 1967	168 & xvi	25

8a. CONTRACT OR GRANT NO.	9a. ORIGINATOR'S REPORT NUMBER(S)
AF04(611)-11415	
b. PROJECT NO.	R-7022
c.	9b. OTHER REPORT NO(S) (Any other numbers that may be assigned this report)
d.	

10. AVAILABILITY/LIMITATION NOTICES This document is subject to special export controls and each transmittal to foreign governments or foreign nationals may be made only with prior approval of AFRPL (RPPR/STINFO), Edwards, California 93523.

11. SUPPLEMENTARY NOTES	12. SPONSORING MILITARY ACTIVITY
	AFRPL, Edwards Air Force Base, California

13. ABSTRACT

The two-dimensional ablative heat transfer computer program generated under contract AF04(611)-9714 was refined and extended to handle anisotropic materials, more than one charring material and reradiation at the heated surface. Results of the two-dimensional program were compared to experimental data to determine effective values of material properties used in the analysis to simulate gas generation and cracking reactions. The resulting effective properties for two ablative materials were used in a parametric study generating basic information for the design of ablative systems in liquid rocket thrust chambers. Graphs and charts showing the variation of thermal penetration, char depth and surface erosion are included.

DD FORM 1473
(1 JAN 64)

14.	LINK A		LINK B		LINK C	
KEY WORDS	ROLE	WT	ROLE	WT	ROLE	WT
Two-Dimensional Ablative Program Multiple Charring Ablators Nozzle Throat Erosion Anisotropic Materials Parametric Study Designer's Guide Effective Material Properties Re-Radiation						

INSTRUCTIONS

1. ORIGINATING ACTIVITY: Enter the name and address of the contractor, subcontractor, grantee, Department of Defense activity or other organization (corporate author) issuing the report.

2a. REPORT SECURITY CLASSIFICATION: Enter the overall security classification of the report. Indicate whether "Restricted Data" is included. Marking is to be in accordance with appropriate security regulations.

2b. GROUP: Automatic downgrading is specified in DoD Directive 5200.10 and Armed Forces Industrial Manual. Enter the group number. Also, when applicable, show that optional markings have been used for Group 3 and Group 4 as authorized.

3. REPORT TITLE: Enter the complete report title in all capital letters. Titles in all cases should be unclassified. If a meaningful title cannot be selected without classification, show title classification in all capitals in parenthesis immediately following the title.

4. DESCRIPTIVE NOTES: If appropriate, enter the type of report, e.g., interim, progress, summary, annual, or final. Give the inclusive dates when a specific reporting period is covered.

5. AUTHOR(S): Enter the name(s) of author(s) as shown on or in the report. Enter last name, first name, middle initial. If military, show rank and branch of service. The name of the principal author is an absolute minimum requirement.

6. REPORT DATE: Enter the date of the report as day, month, year; or month, year. If more than one date appears on the report, use date of publication.

7a. TOTAL NUMBER OF PAGES: The total page count should follow normal pagination procedures, i.e., enter the number of pages containing information.

7b. NUMBER OF REFERENCES: Enter the total number of references cited in the report.

8a. CONTRACT OR GRANT NUMBER: If appropriate, enter the applicable number of the contract or grant under which the report was written.

8b, 8c, & 8d. PROJECT NUMBER: Enter the appropriate military department identification, such as project number, subproject number, system numbers, task number, etc.

9a. ORIGINATOR'S REPORT NUMBER(S): Enter the official report number by which the document will be identified and controlled by the originating activity. This number must be unique to this report.

9b. OTHER REPORT NUMBER(S): If the report has been assigned any other report numbers (either by the originator or by the sponsor), also enter this number(s).

10. AVAILABILITY/LIMITATION NOTICES: Enter any limitations on further dissemination of the report, other than those

imposed by security classification, using standard statements such as:

(1) "Qualified requesters may obtain copies of this report from DDC."

(2) "Foreign announcement and dissemination of this report by DDC is not authorized."

(3) "U. S. Government agencies may obtain copies of this report directly from DDC. Other qualified DDC users shall request through

_____ ."

(4) "U. S. military agencies may obtain copies of this report directly from DDC. Other qualified users shall request through

_____ ."

(5) "All distribution of this report is controlled. Qualified DDC users shall request through

_____ ."

If the report has been furnished to the Office of Technical Services, Department of Commerce, for sale to the public, indicate this fact and enter the price, if known.

11. SUPPLEMENTARY NOTES: Use for additional explanatory notes.

12. SPONSORING MILITARY ACTIVITY: Enter the name of the departmental project office or laboratory sponsoring (paying for) the research and development. Include address.

13. ABSTRACT: Enter an abstract giving a brief and factual summary of the document indicative of the report, even though it may also appear elsewhere in the body of the technical report. If additional space is required, a continuation sheet shall be attached.

It is highly desirable that the abstract of classified reports be unclassified. Each paragraph of the abstract shall end with an indication of the military security classification of the information in the paragraph, represented as (TS), (S), (C), or (U).

There is no limitation on the length of the abstract. However, the suggested length is from 150 to 225 words.

14. KEY WORDS: Key words are technically meaningful terms or short phrases that characterize a report and may be used as index entries for cataloging the report. Key words must be selected so that no security classification is required. Identifiers, such as equipment model designation, trade name, military project code name, geographic location, may be used as key words but will be followed by an indication of technical context. The assignment of links, rules, and weights is optional.